Università degli Studi di Siena
Facoltà di Scienze M.F.N.

Dipartimento di Fisica

Dottorato di Ricerca in Fisica Sperimentale, XVI ciclo
(Ph.D. Thesis in Experimental Physics)

AMS-02 dark matter search inspecting cosmic ray positron spectrum

Dott.ssa **Elisa Falchini**

Relatore
Chiar.mo Prof. **Franco Cervelli**

Siena, Luglio 2004

Contents

Introduction

In this thesis is summarized my research activity, during a period of three years as PhD student, in the *Alpha Magnetic Spectrometer* (AMS-02) experiment. AMS is a particle detector aimed to high precision measurements of cosmic ray fluxes in Space. It is under construction by a world wide international collaboration and will be part of the scientific program on board the International Space Station, where it will collect data for three years. The AMS experiment has been designed to investigate fundamental open questions in current astroparticle physics including the existence of cosmological antimatter and the physical nature of the dark matter content of our galaxy.

Cosmological parameters such as the total density of the Universe and the rate of cosmological expansion are being precisely measured for the first time in this period, and a consistent standard picture of the Universe is beginning to emerge. Nevertheless there are some "old" problems still open: though the case for *Dark Matter* holding together galaxies has been around since a long time, the nature of the dark matter in the Universe is still unknown. Most likely astroparticle physics research will soon yield the answer that we are waiting for.

The working hypothesis is that it is formed by weakly interacting elementary particles produced in the early Universe. The most promising candidate for the cold dark matter particles is the *neutralino.* Neutralinos can be detected by indirect methods by looking at annihilation products ($\overline{p}$, e^+, γ, ν) in cosmic rays. One of the main purposes of AMS-02 is then to study the positron spectrum with high resolution and at energies never reached before (hundreds of GeV). A deviation of positrons spectrum from a standard power-law energy distribution would provide a signature for the existence of dark matter neutralino.

The core of the AMS-02 detector is a superconducting magnet, generating a very strong field, enclosing the silicon tracking system; the other subdetectors are the time of flight (TOF) system, the transition radiation detector (TRD), the ring imaging Čherenkov (RICH) and the electromagnetic calorimeter (ECAL).

The AMS research group of INFN (Pisa - Siena) projected the calorimeter and participates to the construction and operation. The electromagnetic calorimeter is a fine grained sampling device with a lead - scintillating fibers structure. The accurate measurement of the e^+ spectrum at energies greater than 10 GeV requires a high rejection power of a cosmic ray background, mainly consisting of protons, and a very good energy resolution. These requirements are achieved by ECAL with a good imaging capability in 3D (that allows a discrimination between hadronic and electromagnetic cascades) and a thickness corresponding to about 17 radiation lengths (that allows a good containment of the electromagnetic showers).

My contribution to the activity of the AMS group includes the development of the code for the calorimeter simulation that is now inserted in the official AMS Monte Carlo software. At the same time, I participated to the ECAL tests beam at CERN and made the data analysis to estimate the calorimeter performances. I studied and implemented new algorithms for the analysis and wrote the code dedicated to the reconstruction of events in the calorimeter. Then I outlined an analysis strategy for electromagnetic/hadronic discrimination that was applied to the AMS Monte Carlo simulated data, in order to investigate the AMS-02 capability to measure the cosmic positrons spectrum.

The outline of the thesis, organized in five chapters, is as follows:

Chapter 1 An introduction to the Big Bang cosmology is performed, together with the description of the most recent and important experimental measurements of the cosmological parameters. A review of the dark matter scenario, and the neutralino detection strategy are presented.

Chapter 2 The AMS-01 detector and major results are described. For AMS-02 are illustrates the working principles, each subdetectors, the trigger and the prospect.

Chapter 3 The principal features of the electromagnetic calorimeter (ECAL) structure are shown. Then the characteristic of the electromagnetic shower are described together with the leading differences between electromagnetic and hadronic behavior in ECAL.

Chapter 4 The analysis of the ECAL Test Beam data is reported. Two calibration procedures are described and their results are compared. The performances of the calorimeter in linearity and energy resolution are shown.

Chapter 5 The discrimination capability between electromagnetic and hadronic cascades of AMS-02 are studied; the analysis strategy is described in details. Eventually the rejection power on the protons spectrum and the efficiency on the positrons spectrum are given.

Chapter 1

The Dark Side of the Universe

Cosmology is undergoing an explosive period of activity, fueled by new accurate astrophysical data. Cosmological parameters such as the total density of the Universe and the rate of cosmological expansion are being precisely measured for the first time, and a consistent standard picture of the Universe is beginning to emerge. Nevertheless there are some "old" problems still open: though the case for *Dark Matter* holding together galaxies has been around for a long time (1970 [1]), the nature of the dark matter in the Universe is still unknown. Most likely astroparticle physics research will soon yield the answer that we are waiting for.

1.1 The Big Bang Cosmology

The *Big Bang* theory, based on the General Relativity theory [2, 3], describes the evolution of the early Universe since a fraction of a second up to now. The theory predicts three fundamental facts, which are in agreement with experiments:

· the increase of mutual distances among galaxies (Universe expansion) [4];

· the abundance of light elements [5];

· the existence of a background radiation [6].

The main idea behind General Relativity is that space-time geometry is determined by the distribution of masses within it.

Considering the small scale structure of the Universe, matter distribution is rather irregular: stars are grouped in galaxies which form *clusters* that arrange themselves in *super-clusters*. Only on larger scales ($\gtrsim 10^8$ light-year) it is sensible to assume an almost homogeneous distribution. If, together with homogeneity, we also assume the isotropy of the Universe, the so called *cosmological principle* holds: a family of spatial sections of space-time exists such that every section has the same physical properties in every point and direction [7].

The most general space-time metric of a homogeneous and isotropic Universe is given by the *Robertson-Walker* metric:

$$d\tau^2 = dt^2 - a^2(t)\left[\frac{dr^2}{1-kr^2} + r^2(d\theta^2 + sin^2\theta d\phi^2)\right]$$

Matter is supposed to be macroscopically at rest with respect to the coordinate system t, r, θ, ϕ (comoving coordinates). The Universe expansion is governed by the *scale factor* $a(t)$ which depends only on the time t; k determines the *spatial* curvature:

$$\begin{aligned} k = -1 &\rightarrow \textit{open Universe} \\ k = 0 &\rightarrow \textit{flat Universe} \\ k = 1 &\rightarrow \textit{closed Universe} \end{aligned}$$

Notice that in this space-time model the curvature is constant (i.e. it is the same everywhere in the Universe): this is a direct consequence of the cosmological principle. Usually, if $k < 0$ we think the Universe as open, since it expands forever. On the contrary, if $k > 0$, the Universe is said closed, because, it is doomed to collapse at some future time. The boundary case, $k = 0$, is called a flat Universe.

We will see that these statements are correct only if there is no cosmological constant (the vacuum energy in the quantum field theory). From general considerations of homogeneity and isotropy, however, the cosmological constant can be present, and these notions need to be modified.

In 1929, Edwin Hubble observed a red-shift in the spectra of distant galaxies, which indicated that they were receding from us at a velocity proportional to their distance (from us). This was correctly interpreted as due to the expansion of the Universe, that is, to the fact that the scale factor today is larger than when the photons were emitted by the observed galaxies. The space-time fabric is stretching between galaxies, hence the observed wavelength (λ_{obs}) of photons coming from distant objects is enlarged with respect to the corresponding one (λ_{em}) at the emission time by a factor precisely equal to the ratio of scale factors:

$$\frac{\lambda_{obs}}{\lambda_{em}} = \frac{a_0}{a} \equiv 1 + z$$

where a_0 is the present value of the scale factor and z is the *cosmological red-shift*.

The expansion rate of the Universe is given by the *Hubble constant*:

$$H(t) \equiv \frac{\dot{a}(t)}{a(t)}$$

whose value today is denoted by H_0. It is possible to compute the relation between the physical distance d_L and the present rate of expansion, in terms of the red-shift parameter:

$$H_0 d_L = z + \frac{1}{2}(1 - q_0)z^2 + \mathcal{O}(z^3). \tag{1.1}$$

where q_0 is a constant called deceleration parameter (defined below). At small distances from us, i.e. at $z \ll 1$, we can safely keep only the linear term, and thus the recession velocity becomes proportional to the distance from us, $v = c\,z = H_0\,d_L$, the proportionality constant being the Hubble rate, H_0. This expression represents the so-called *Hubble law*, and is spectacularly confirmed by a huge amount of data, up to distances of hundreds of mega-parsecs. Only recently measurements from very bright and distant supernovae, at $z \simeq 1$, were obtained, allowing to start probing the second-order term, proportional to the deceleration parameter q_0.

The value of the Hubble constant is obtained from the *Hubble law*. Large systematic uncertainties in determining distances have made an accurate determination of the Hubble constant a challenge, and only recently improvements in instrumentation, the launch of the Hubble Space Telescope, and the development of several different measurement methods have led its value to converge [8]:

$$H_0 = 72 \pm 2 \pm 7 \; km/sMpc$$

(where the error bars represent statistical and systematic uncertainties, respectively) which is usually rewritten in the form:

$$H = 100h \quad km/sMpc$$

and h is the adimensional parameter which also reflects the accuracy of the measurements.

According to general relativity, from Einstein equations and assuming the cosmological principle, we obtain:

$$H^2 = \left(\frac{\dot{a}(t)}{a(t)}\right)^2 = \frac{8\pi G}{3}\rho - \frac{k}{a^2(t)} + \frac{\Lambda}{3} \tag{1.2}$$

$$\frac{\ddot{a}(t)}{a(t)} = -\frac{4\pi G}{3}(\rho + 3p) + \frac{\Lambda}{3}. \tag{1.3}$$

where ρ is the mass density, and p is the pressure. Λ is the *Cosmological Constant* and gives a contribution distinct from that of matter; in fact it can be associated with the vacuum energy in quantum field theory, although we still do not understand why it should have such a small value (120 orders of below the quantum theory prediction). This constitutes today one of the most fundamental problems of physics.

A *critical* density ρ_c is usually defined which, in absence of a cosmological constant, would correspond to a flat Universe ($k = 0$):

$$\rho_c \equiv \frac{3}{8\pi G}H^2$$

$$\rho_{c0} = \frac{3}{8\pi G}H_0^2 = 1,88h^2 \times 10^{-29} g/cm^3$$
$$\sim 4 \quad protons/m^3$$

We can define another adimensional parameter Ω equal to the ratio between the actual and the critical density:

$$\Omega \equiv \frac{\rho}{\rho_c}.$$

In the Universe many different types of matter are present; so we can define the ratios $\Omega_i \equiv \rho_i/\rho_c$ for matter, radiation, cosmological constant and even curvature:

$$\Omega_M \equiv \frac{8\pi G \rho_M}{3H_0^2} \qquad \Omega_R \equiv \frac{8\pi G \rho_R}{3H_0^2}$$

$$\Omega_\Lambda \equiv \frac{\Lambda}{3H_0^2} \qquad \Omega_k \equiv -\frac{k}{a_0^2 H_0^2}.$$

As it will be shown in the following, the radiation component Ω_R, corresponding to relativistic particles, is negligible in the present Universe.

An interesting consequence of these definitions is that we can now write the Friedman equation 1.2 today, $a = a_0$, as a *cosmic sum rule*, emphasizing that the matter and vacuum energy density in the Universe determines its geometry:

$$1 = \Omega_M + \Omega_\Lambda + \Omega_k$$

(where we have neglected Ω_R today).

Another very useful relationship is that of the *cosmological deceleration parameter* today, q_0, in terms of the matter and cosmological components of the Universe (see Eq. 1.3):

$$q_0 \equiv -\frac{\ddot{a}}{aH^2}\bigg|_0 = \frac{1}{2}\Omega_M - \Omega_\Lambda. \tag{1.4}$$

Uniform expansion corresponds to $q_0 = 0$ and requires a precise cancellation: $\Omega_M = 2\Omega_\Lambda$. It represents spatial sections that are expanding at a fixed rate, its scale factor growing by the same amount in equally-spaced time intervals. Accelerated expansion corresponds to $q_0 < 0$ and occurs whenever $\Omega_M < 2\Omega_\Lambda$: spatial sections expand at an increasing rate, their scale factor growing at a greater speed within each subsequent time interval. In the opposite case, $\Omega_M > 2\Omega_\Lambda$, we have decelerated expansion corresponding to $q_0 > 0$. So new classes of Universe evolution models are admitted: for instance, spatially open Universes may re-collapse, closed Universes can expand forever and there can be also models without an initial singularity [9].

In Fig 1.1 a range of possible evolutions of the scale factor $a(t)$ are shown for various pairs of values of $(\Omega_M, \Omega_\Lambda)$. All these panels have been summarized in Fig. 1.2, where we have shown which values of Ω_M and Ω_Λ give open or closed Universes, as well as hyperbolic or elliptical Universes. As we clearly see in this plot, the identification of closed Universes with elliptical ones works only for $\Lambda = 0$, and so does the identification of open Universes with hyperbolic ones.

How to determine which one is our own Universe?

What is easy to say, is that we do not live in a bouncing Universe, i.e. one without initial singularity. The reason is that such Universes have a minimum value of a/a_0, and correspondingly a certain maximum value for the red-shift parameter z which it is not observed. However, this still leaves us with a vast region in the Ω_M-Ω_Λ parameter region, and we need to set up a strategy to proceed. The general (and obvious) strategy is the following. We need to find some observable quantity which depends on the cosmological parameters and determine its value. Inverting these dependencies will give us the values of the cosmological parameters. Our original question now shifts to the following one: which are good observables for this purpose?

Important results are obtained by investigating:

- Cosmic Microwave Background (CMB) anisotropies;

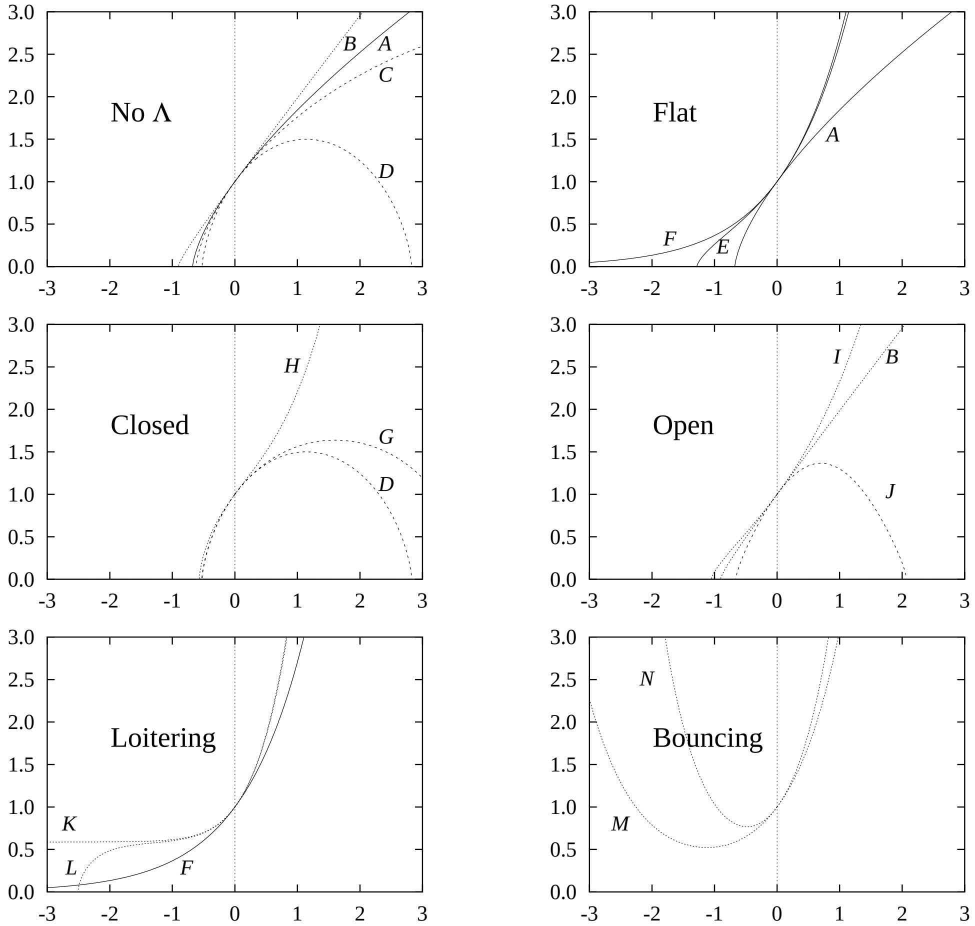

Figure 1.1: Time evolution of the scale parameter for different values of matter density and cosmological parameter. The horizontal axis represents $H_0(t - t_0)$; the vertical axis is $y = a/a_0$ in each case. The values of $(\Omega_M, \Omega_\Lambda)$ for different plots are: A=(1,0), B=(0.1,0), C=(1.5,0), D=(3,0), E=(0.1,0.9), F=(0,1), G=(3,0.1), H=(3,1), I=(0.1,0.5), J=(0.5,-1), K=(1.1,2.707), L=(1,2.59), M=(0.1,2.5), N=(0.1,2.5).

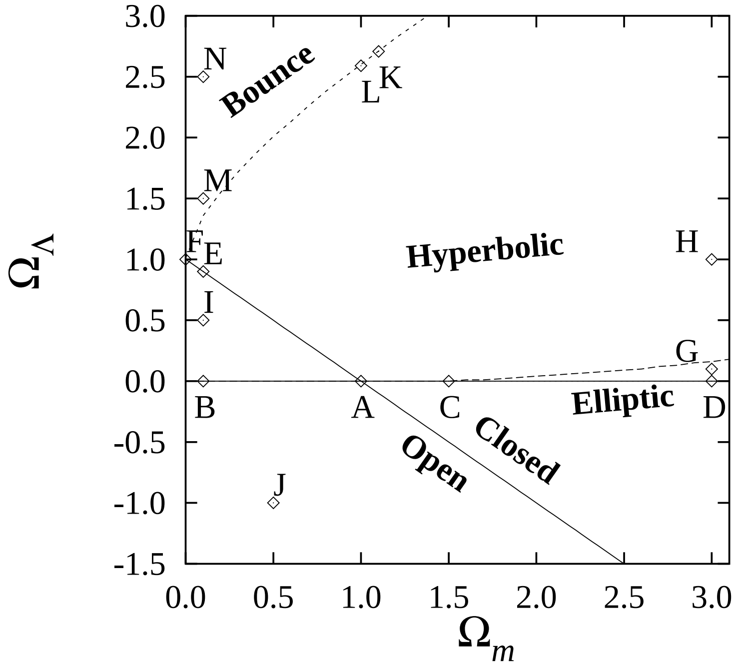

Figure 1.2: Summary of the different evolution plots presented in Fig. 1.1. The borderline between open and closed Universes represents flat Universes, between hyperbolic and bounce Universes represents loitering Universes, and the one between elliptic and hyperbolic Universes are called critical Universes.

- Supernovae of type 1a.

1.2 Experimental measurements of cosmological parameters

Space research has provided most of the data of interest in this field: the Hubble Space Telescope has provided precise measurements of the expansion rates of the Universe; the COBE [10] satellite has measured the spectrum and temperature of the CMB with high precision and its anisotropy at large scales; the BOOMERanG balloon-borne experiment has measured the anisotropy at sub-horizon scales [11]; the WMAP satellite has measured the anisotropy of the CMB on the whole sky.

Ground experiments have also contributed important achievement being able to measure data from Supernovae of type 1a.

1.2.1 The Total Density of the Universe

The Cosmic Microwave Background is one of the observable relics of the *Hot* Big Bang, together with the abundance of primordial elements and the distribution of galaxies and other predicted but yet seen such as gravitational waves and neutralinos backgrounds. All these relics are inter-related, and current cosmological research is trying to explain a variety of observations simultaneously.

Photons generated in the early Universe underwent the last scatterings at the recombination time (when the Hydrogen atoms formed from the primeval plasma and the Universe became transparent). They form a faint but very important thermal microwave background. Its spectrum today is very precisely that of a blackbody with $T = (2.725 \pm 0.002)\ K$ [10].

Recombination is also important for the development of structures in the Universe. Density perturbations were oscillating in the plasma era, afterward recombination density perturbations can grow and create the hierarchy of structures we see in the nearby Universe. CMB temperature fluctuations are closely related to density fluctuations at recombination, therefore mapping the CMB temperature we map the density and velocity fields in the Universe at recombination and sample the direct result of early physical processes. In the primeval plasma, photon/baryon density perturbations start to oscillate only when the sound horizon becomes larger then their linear size. Small wavelength perturbations oscillate faster than large ones. The result is that perturbations with different linear size arrive at recombination with different phases. The largest ones have about the same size as the horizon at recombination: these have just enough time to arrive at recombination maximally compressed (or rarefied). They produce a network of cold and hot spots in the image, with the dimensions of the acoustic horizon (similar to the casual one, since the sound speed in the plasma is $\sim c/\sqrt{3}$). The presence of a characteristic dimension of the spots results in a peak in the angular power spectrum of the CMB image. The projected angular size of the horizon can be computed by means of the Friedmann equation as a function of the cosmological parameter [12]. We expect a strong dependence of this observable from the density parameter, which controls the curvature of the Universe. The computation shows that the result is mainly a function of two cosmological parameter: the density parameter for matter Ω_M, and the density parameter for vacuum (dark) energy Ω_Λ. If $\Omega_\Lambda + \Omega_M = \Omega = 1$, then the dependence on the relative contributions of matter and vacuum is very weak, and the typical size of the horizon is $\Theta_h \sim 0.85^0$. These spots produce a peak in the power spectrum at multipole $l_1 = \pi/\Theta_h \sim 210$.

From the BOOMERanG experiment a firm detection of a first peak in the CMB angular power spectrum on about degree scales has been obtained in the year 2000. The recent results from the WMAP (Wilkinson Microwave Anisotropy Probe) satellite experiment have confirmed in a spectacular way all the previous results with a considerable reduction of the error bars (Figure 1.3).

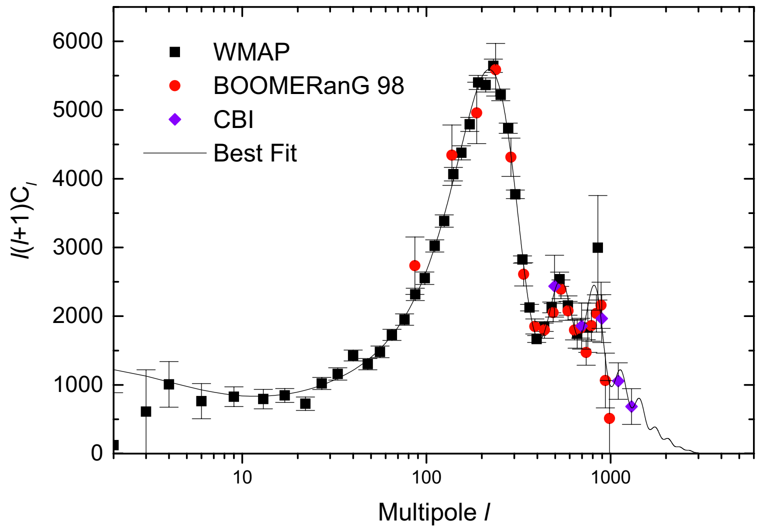

Figure 1.3: Cosmic Microwave anisotropies data from WMAP, BOOMERanG and CBI experiments.

The WMAP mission was designed to measure the CMB anisotropy with unprecedented precision (a sensitivity of 20 μK per 0.3^0 square pixel, with systematic artifacts limited to 5 μK per pixel) and accuracy on angular scales over the whole sky of several arc minutes producing maps at five frequencies from 23 to 94 GHz. To achieve these goals, WMAP uses differential microwave radiometers that measure temperature differences between two points on the sky. WMAP observes the sky from an orbit at the L2 Sun-Earth Lagrange point, 1.5 million km from Earth; this vantage point offers an exceptionally stable environment for observation since the observatory can always point away from the Sun, Earth and Moon while maintaining an unobstructed view to deep space. The satellite observes the sky with a compound spin and precession that covers the full sky every six months. The resulting map after the first year of flight is shown in Figure 1.4.

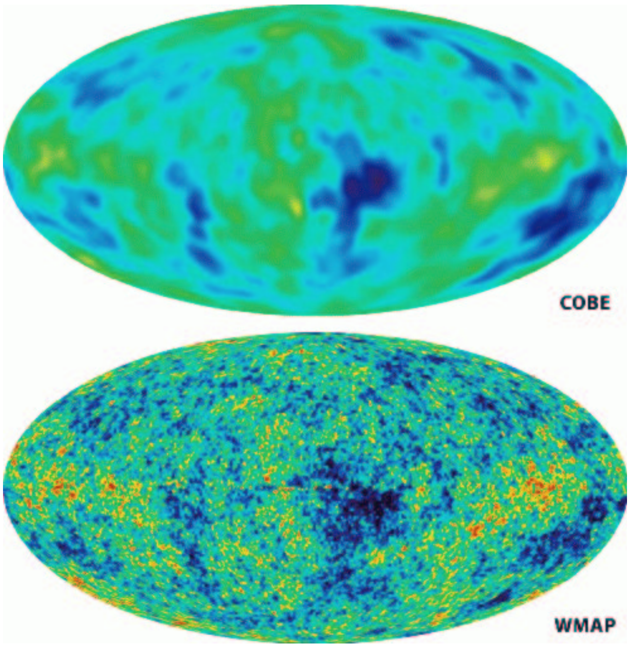

Figure 1.4: Anisotropy of the Cosmic Microwave Background: All sky maps, made by COBE (*upper*) and by WMAP (*lower*); the range of color scale is $\pm 200\ \mu K$.

The best fit parameters from the WMAP [13] data only are:

$$h = 0.72 \pm 0.05 \qquad \Omega_B h^2 = 0.024 \pm 0.001 \qquad \Omega_M h^2 = 0.14 \pm 0.02$$

These parameters fit both finer scale CMB measurements and measurements of the large scale structure. Therefore the emerging standard model of cosmology fitting the WMAP data is that of a flat Λ-dominated Universe seeded by a nearly scale-invariant adiabatic Gaussian fluctuations. This simple model is also consistent with a host of other astronomical measurements: the predicted age of the Universe is consistent with stellar ages, the baryon/photon ratio is consistent with measurements of the Deuterium/Hydrogen ratio, and the inferred Hubble constant is consistent with local observations of the expansion rate.

By combining WMAP data with other astronomical data the geometry of the Universe is constrained (Figure 1.5):

$$\Omega_{tot} = 1.02 \pm 0.02$$

A comprehensive summary of all the recent results from the WMAP experiment has been published on the Astrophysics Journal Supplement 148 (2003).

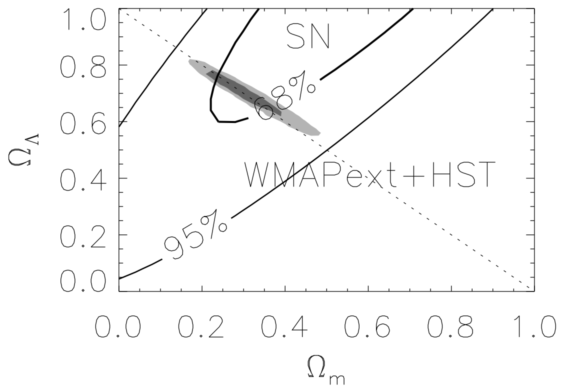

Figure 1.5: Constraint on the geometry of the Universe: $\Omega_M - \Omega_\Lambda$ plane. This figure shows the two dimensional likelihood surface for various combinations of data.

1.2.2 The Rate of Cosmological Expansion

Another quantity that depends on Ω_M and Ω_Λ is the *look back time* for any object. We look at a certain object in the sky and accurately determine its red-shift. All we have to do now, is to find a way of knowing at which time the light that we observe was emitted from the object. But this cannot be done very well. By looking at the composition of the object and by comparing it with some evolutionary model, we can arguably estimate the age. This will however depend on the evolutionary model; hence the method is somewhat uncertain. Therefore one usually relies on the measurement of distances of objects as a function of their red-shifts for the purpose of determining cosmological constants. The distance as a function of the red-shift depends only on H_0 for low z ($z \lesssim 0.1$), while in the high z region it depends also on Ω_M and Ω_Λ thus allowing the determination of these parameters (see Eq. 1.1 and Eq 1.4).

Supernovae of type 1a are identified by the nature of their light curve, i.e., the variation of their intensity with time; in addition, the spectral analysis reveals lines for heavy elements like magnesium and silicon. Supernovae of this type are believed to occur due of the merging of two white dwarfs with masses very close to the Chandrasekhar limit. Since the masses involved in the explosion are roughly the same for any supernovae 1a, it is reasonable to assume that the intrinsic (or absolute) luminosity of any supernovae of this type is the same. Thus, if one measures the apparent luminosity at the maximum of the light curve, this should scale as the inverse square of the distance of the supernova.

The red-shifts and apparent magnitudes of nearby supernovae should determine the Hubble parameter. Using this value, one can go over to larger values of z and determine Ω_M and Ω_Λ.

The High-z Supernova Search Team [14] has discovered and observed some new supernovae in the redshift interval $z = 0.3 \div 1.2$. These independent observations, analyzed by similar but distinct methods, confirm the old results that supernovae luminosity distances imply an accelerating Universe. These measurements provide another quantitative confirmation of the importance of dark energy. In particular the range of possible values for Ω_Λ and Ω_M has been determined. The results are shown in Figure 1.6.

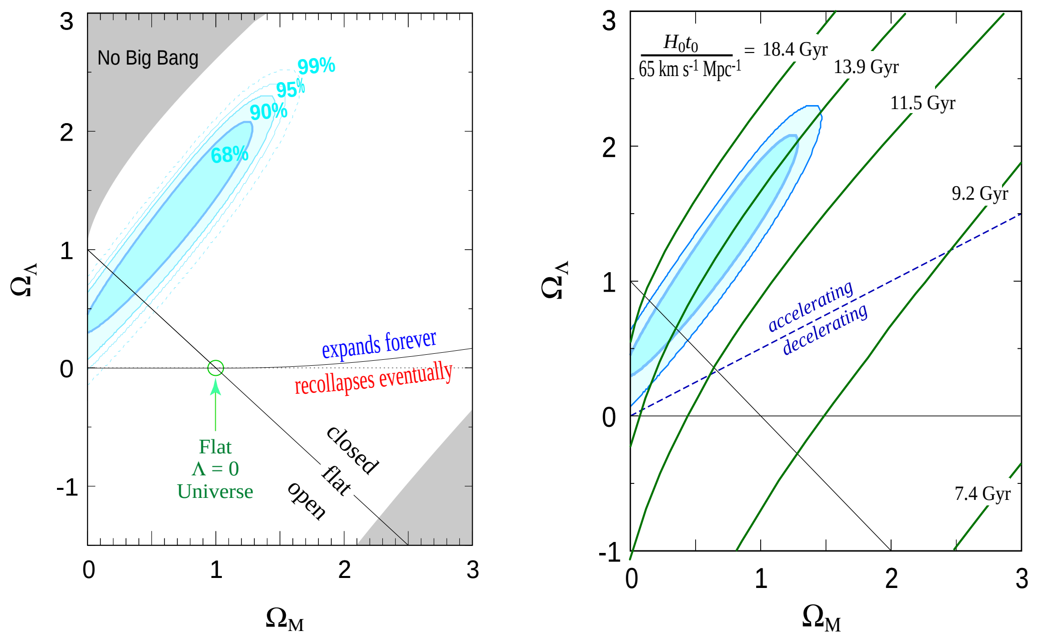

Figure 1.6: The evidenced oval zone is the most probable region according to supernovae observations. This region is intersected by the line $\Omega = \Omega_\Lambda + \Omega_M = 1$, and is compatible with the result from dark matter measurement: $\Omega_M \simeq \Omega_{DM} \sim 0.3$.

In conclusion there are two different experimental results (the Universe acceleration and its curvature) that are compatible with each other and identify two regions in the plane of possible values of Ω_M and Ω_Λ which have a common intersection. In this common zone Ω_M assumes the value ~ 0.3 thus supporting the result obtained from the measurements of the hydrogen velocities in galaxies.

1.3 The Dark Matter

Observation of gas clouds in galaxies show [1] that the rotation velocity tends to

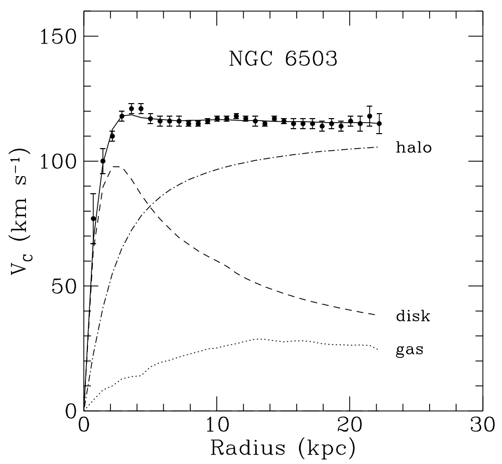

Figure 1.7: Rotation curve of the spiral galaxy NGC 6503, determined by radio measurements of the 21 *cm* line emission of neutral Hydrogen in the disk. The dashed line shows the rotation curve expected from the disk material alone, the dot-dashed line is from the dark matter halo alone [15].

a constant as the distance r from the galaxy center increases. If the total mass of the galaxy were only due to visible matter (i.e. stars, etc.), then the rotation velocity, outside the luminous disk, should decrease proportionally to $1/\sqrt{r}$. On the other hand, the observed behavior implies that the density distribution $\rho(r)$ is proportional to $1/r^2$; it follows that:

$$M(r) \propto r$$

where $M(r)$ is the total mass within a sphere of radius r centered at the galaxy center. Notice that the above mass distribution is proper of a self gravitating isothermic gas; hence a natural explanation of the behavior shown in Fig. 1.7 is that a big fraction of the galaxy mass is due to an invisible halo (*dark matter*).

An estimate of the relative visible matter density is obtained from the luminosity for different sources:

$$\Omega_{lum} = 3.5 \times 10^{-3} h^{-2}$$

It follows that

$$\rho_{lum} = (0.7\% \div 0.35\%)\rho_c$$

Experimental data for the velocities of gas clouds of different type of galaxies [16] give the following values for the ratios between the masses of the dark (M_{dm}) and visible (M_{lm}) matter:

· $3 < \frac{M_{dm}}{M_{lm}} < 5$ for spiral galaxies;

· $10 < \frac{M_{dm}}{M_{lm}}$ for elliptic galaxies;

· $\frac{M_{dm}}{M_{lm}} \sim 50 \div 100$ for clusters of galaxies.

Once known the dark matter density, we obtain $\Omega_{DM} \sim 0.1$ for the dark matter inside galaxies and $\Omega_{DM} \sim 0.3$ for that between galaxies.

In principle, the background radiation and neutrinos also contribute to the total density of the Universe. If ρ_R is the radiation energy density, we have:

$$\rho_R = \frac{\pi^2}{15}\frac{(kT_R)^4}{(\hbar c)^3} = 4.5 \times 10^{-34} \qquad g/cm^3$$

this, together with:

$$\Omega_R \equiv \frac{8\pi G\rho_R}{3H_0^2}$$

gives:

$$\Omega_R = 2.4 \times 10^{-5}h^{-2}.$$

For neutrinos we obtain, in an analogous way:

$$\Omega_\nu \simeq 0.68\ \Omega_R$$

It can be noticed that at present they are both completely negligible; hence the value of Ω seems to be dominated by the effect of dark matter.

What kind of matter do we observe by measuring hydrogen speed in galaxies?

According to the best census, the visible part of ordinary matter (that associated with stars) contributes only about 1% of the total. What we can see with telescopes is literally the tip of an enormous iceberg.

Although the hypothesis that dark matter holds together galaxies has been around for a long time, the nature of the DM in the Universe is still unknown. In fact, we still speak with more certainty about what dark matter is known not to be. Based upon simple accounting, we have eliminated all but the possibility of dark matter being made of neutrons and protons, and established a strong case for a new form of matter.

Baryonic dark matter

The estimation of ordinary matter involves three different methods, all of which give the same answer. The most accurate of these methods comes from considering the formation of light elements during Big Bang nucleosynthesis, ^4He, D, ^3He and ^7Li produced in the first few minutes after the Big Bang. However, only if the density of ordinary baryons is within a narrow range is the predicted production consistent with what we actually measure. The production of Deuterium is the most sensitive indicator of the baryon density. Recent measurements of the Deuterium to Hydrogen ratio, together with predictions from standard Big Bang nucleosynthesis give [17]:

$$\Omega_B h^2 = 0.019 \pm 0.001.$$

Two other determinations are consistent with the nucleosynthesis argument: first, the net absorption of light emitted from very distant quasars by intervening gas indicates a similar value for the baryonic density ($\rho_B = (3.8 \pm 0.2) \times 10^{-31}\ g/cm^3 \simeq 4\%\ \rho_C$). This probes ordinary matter at a time and a place when the bulk of the baryons are still expected to still be in gaseous form. The second constraint comes from measurements of the CMB, which yield an independent baryon density consistent with that determined from nucleosynthesis. Our best accounting of ordinary matter comes from this early time before many stars had yet formed.

Our evaluation of baryons at the present epoch is not as complete. Baryons in star account for only about 1/4 of all the baryons; the rest are optically dark.

Among the many proposed candidates for dark matter there are MACHOs (massive astrophysical compact halo objects), i.e. astronomical objects which do not emit electromagnetic waves; primordial black holes, brown dwarfs, white dwarfs, neutron stars and planet-like objects. These objects can be observed by means of *gravitational lenses.* The MACHO collaboration has observed over 8.5 million stars in the *LMC* galaxy (Large Magellanic Cloud) and found 8 candidate MACHOs. Their conclusion was that objects with a mass between 0.05 e 1 $M_\odot$ account for $0.2 \div 0.5\%$ of the total mass of our galaxy. It follows that MACHOs alone cannot account for all the baryonic dark matter of our galaxy and the solution of this mystery must be searched elsewhere.

While not all of the dark baryons are accounted for, baryonic dark matter itself only weighs for about 1/10 of all dark matter.

Non-baryonic dark matter

A possible way out of the dark matter problem, proposed a long time ago is to assume that neutrinos have a mass. In fact, it was realized that if their mass is in the range *10-50 eV*, the enormous amount of neutrinos created during the Big Bang could explain all non-baryonic dark matter of the Universe. Although in the Standard Model neutrinos have zero rest mass, many extensions exist in which they are massive. In this case their contribution to Ω would be given by:

$$\Omega_\nu = \frac{\sum_{i=1}^{3} m_{\nu i}(eV)}{92h^2}$$

Different experiments, studying solar, atmospheric and reactor neutrinos, now provide evidence that neutrinos have mass; they have placed a lower limit on the mass of the heaviest neutrino at about 0.05 eV. This implies that neutrinos contribute at most for the 0.1% of the mass-energy of the Universe.

What then is this non-baryonic dark matter?

The working hypothesis is that it is formed by weakly interacting elementary particles produced in the early Universe. Before discussing specific particle candidates, we shall review the constraints from astrophysical observations. Since dark matter is diffusely distributed in external halos around individual galaxies or in a sea through which cluster galaxies move, dark matter particles must not interact with ordinary matter very much, if at all; moreover we can be confident that they are uncharged and have only very weak interactions. In addition, the formation of structures in the Universe tells us that early after the Big Bang dark matter particles must have been cold (i.e., moving at non-relativistic speeds) rather than hot (i.e., moving relativistically). In fact, if the dark matter had been hot, then these fast-moving particles would have smoothed out the smaller density irregularities (the seeds for the formation of galaxies and clusters) by streaming from high-density regions to low-density regions. The first objects to form would have been the largest structures (the super-clusters) and small objects (galaxies) would have only formed later by fragmentation. However, this is inconsistent with observations. The deep image of the sky obtained by the Hubble Deep Field in 1995, along with other observations by ground-based telescopes, identified the epoch when most galaxies formed as a few billion years after the Big Bang ($z \sim 1 \div 3$). The Sloan Digital Sky Survey, as well as x-ray observations, have shown that clusters form later ($z < 1$). Finally super-clusters are forming just today. This sequence is inconsistent with hot dark matter.

The leading candidates for the cold dark matter particles are the *axion* and the *neutralino*, two hypothetical elementary particles. If they exist, these particles would have been produced in the earliest moments of the Universe, and survived in sufficient numbers to account for dark matter. Both are new forms of stable matter, predicted to exist by theories that attempt to unify the forces of Nature. But they have wildly different masses: a trillion times smaller than that of the electron for the axion, and a hundred times larger than the mass of the proton for the neutralino. If the cold dark matter hypothesis is correct, then the halo of our Milky Way should be awash in axions or neutralinos.

1.4 Weakly-Interacting Massive Particles

A promising WIMP candidate comes from electroweak-scale supersymmetry (SUSY). SUSY was hypothesized in particle physics to cure the naturalness problem with fundamental Higgs bosons at the electroweak scale. Coupling-constant unification at the GUT scale seems to be improved with SUSY, and SUSY is an essential ingredient in theories that unify gravity with the other three fundamental forces.

It is usually assumed that the lightest supersymmetric particle is the *neutralino* (χ). This should be a linear superposition of the supersymmetric partners of the photon, the Z and of the two neutral and $CP-even\ Higgs$ boson predicted by the *Minimal Supersymmetric Standard Model* (*MSSM*).

In supersymmetric theories R-parity is conserved: supersymmetric particles have $R=-1$, while the others have $R=1$. In particular the neutralino, being the lightest supersymmetric particle, cannot decay in other supersymmetric particles, nor into $R=+1$ particles.

The fact that the neutralino is stable opens up the possibility that neutralinos are still present in the Universe as a cosmological relic.

An approximate solution to the Boltzmann equation yields the cosmological WIMP abundance (in units of the critical density ρ_c):

$$\Omega_\chi = \frac{m_\chi n_\chi}{\rho_c h^2} = \frac{3\times 10^{-27}\ cm^3/s}{<\sigma_A v>} h^{-2} \tag{1.5}$$

Depending on the mass of the χ, the Global-SUSY models predict different abundances consistently with the hypothesis that neutralinos are the explanation of dark matter.

The present knowledge gives the following picture for the evolution of the Universe: immediately after the Big Bang, all matter is hot (relativistic); the Universe cools down during the expansion until it reaches the temperature at which SUSY symmetry is broken ($\sim$ 1 TeV): particles decouple from s-particles and, the latter being heavy, become quickly non-relativistic and begin to arrange themselves in structures, due to gravity. Interacting as a self-gravitating isothermic gas, the s-particles form relatively small structures: the future galactic halos. During the expansion of the Universe, at a given temperature baryons decouple from radiation and are attracted inside the cold dark matter objects to form galaxies.

Neutralinos can be detected in the following channels:

- direct searches:

  $\Rightarrow$ elastic scattering on nuclei;

- indirect searches:

  $\Rightarrow$ $\chi - \chi$ annihilation inside the Sun or the Earth:

  · neutrino flux (ν's are the only visible annihilation products);

  $\Rightarrow$ $\chi - \chi$ annihilation in the galactic halo:

  · ν fluxes and $\overline{\nu}$ with high directional density;

  · a line in the diffuse γ spectrum from galactic plane;

  · greater abundance of rare components ($\overline{p}$ and e^+) in cosmic rays.

1.5 Direct neutralino searches

According to theoretical models, the neutralino mass is between 20 GeV and 1 TeV; LEP has established a lower experimental limit of 34 GeV. The neutralino could be a weakly interacting massive particle (WIMP); various groups do not use particle accelerators to find them. WIMPs would be created during the Big Bang and should surround the Earth because of their gravitational interaction with matter. Due to their weak interaction with matter they are extremely difficult to detect. However there is the possibility that some of them undergo elastic scattering with nuclei.

The recoil energy depends on the mass and velocity of the WIMP and on the mass of the target nucleus. The number of elastic collisions decreases exponentially with the recoil energy. The maximum energy transfer is obtained when the WIMP and the target nucleus have the same mass:

$$E_R = \frac{m^2 v^2}{m_N}(1 - cos\theta) \qquad\qquad m = \frac{m_W m_N}{m_W + m_N}$$

(E_R: recoil energy; v: WIMP velocity; m_W: WIMP mass; m_N: mass of target nucleus). The use of several different nuclei as targets thus allows to cover a large mass range with great sensitivity.

The recoil energy can be observed in different ways, depending on the target composition:

· temperature increase in cryogenic detectors;

· ionization;

· scintillation.

To be sensitive to WIMPs, the detector must be sensitive to energy releases of the order of 10 keV. The expected event rate is only one per day per 10 kg of detector mass. Moreover for each WIMP interaction, there are millions of background events due to cosmic rays and radioactivity of the detector itself and of its surroundings. For these reasons the discriminating requirement for the direct detection of WIMPs are:

⇒ annual modulation of the signal

⇒ daily modulation of the signal

⇒ directionality of the interaction.

The results of the DAMA collaboration have recently been published [18]. The detector, located in the Gran Sasso National Laboratories (INFN), consists of 100 kg of highly radio-pure $NaI(Tl)$. Data have been collected for seven annual cycles up to July 2002 for a total of 107731 $kg \cdot day$.

In particular DAMA has studied the annual modulation of its signals. According to standard models, the WIMPs velocities ($\overline{v} \sim 230 \pm 50\ km/s$) in the galactic halo should follow a Maxwell distribution, with a cut-off equal to the galactic escape velocity ($\sim 500\ km/s$). Consequently the Earth should constantly be swept by a WIMP "wind". Because of the rotation of the Earth around the Sun, it should be possible to point out an *annual modulation* of the signal of WIMPs interactions; the WIMP flux through the Earth should be greater in June (when the rotation velocity of the Earth sums up to that of the Solar System with respect to the galaxy) than in December (when the two velocities are opposite). Since the most probable recoil energy of a nucleus for an elastic scattering is proportional to the incident WIMP velocity, different peak recoil energy values should be observed in June and December.

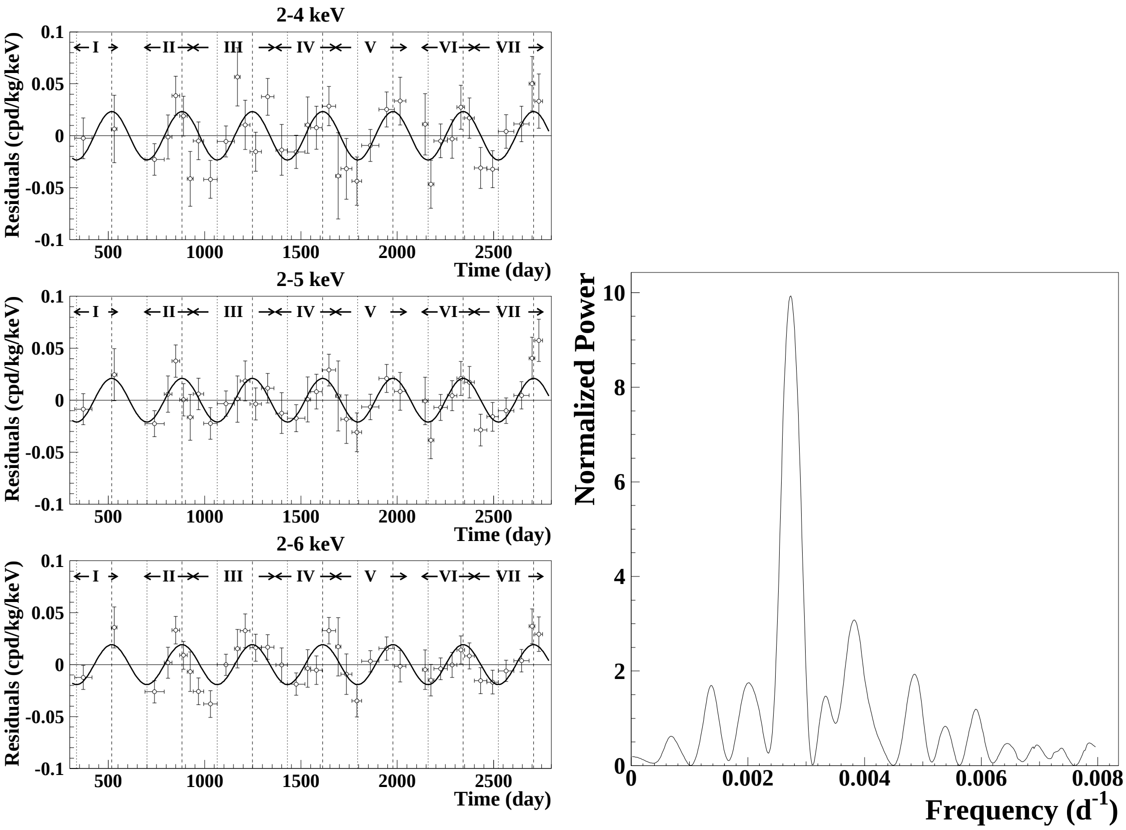

Figure 1.8: *On the left:* experimental residual rate for *single-hit* events in the $(2 \div 4)$, $(2 \div 5)$, and $(2 \div 6)$ keV energy intervals as a function of the time, over 7 annual cycles. The experimental points present the errors as vertical bars and the associated time bin width as horizontal bars. The superimposed curves represent the cosinusoidal behaviors expected for a WIMP signal with a period equal to 1 year and phase at 2^{nd} June; the modulation amplitudes have been obtained by best fit. *On the right:* power spectrum of the measurements in the $(2 \div 6)$ keV region. As it can be seen, the principal mode corresponds to a frequency of $2.737 \times 10^{-3}\ d^{-1}$, that is to a period of 365.36 days $\simeq$ 1 year.

The data collected by DAMA show an annual modulation consistent with the expectations from WIMPs. The analysis of all available data (Fig.1.8) favors the presence of a modulated cosine-like behavior $(A \cdot \cos\omega(t - t_0))$ at 6.3 σ $C.L.$. A fit to the $(2 \div 6)$ keV largest statistics energy interval, yields a modulation amplitude equal to (0.0200 ± 0.0032) $cpd/kg/keV$, $t_0 = (140 \pm 22)$ $days$ and $T = 2\pi/\omega = (1.00 \pm 0.01)$ $year$, all parameters being kept free in the fit.

A different experiment (the CDMS collaboration [19]) is studying the direct signal of WIMPs by measuring the temperature increase in silicon and germanium crystals. The energy detection threshold is 10 keV but with the currently available statistics CDMS can only determine an exclusion region in the plane $\sigma - M_W$ (Fig 1.9) which, however, does not completely cover the DAMA region.

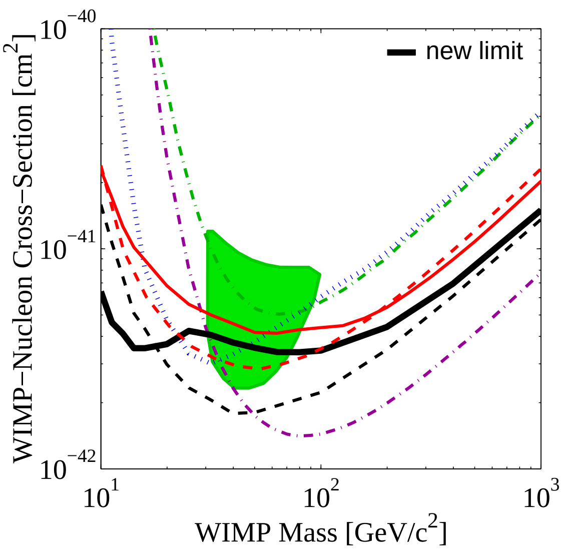

Figure 1.9: The region above the black curve is excluded at 90% $C.L.$ by CDMS. The green shaded region is the DAMA 3σ allowed region.

1.6 Indirect neutralino searches

Neutralinos can also be detected by indirect methods by looking at annihilation products [20].

Neutralinos are Majorana particles formed by a superposition of *photino*, *Higgsino* and *Zino*; the relative weights of these particles depend on three parameters of the SUSY model and as they are changed neutralinos can annihilate in different channels. The secondary products of neutralino annihilations could be stable particles like p, $\overline{p}$, e^+, e^-, γ, ν.

The effects in the photon and neutrino channels have very peculiar signatures which will make the identification easy. Photons can be produced in $\chi\chi \rightarrow \gamma\gamma$ or $\chi\chi \rightarrow Z\gamma$ annihilations so their energies are well defined. In fact all such γs should have the same energy equal to $E_\gamma = m_\chi$, or $E_\gamma = m_\chi(1 - \frac{m_Z^2}{4m_\chi^2})$ in the second case, since the neutralino velocities in the halo are of order $10^{-3} \cdot c$ so that the annihilation can be considered at rest.

Neutrinos, on the other hand, should be originated from the center of the Earth or from the Sun, where the predicted neutralino density is higher due to gravitational interaction.

The rates of both processes is difficult to estimate, because of uncertainties on the supersymmetry parameters, on the cross sections, and on the density of the halo; nonetheless the identification criteria are very strong: the flux direction for neutrinos and the energy for photons.

The continuum spectrum of photons could also provide a good signal [21] since the average angular distribution should follow that of dark matter in the halo, contrary to the background emitted mainly by the galactic disk (cosmic rays produce gamma rays interacting with interstellar hydrogen). Results by EGRET indicate an excess of gamma rays in the GeV region coming from the halo. However other possible explanations for this effect also exists (i.e. π^0 production from cosmic rays escaped from the disk) and further investigation is needed to understand the observations. Experiments such as GLAST and ACT (Air Cerenkov Telescope) should provide, in future, results in this direction.

Indirect searches for neutralinos is not easier than direct measurement.

Stable particles produced by "conventional" sources are also present in cosmic rays. Their abundances and energy spectrum are described by the *leaky-box* model of cosmic ray propagation and interaction in space. Neutralino annihilations must be searched as an excess of a given particle species above a level determined by the production from conventional sources. As an example, consider the case of a light neutralino; annihilation to gluon pairs should then be possible and from their fragmentation antiprotons can be obtained with a known probability. If the neutralino mass were about 30 GeV, evidence should be observed in the ratio $\overline{p}/p$ at low energies ($\lesssim$100 MeV). If, on the contrary, its mass were greater than 60 GeV, the signal in this channel should be too small compared to that due to standard sources. In the case of a very high neutralino mass ($\lesssim$1 TeV) the signal should be visible again.

For heavy neutralinos (80÷500 GeV) the preferred channel for secondary annihilation products is into a positron. The study of the positron spectrum is one the main goals of **AMS-02**.

1.6.1 The signal in the positron channel

Neutralino annihilation in the galactic halo can produce a visible signal in the ratio between the positron and the positron plus electron flux (positron fraction). The competitive background was studied by means of the leaky-box propagation model for cosmic rays. The electron flux, in the energy range 10 GeV - 2 TeV, is described (within a factor of two) by the following formula:

$$\frac{d\mathcal{F}_-}{dE} \simeq 0,07 \left(\frac{E}{GeV}\right)^{-3,3} cm^{-2} sr^{-1} GeV^{-1} sec^{-1}.$$

For energies greater than a few GeV, the measured positron flux is $\sim 3\% \div 5\%$ of the electron one, and is consistent with the expectations for conventional sources. The dominant background sources are interactions of protons and Helium nuclei from primary cosmic rays with the interstellar medium nuclei: π^+ are produced whose decay increases the positron flux. As stated above, the search for the neutralino annihilation signal is done by studying the positron fraction; the estimate of the background due to standard sources has the form:

$$\frac{d\mathcal{F}_+/dE}{d\mathcal{F}_+/dE + d\mathcal{F}_-/dE} = 0,02 + 0,10 \left(\frac{E}{GeV}\right)^{-0,5}.$$

At energies below 10 GeV, however, this background is subject to large uncertainties because of the effects of the solar wind. The soft positron spectrum also varies depending on the orbit path of the experiment. At high energies, these effects are negligible. In addition, positrons lose energy through a variety of processes, therefore hard positrons must typically have been produced within a few *kpc*. For this reason, the hard spectrum is relatively insensitive to variations in the halo profile near the galactic center. The dark matter signal is therefore most promising at high energies, where the background is relatively small and well understood.

The signal is easier to identify if the neutralino is in a pure Higgsino state [22]. In fact, the annihilations of a neutralino of this kind can increase the positron flux in two ways. The first channel is through direct decay of gauge bosons:

$$\chi\chi \to W^+W^- \qquad \chi\chi \to Z^0Z^0$$

$$W^+ \to e^+\nu \qquad Z^0 \to e^+e^-$$

(the branching ratio for the W^+ decay in e^+ is $\sim$ 11%, while for the Z^0 is $\sim$ 3%). Neutralinos in the galactic halo have a velocity of the order of $10^{-3} \cdot c$, thus annihilations can be considered at rest. In this case, positrons originating from direct decays of gauge bosons will have an average energy equal to half the neutralino mass ($m_\chi/2$). Their spectrum will present a very peculiar shape, characterized by a steep drop when the energy increases and reaches zero at an energy value equal to the neutralino mass. The steep descent should provide a strong signature for this signal allowing an easy identification. The signal should appear as a peak in the ratio between the positron flux and the combined flux of positron and electrons. The second production channel of positrons via annihilations of Higgsino-kind neutralinos is given by secondary decays of gauge bosons:

$$W^+ \to \tau^+ \to e^+$$

$$W^+ \to \mu^+ \to e^+$$

$$W^+ \to (\text{b and c quarks}) \to e^+$$

or, the final products of a cascade of charged pions resulting from the hadronization of quarks coming from decays of the gauge bosons ($\pi^+ \to \mu^+ \to e^+$). The positrons produced by pions are ten times more than those from decays of gauge bosons; this fact however would not hide the possible signal discussed above because the energies of “secondary” positrons are lower. In fact, this second production channel of positrons contributes with a broader spectrum peaked at an energy corresponding to one twentieth of the neutralino mass ($m_\chi/20$).

In the case of neutralinos that are not a in a pure Higgsino state, the annihilations into vector bosons are not favored. Leptons and heavy quarks should give the dominant contribution since the annihilation cross section of neutralinos into fermions is proportional to their mass:

$$\sigma \propto \left(\frac{m_f}{m_\chi}\right)^2.$$

The main contribution to the signal are the following:

$$\chi\chi \to t\bar{t}, \qquad \chi\chi \to b\bar{b}, \qquad \chi\chi \to \tau^+\tau^-.$$

We notice that the most energetic positrons are produced by annihilations into gauge bosons of Higgsino-like neutralinos.

The differential positron fraction in this case in shown in Figure 1.10 using the cross sections of a pure Higgsino [23]. It is seen that the predicted signal/background ratio has a maximum for $m_\chi \sim m_W$. Moreover it seems that for neutralino masses of the order of $\simeq 100\ GeV$ the signal would be experimentally detectable. However the relic abundances of this kind of neutralinos are not enough to explain the dark matter.

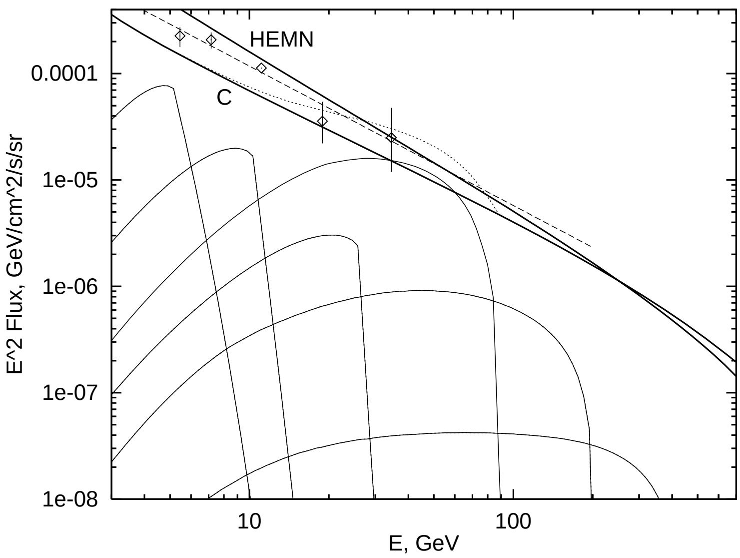

Figure 1.10: The predictions for two CR positron "background" models (C and HEMN: heavy solid lines), and positron signals from neutralino annihilation for m_χ = 5.15, 10.3, 25.8, 103.0, 206.1, 412.1 (thin solid lines) In the case of $m_\chi = 103.0\ GeV$, the signal plus background (model C) is shown by the dotted line.

As can be seen from Figures 1.11 the pure Higgsino case corresponds to a gaugino fraction $<$ 10% (see *Middle*) which is outside of the light blue region corresponding to sensible values of the relic abundances ($0.1 \leq \Omega_\chi h^2 \leq 0.3$). In fact, as shown in Eq. 1.5, Ω_χ is inversely proportional to $\sigma_A v$ which (see *Bottom*) has a maximum in the pure Higgsino case.

Higgsino-like dark matter is highly disfavored unless it is unnaturally heavy, it annihilates too strongly to leave interesting relic abundances.

Imposing the constraint that $\Omega_\chi h^2 \simeq 0.15$ [24] the signal rates are significantly suppressed as shown by the curves in Figure 1.12.

Several years ago the HEAT collaboration reported an excess of cosmic ray positrons with energies $\sim$ 10 GeV [25]; in the year 2000 they again measured this excess using a new instrument, and found excellent agreement [26] with the previous result. The possibility that this excess is due to annihilations of neutralinos in supersymmetric models, has been investigated by many authors.

Some of them, in one of the most recent publication [27], confirm that neutralino annihilation can produce enough positrons to explain the measured excess if there is an additional enhancement to the expected signal. They quantify the "boost factor" that is required in the signal for various models in the Minimal Supersymmetric Standard Model parameter space, and find that a boost factor ≥ 30 provides good fits to the HEAT data. Such an enhancement in the signal could arise if we live in a clumpy halo. Since the structure of the galactic dark halo is unknown, there is no compelling argument for any particular value of the enhancement factor, be it unity or in the thousands or more.

In Fig. 1.13 is shown the positron data from the HEAT 94+95 and HEAT 2000 experiments, together with a fit assuming only background, and two interesting SUSY model predictions that provide good fits. The apparent sharp increase in the positron fraction around 7 GeV is not evident in any of our SUSY models, even before the smoothing effects of energy loss on the spectrum. In principle one could envision a sharp edge coming from the direct decay of gauge bosons. However, we would then get positrons also from the hadronic decay of the gauge bosons and this would entirely dominate the flux at 7 GeV as seen in Fig. 1.13 *bottom*.

They have explored models in the Minimal Supersymmetric Standard Model (MSSM) parameter space to find how large the boost factor (B_s) must be for each of the models. The lowest boost factor found is roughly 30 for a WIMP that is primarily a Bino in content with mass 160 GeV. For $B_s < 100$ the models are gaugino-dominated, though some have significant Higgsino fractions. The masses of the models are in the range $150 \div 400$ GeV for the most part. For $100 < B_s < 1000$,

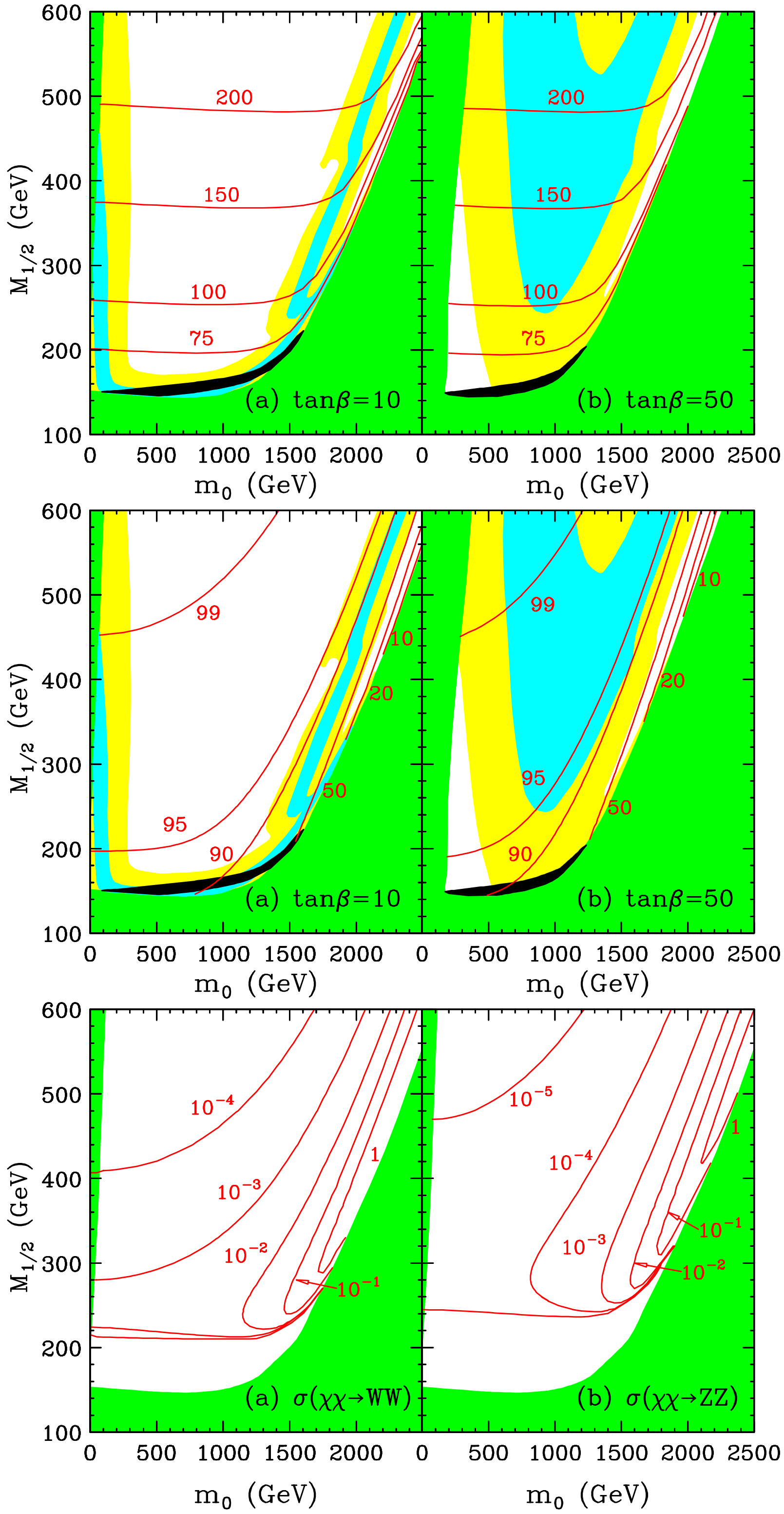

Figure 1.11: Contours plots in the $(m_0, M_{1/2})$ plane. The green shaded regions are excluded by the requirement that the LSP be neutral (left) and by the chargino mass limit of 95 GeV (bottom and right). The regions with potentially interesting values of the LSP relic abundance are also delineated: $0.025 \leq \Omega_\chi h^2 \leq 1$ (yellow) and $0.1 \leq \Omega_\chi h^2 \leq 0.3$ (light blue). *Top*: Contours of constant neutralino mass m_χ in GeV. *Middle*: gaugino fraction in percent. *Bottom*: Contours of constant σv in pb for (a) $\chi\chi \to WW$ and (b) $\chi\chi \to ZZ$.

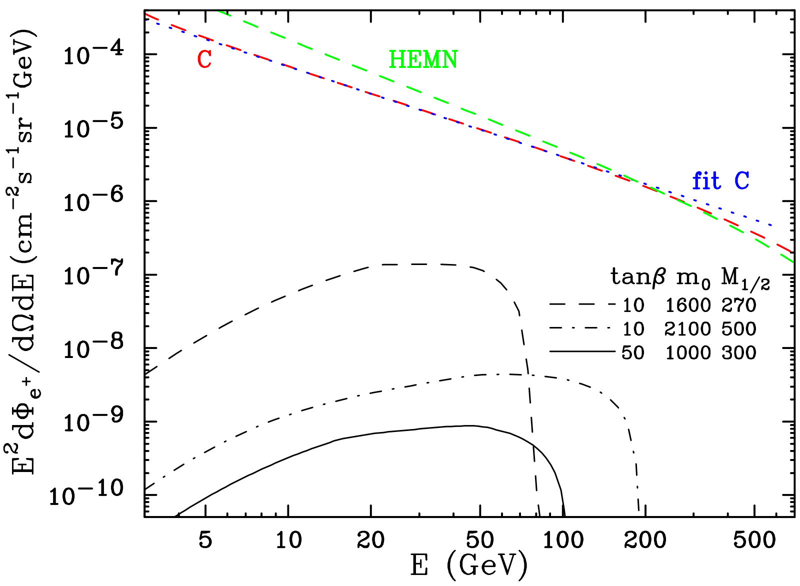

Figure 1.12: The differential positron flux for three sets of the SUSY parameters ($\tan\beta$, m_0, $M_{1/2}$). The curves labeled C and HEMN are background models from Ref. [23]; the dotted curve is the fit to C.

the masses are as large as 2 TeV, and some very pure Higgsinos become allowed.

Fits to the new HEAT data with positrons from supersymmetric dark matter have been made by other groups, which come to more or less the same conclusions, i.e. that large boost factors are needed and that the fits are better than the background-only fits, though not excellent.

As can be seen from these Figures the currently available data do not allow to establish the presence, and possibly the type, of signal with confidence. One of the main purposes of **AMS-02** is then to study the positron fraction with greater resolution and at higher energies, i.e. in the region where a potential signal should be stronger.

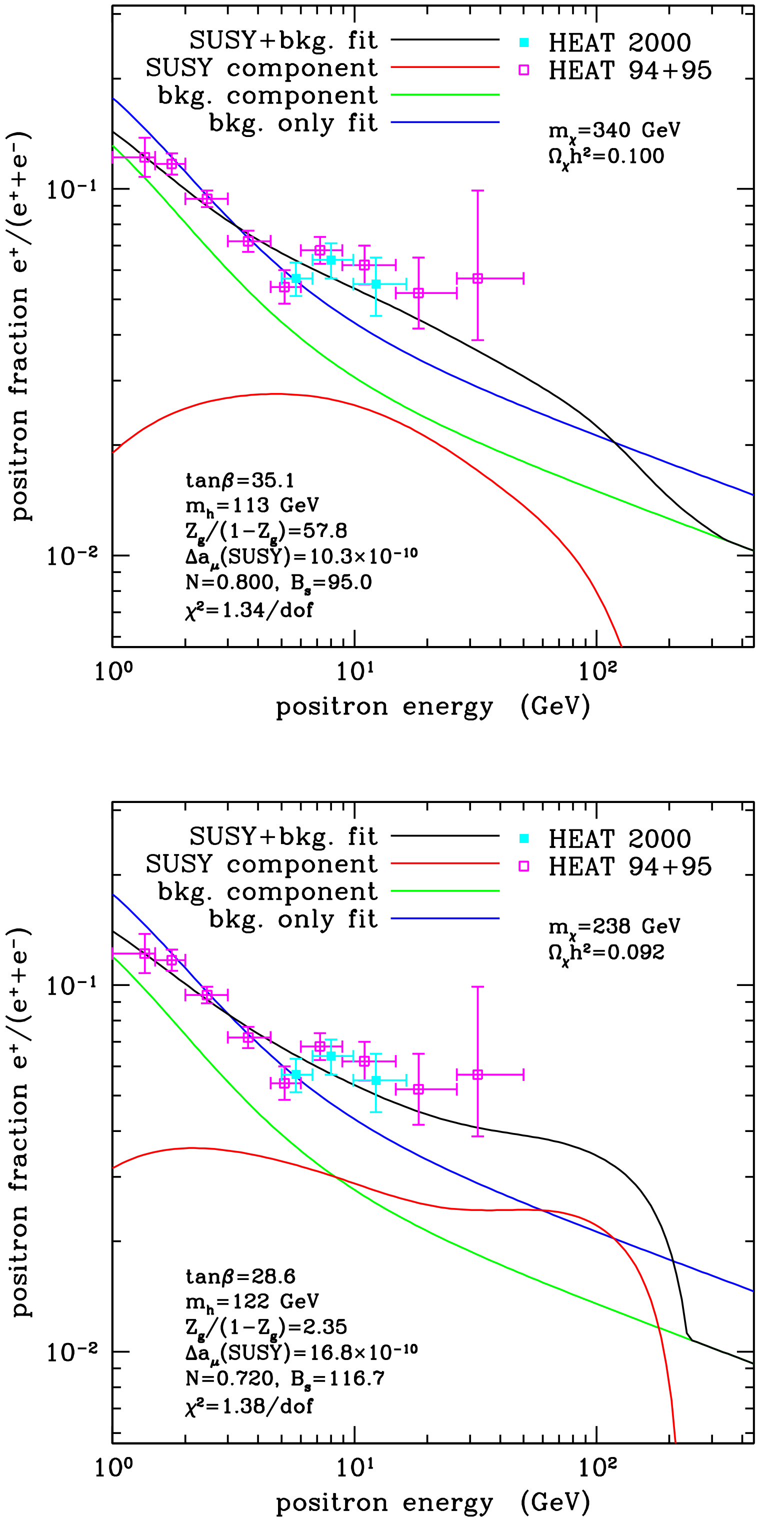

Figure 1.13: Positron fraction data and fits. Here are shown the positron data from HEAT 94+95 and HEAT 2000, a background only fit, and a SUSY+background fit for two interesting MSSM models. Two additional curves separately display the SUSY and background components of the combined SUSY+background fit. These models are gaugino dominated and the model on *top* has positrons primarily from hadronization, while the model on *bottom* has hard positrons from direct gauge boson decays.

Chapter 2

The AMS experiment

The *Alpha Magnetic Spectrometer* (**AMS**) is a particle detector aimed at high precision measurements of cosmic ray fluxes in Space. It will be part of the scientific program on board the International Space Station (ISS), where it will collect data for three years. The AMS experiment's main goals are:

· search for cosmic antimatter nuclei;

· search for dark matter signatures;

· measurements of cosmic ray spectra in the energy range from a few GeV up to $1\ TeV$.

The precursor experiment **AMS-01** was boarded on the space shuttle Discovery, flight STS-91 for 10 days in June 1998; the detector has been operative for about 180 hours, collecting over one hundred million cosmic ray events.

The improved version of the detector, called **AMS-02**, will be installed aboard the ISS. In addition to a refined silicon tracker and a redesigned Time Of Flight (TOF) and anti-coincidence systems, a proximity focusing Ring Imaging ČHerenkov (RICH) detector will replace the threshold Čherenkov counter of AMS-01, and two additional subdetectors, a Transition Radiation Detector (TRD) and an Electromagnetic CALorimeter (ECAL), will be added to improve the proton-electron separation capability of the instrument.

2.1 Particle identification

In order to measure the fluxes of cosmic ray particles, the detector has to be able to measure their charge, velocity and *rigidity*:

$$R = \frac{pc}{ze} = \gamma\beta\frac{m_0 c^2}{ze} \tag{2.1}$$

where p and ze are the relativistic momentum and the particle charge respectively, m_0 is its rest mass, c is the speed of light, $v = \beta c$ is the particle velocity and $\gamma = (1 - \beta^2)^{-1/2}$ is the Lorentz factor.

In principle, when z, β and R are known, it is possible to obtain the particle rest mass m_0 from the relation 2.1 and the particle identification is complete. In practice, due to experimental uncertainties on those parameters, mass discrimination between two given particle species may be allowed only in some rigidity or energy range. In particular, it is easier to separate electrons from protons ($m_p \simeq 1837\ m_e$) than protons from deuteron's ($m_d \simeq 2\ m_p$), and the latter are better separated than any other pair of nuclear isotopes.

A particle with charge z and rigidity R, moving through a region where a uniform magnetic field B exists, will follow a helix with radius of curvature:

$$r = \frac{R}{Bc}\sin\theta\ ,$$

where θ is the angle between the particle momentum and the magnetic field. If the field is not perfectly homogeneous, as in the case of the AMS detector, the trajectory is more complicated but, in any case, it depends only on the particle instantaneous rigidity and the local magnetic field. Hence, if the field is known, in order to measure the particle rigidity one has to reconstruct its trajectory, keeping into account the energy lost within the detector (that will decrease the instantaneous radius of curvature).

The tracking system of AMS is a silicon detector with N planes ($N = 6$ for AMS-01, $N = 8$ for AMS-02) that are able to measure the (x, y) coordinates of the crossing points and the energy lost by the particle by ionization of the active material. If the spatial resolution of the tracking system is σ_{pos} and the magnetic field strength along the particle trajectory is $s_{mag} = \int \mathbf{B} \cdot \mathbf{dl}$, the relative uncertainty on the rigidity is:

$$\frac{\Delta R}{R} \propto \frac{R\sigma_{pos}}{s_{mag}}\frac{1}{\sqrt{N+4}}$$

that is, the "deflection" $\eta = 1/R$ is Gaussian distributed.

It is customary to define the *Maximum Detectable Rigidity* (MDR) the rigidity for which the measurement uncertainty is 100% (that is $\Delta R/R = 1$). The MDR for protons is 150 GV in AMS-01 and will reach 1 TV in AMS-02. When the particle rigidity is comparable with the MDR of the instrument (i.e. the deflection tends to zero), it becomes likely that the wrong deflection sign will be attributed to the trajectory ("spillover"). The spillover causes two problems: first, it produces fake antiparticles; second, it leads to a distortion of the measured rigidity spectrum, that will appear steeper due a disappearance of events from the highest rigidity bins.

When the particle rigidity is known, in order to obtain the momentum it is necessary to measure its charge. The sign of the charge is found by looking at the track curvature (measured by the tracker) and direction (obtained by the TOF system) in the magnetic field, while its absolute value is given by the energy lost in the active parts of the detector. Given a particle with charge z and velocity βc, the average energy lost after a path length $d\xi = \rho dx$ through a medium with density ρ, atomic and mass numbers Z and A respectively, is given by the corrected Bethe-Bloch formula:

$$-\frac{dE}{d\xi} = Kz^2 \frac{Z}{A} \frac{1}{\beta^2} \left[\frac{1}{2} ln \frac{2m_e c^2 (\beta\gamma)^2 T_{max}}{< I >^2} - \beta^2 - \frac{\delta}{2} \right]. \qquad (2.2)$$

Formula 2.2 can be used to infer the particle charge $|z|$ from the energy deposition measurements in the TOF and tracker layers if the particle velocity β is known.

Two techniques can be used by AMS-02 to determine the particle velocity: measurements of the time of flight and of the Čherenkov cone opening angle.

The first method is used by the TOF system: a particle with velocity $v = \beta c$ takes a time $t = l/v$ to cover a distance $l = L/\cos\theta$ between the upper and lower TOF planes (L is their distance and θ is the trajectory colatitude angle). The time of flight is given by:

$$t = \frac{L}{\beta c \ \cos\theta}$$

and its uncertainty σ_t is Gaussian. The uncertainty on β will be:

$$\sigma_\beta^2 = \frac{L^2}{c^2} \left(\frac{\sigma_t^2}{t^4 \cos^2\theta} + \frac{\sigma_\theta^2 \sin^2\theta}{t^2 \cos^4\theta} \right) \simeq \frac{L^2}{c^2} \frac{\sigma_t^2}{t^4 \cos^2\theta},$$

since the second term inside the parenthesis can be safely neglected both in AMS-01 and AMS-02 thanks to the excellent angular resolution of the tracker. The time resolution of the TOF system is of order of 0.1 ns, hence the time measurement can be used to infer the particle velocity up to about $\beta \simeq 0.95$.

On the other hand, a direct measurement at higher β can be done exploiting the RICH detector of AMS-02, that will have a relative precision of $\Delta\beta/\beta \simeq 0.1\%$. The Čherenkov radiation, produced by charged particles with velocity greater than the local phase velocity of light in the medium, is emitted over the surface of a cone whose axis is the particle momentum direction. The cone opening angle 2α depends only on the refractive index of the medium and the particle velocity:

$$\cos\alpha = \frac{1}{\beta n}.$$

Below the threshold given by:

$$\beta_{min} = 1/n.$$

there is no Čherenkov emission at all.

2.2 The AMS-01 detector and results

Figure 2.1 shows the AMS-01 detector that was flown aboard the shuttle Discovery on June 1998 during a ten-day mission. The instrument was operative for about 180 hours and has collected over one hundred million events in the energy interval $0.1 \div 200$ GeV. The space shuttle orbited at an altitude of about $370 \div 390$ km and covered all the longitudes and latitudes within $\pm 51.7°$.

The AMS-01 detector

The core of the instrument is a permanent Nd-Fe-B magnet enclosing the tracking system and an Anti-Coincidence Counter (ACC) system.

The AMS-01 permanent magnet produces a roughly constant field with $B_x \simeq$ 1.6 kG within ± 30 cm along the z-axis, and decreases rapidly outside the bore thus limiting the torque resulting from the interaction with the geomagnetic field. The nominal bending power of the magnet is $BL^2 = 0.14$ Tm^2, when considering the average B_x in the range $|z| < 71.4$ cm. Its geometrical acceptance is 0.82 $m^2 sr$ and its weight is 1900 kg.

The silicon tracker consist of 300 μm thick double-sided micro-strip sensors of area 4×7 cm^2. The spatial resolution is 20 μm in the bending and 30 μm in the non-bending direction. The silicon sensors are grouped together in ladders of different

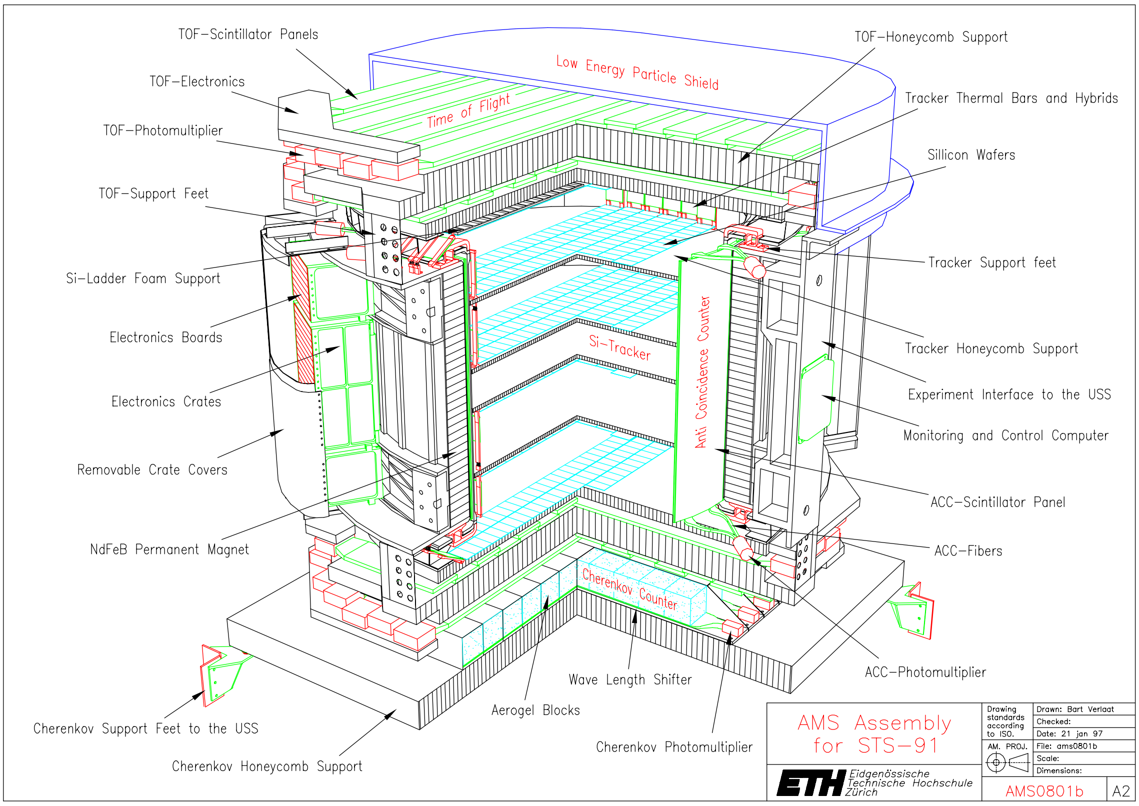

Figure 2.1: The **AMS – 01** detector.

length, assembled on 6 ultra-light honeycomb planes. For vertical tracks, the total amount of matter of the 6 planes is about $0.02 \div 0.03$ radiation lengths.

The tracker was not fully assembled for the test flight in 1998; the ladders were just in the middle of the planes (as shown in Figure 2.1) so the geometrical acceptance was reduced to 0.36 $m^2 sr$.

The momentum resolution of the tracker is limited by multiple scattering at low energies, while at high energies it is limited by the magnet bending power and the tracker spatial resolution. The momentum resolution for protons is at the 7% level between 1 and 10 GeV.

Above and below the magnet, four layers of scintillator counters constitute the time of flight system, which the main goals are to provide the fast trigger to the AMS readout electronics and to measure the particle direction, velocity, position and charge.

The detector consists of 4 planes of plastic scintillator paddles (Bicron BC408), two above and two below the magnet. The counters of adjacent planes are orthogonal, in order to guarantee a certain granularity at the trigger level. Each TOF plane has 14 1 cm thick scintillator counters covering a roughly circular area of 1.6 m^2. The system has a time resolution of about 120 ps and a spatial resolution of about 2 cm.

The Anti-Coincidence Counter (ACC) is used as *veto* by the level-1 trigger in order to discard the events produced by interactions of cosmic ray particles in the magnet structure giving secondaries of opposite charges that are deflected toward the upper and lower TOF planes.

The Aerogel Threshold Čherenkov (ATC) counter mounted below the AMS-01 magnet consists of two layers of 8×10 (upper) and 8×11 (lower) aerogel cells. Directly attached to the universal support structure (USS) rather than to the magnet, as are the other subdetectors.

The ATC is used to improve the separation capability between protons (antiprotons) and positrons (electrons). The number of photons produced by a particle with charge z traveling a distance L_{aero} inside the aerogel, with velocity β above the Čherenkov threshold, is:

$$N_{ph} \propto L_{aero} z^2 \left(1 - \frac{1}{n^2 \beta^2}\right)$$

where n is the refractive index of the radiator. Aerogel was chosen because its refractive index $n = 1.035$ allows the discrimination of protons from electrons up to 3.5 GeV.

The AMS-01 results

The high statistics measurements of cosmic rays in Space performed with the state-of-art AMS magnet spectrometer enabled to measure the flux of cosmic rays with reduced systematics and the highest precision. The mission provided very accurate measurements of all the light (up to Helium) particles fluxes. The collaboration has published results of their analysis on cosmic antimatter [28] and the flux of protons [29, 30], electrons and positrons [31], and Helium [32] in the low orbit environment.

The geomagnetic field acts as a filter for low energy particles: they can penetrate only regions allowed by their charge, momentum and incident direction. On the other hand, soft secondaries produced in the atmosphere will very likely be trapped if their energy is below a certain cut-off. The effect of the geomagnetic cut-off and the decrease of this cut-off with increasing geomagnetic latitude ($|\Theta_M|$) is particularly visible in the downward spectra. Is possible to observe two spectra: a primary one, i.e. above the geomagnetic cut-off, and a second one below the cut-off.

The spectra from particles which are traced to originate far away from Earth are classified as "primary" and those from particles which originate in the atmosphere as "second".

The **primary cosmic rays** are dominated by the proton component as seen in Figure 2.2, which shows the primary spectra of protons, He nuclei, electrons and positrons measured by AMS-01.

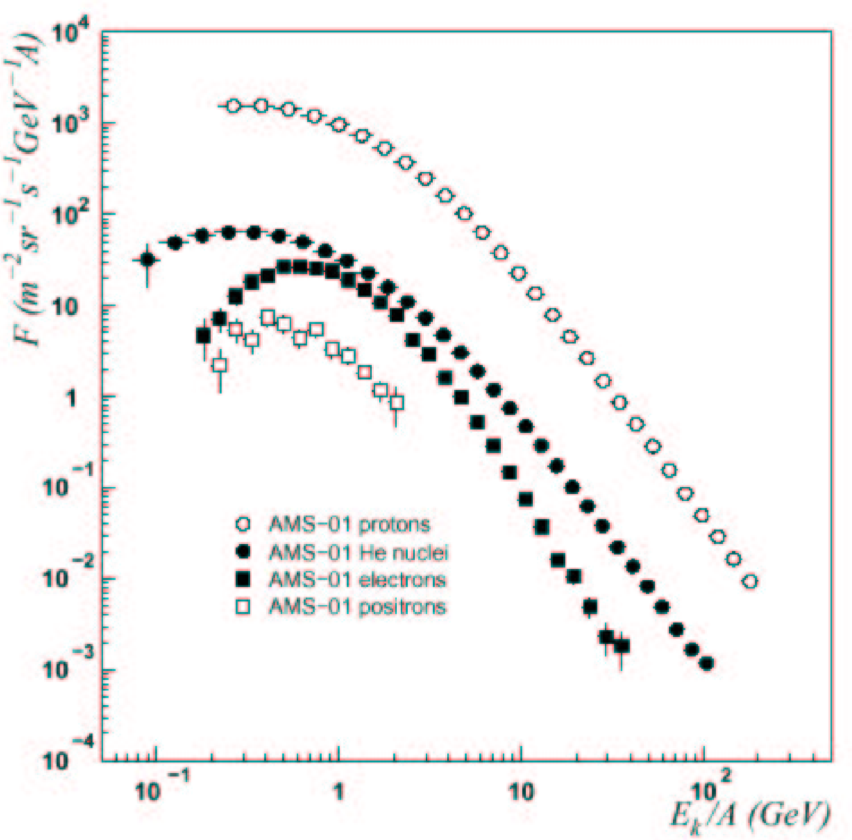

Figure 2.2: Primary fluxes of CR protons, He nuclei, electrons and positrons measured by AMS-01.

The proton differential spectrum measured by AMS-01 can be fit by a power law in rigidity, for $R > 10\ GV$, of the form:

$$\Phi(R) = \Phi_0 R^{-\gamma} \qquad [m^{-2}s^{-1}sr^{-1}MV^{-1}] \tag{2.3}$$

with [30]:

$$\gamma^{(p)} = 2.78 \pm 0.009(fit) \pm 0.019(sys)$$

$$\Phi_0^{(p)} = 17.1 \pm 0.15(fit) \pm 1.3(sys) \pm 1.5(\gamma) \qquad [GV^{2.78}m^{-2}s^{-1}sr^{-1}MV^{-1}].$$

In addition, the He spectrum for $20 < R < 200\ GV$ can be fit by a power law with [32]:

$$\gamma^{(He)} = 2.74 \pm 0.010(stat) \pm 0.016(sys)$$

$$\Phi_0^{(He)} = 2.52 \pm 0.09(stat) \pm 0.13(sys) \pm 0.14(\gamma) \qquad [GV^{2.74}m^{-2}s^{-1}sr^{-1}MV^{-1}].$$

The e^- and e^+ spectra are shown in Figure 2.3 a); AMS-01 collected a large amount of data, and the spectra of electrons and positrons have unprecedented small error bars. While the size of the background does not allow any significant conclusion on the positron spectrum above 1.5 GeV, the measurement of the electrons spectrum is very good up to about 30 GeV. Figure 2.3 b) shows the energy dependence of the positron fraction, which exhibits predominance of the electrons over positron in primary cosmic rays, as expected.

The wide range of geomagnetic coordinates sampled by AMS-01 during the STS-91 Shuttle flight ($|\Theta_M| < 75^0$) allowed a precise measurement of the dependence of the **secondary cosmic ray** component on the geomagnetic field.

The upward and downward proton fluxes were measured at different geomagnetic latitudes. It is evident that for small latitudes (i.e. in the equatorial region) the primary component is damped at low energy by the Earth magnetic field, that reflects back incoming particles having rigidity below a cut-off level that is near 10 GV. This level decreases at increasing latitudes. However, the spectrum shows a dip and starts to rise again below few GV. In addition, this second part of the spectrum is the same for upward and downward protons, indicating that it is due to particles that are looping in the geomagnetic field.

Using the large He sample collected by AMS, a search for **anti-Helium** candidates have been performed. The procedure to search for $\overline{He}$ begins with event reconstruction, which include: the measurement of the particle rigidity, R, from the deflection of the trajectory measured by the tracker in the magnetic field; the measurement of the particle velocity, β, and direction, from the TOF and the determination of the magnitude of the particle charge, $|z|$, from the measurements of energy losses in the TOF counters and tracker planes (including β corrections).

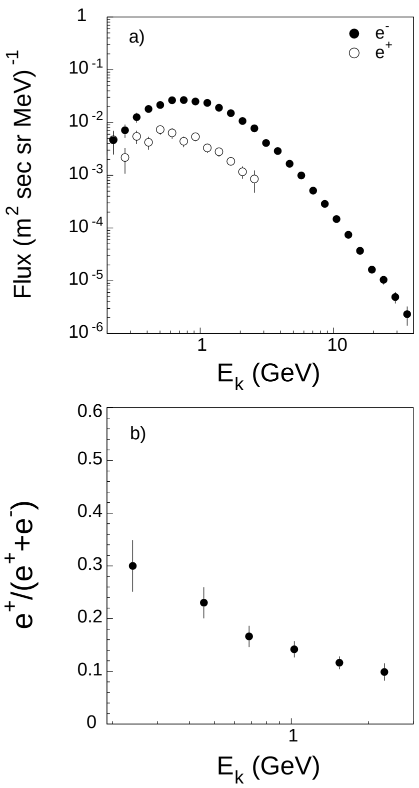

Figure 2.3: AMS-01 primary fluxes of electrons and positrons a) and relative abundances b) [31].

Within 2.86 millions He events, no $\overline{He}$ candidates were found in the energy interval $1 \div 140\ GeV$.

This result allows to set an upper limit on the anti-helium flux; if the incident $\overline{He}$ spectrum is assumed to have the same shape as the He spectrum over the range $1 < R < 140\ GV$, then an upper limit of $\mathbf{1.1 \times 10^{-6}}$ is obtained.

This result is an improvement in both sensitivity and rigidity range, over previous measurements. This flight has shown that the complete AMS on the International Space Station will provide an improvement in sensitivity by many orders of magnitude over previous experiments in the search for anti-helium.

2.3 The AMS-02 detector

The AMS-02 detector (Figure 2.4) will be installed on board the International Space Station (ISS) in 2007 (NASA shuttle flight UF-4.1), where it will operate for at least 3 years, at an altitude of 430 km on a 51^0 orbit.

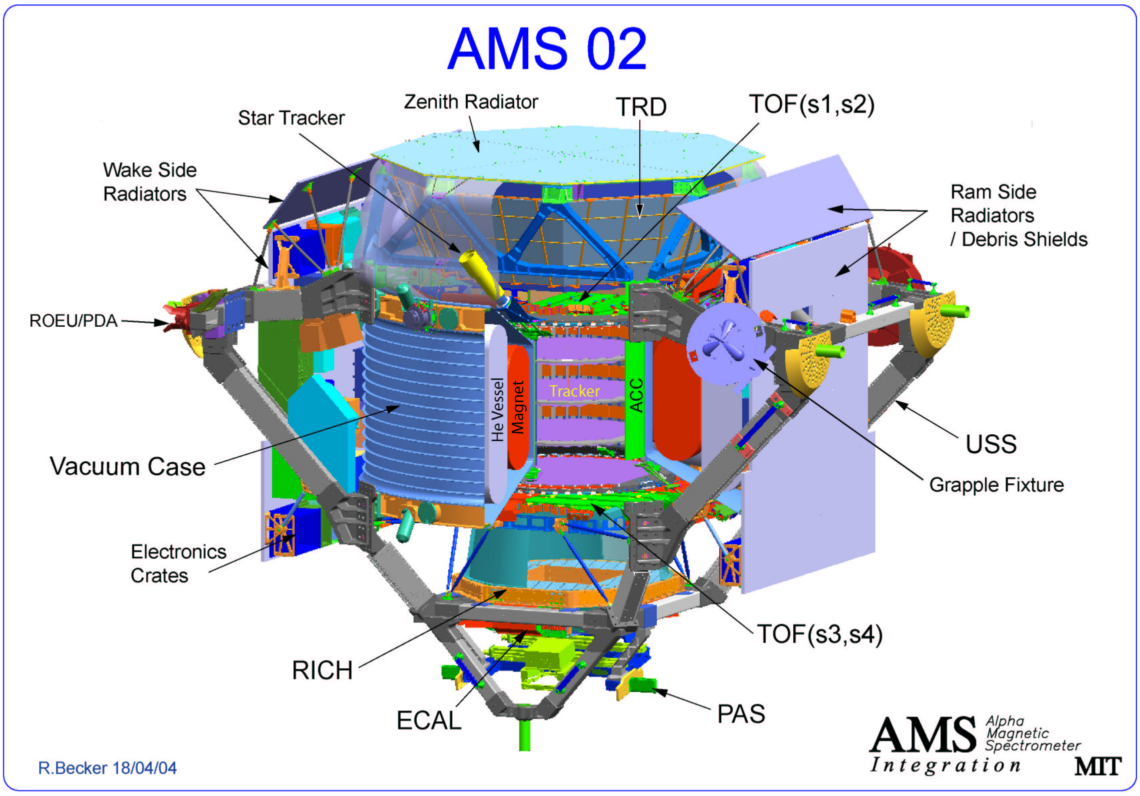

Figure 2.4: The AMS-02 detector.

The AMS-02 detector is based on a superconducting magnet generating a magnetic field stronger than the AMS-01 permanent magnet. The threshold Čherenkov counter will be replaced by a Ring Imaging Čherenkov (RICH) counter to increase the velocity and the charge resolution; two completely new detectors will be added: a Transition Radiation Detector (TRD), on the top of AMS-02, and an Electromagnetic Calorimeter (ECAL), below the RICH. They will improve the detector sensitivity to high energy electrons and photons, and the hadron/electron rejection capability.

The Magnet

AMS-02 will operate with a six times stronger magnetic field (compared with AMS-01) created by a superconducting magnet system. The AMS collaboration has chosen to use a superconducting magnet system, as it is the only way to generate the required magnetic flux density within the mass and the power constraints of the Space Shuttle during the launch and of the ISS during operation. The AMS-02 magnet will be the first large superconducting magnet to be used in space.

The magnet system of AMS-02 consists of a pair of large racetrack shaped coils together with two series of six smaller racetrack coils circumferentially distributed between them (see Figure 2.5 on left). The two main racetrack coils are akin to an Helmoltz pair; they are used to generate the main part of the transverse magnetic field. The twelve smaller racetracks are included to increase the magnitude of the overall dipole field; to reduce the magnitude of the stray field outside the magnet and to reduce the magnetic torque resulting from the interaction between the external field of the magnet system and the Earth's field.

The nominal bending power of the magnet system in this configuration is $BL^2 = 0.78\ Tm^2$ [33] (it was $0.14\ Tm^2$ for AMS-01).

All coils are located inside a vacuum tank and operate at $1.8^0\ K$ using super-fluid Helium. The free bore of the system has a diameter of $1.1\ m$, while the external diameter of the vacuum tank is $2.7\ m$, with a height of $1.55\ m$.

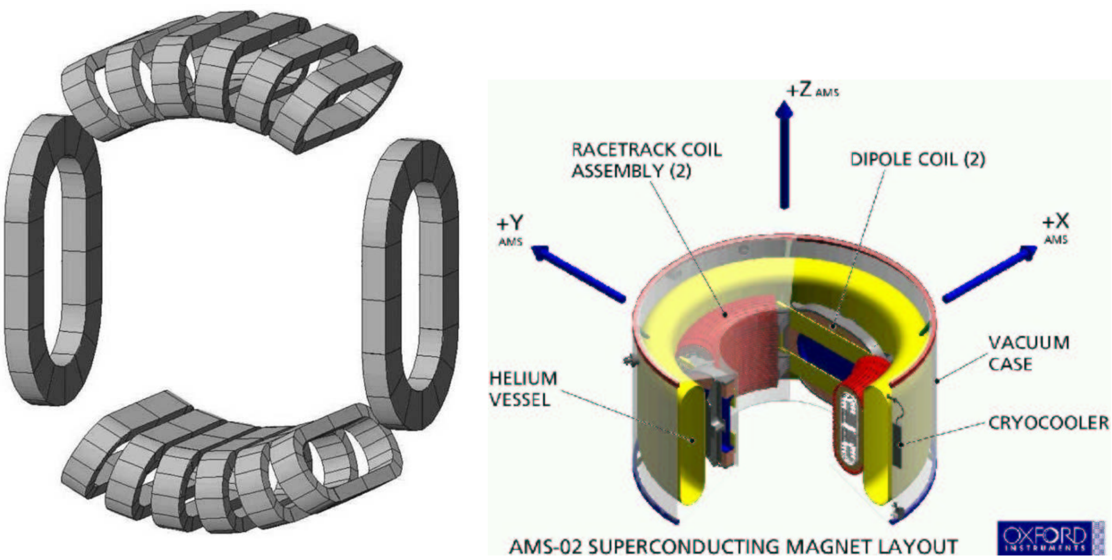

Figure 2.5: The AMS-02 superconducting magnet system.

The coils are electrically connected in series, and operate with a current of $459A$ in the "*persistent mode*": once a constant current has been established, a superconducting switch will cut off the power supply and the current will circulate with zero energy dissipation. At this stage no power is required to maintain the current loop. All magnets are wound from the same kind of conductor: a $NbTi/Cu$ superconducting wire embedded in a high purity aluminum stabilizer. A total of 55 km of strand is required for the whole system. The operating temperature is below 10^0 K, requiring 2500 liters of liquid Helium for the cooling (the He vessel is filled with super-fluid He at 1.8^0 K before the launch). The coils are thermally connected to the tank through pipes filled with pressurized super-fluid He. This material has the highest heat conductivity among all materials, and high density. Helium will circulate also in the cooling circuit, and finally will be vented into space. The large volume of 2500 liters is needed to be able to operate for three years without refilling.

The Tracking system

The main differences between the AMS-01 and AMS-02 tracker are the number of support planes (6 and 5 respectively) and read-out planes (6 and 8 respectively), the geometrical acceptance (from about 0.15 to 0.36 m^2sr), and the use of silicon detectors.

Decreasing the number of supporting planes results in a smaller amount of matter to be traversed by the particles, thus reducing the probability that multiple scattering affects the trajectory. This is the main source of loss of precision in momentum measurements at low rigidities.

The increment of the number of read-out (x, y) planes is obtained equipping both sides of the three internal planes with ladders; this guarantees a better measurement of the particle energy loss and an improvement in the reconstruction of the trajectory. In addition to a refinement in the ladders production and to the stronger magnetic field, the net result is a better measurement of the particle momentum.

An estimate of the AMS-02 proton rigidity resolution (≥ 5 hit tracks) is presented in Figure 2.6 [34]. Position resolutions of 30 (10) μm where used for the x (y) coordinates with a detection efficiency of 90% in the silicon detectors. The estimated resolution is about 1.5% for $5 \div 10$ GeV protons, and the MDR is in the range $1 \div 2$ TV.

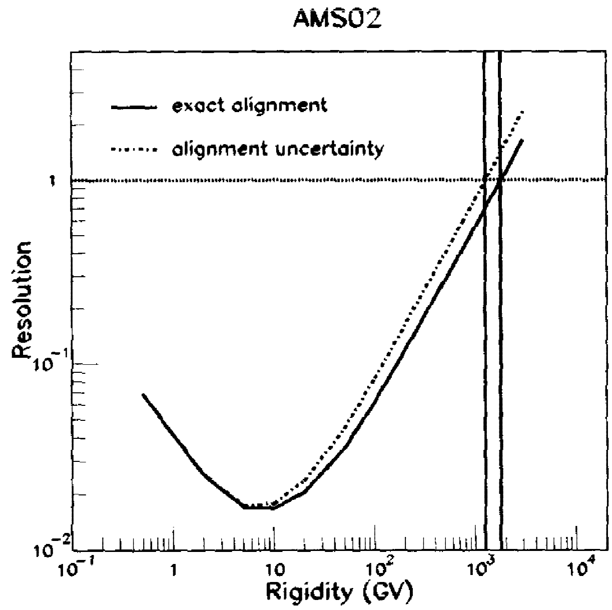

Figure 2.6: Rigidity resolution for the AMS-02 Tracker and 0.8 T superconducting magnet; the vertical lines denote the MDR.

The Time Of Flight system

The time of flight system of AMS-02 will be similar to the TOF system of AMS-01, but, due to the strong residual magnetic field in the phototube zone, the new TOF will adopt different PMTs (Hamamatsu R5946) and will have curved light guides in order to minimize the angle between the field and the PMT axis. This will produce a worse time resolution than AMS-01 ($\simeq$ 140 ps for protons, and better for other CR nuclei [35]). However the new front-end electronics will improve the charge resolution and the trigger efficiency will be unaffected by such problems.

The TOF system has the following essential tasks:

· has to send the start signals to the trigger system (see Section 2.4;

· the particle time of flight is used to measure its velocity $\beta = v/c$ when the crossing positions are known;

· the time of flight is used to distinguish between upward and downward going particles;

· has to give an independent charge measurement.

The Anti-Coincidence system

The Anti-Coincidence Counter (ACC) system forms a barrel around the silicon tracker of AMS-02. Its purpose is to flag events produced by particles crossing the detector from its sides, by δ-rays or even showers produced by triggered particles, and by back-scattering of the electromagnetic calorimeter. In these cases, the detector would record informations resulting in bad track fit, charge and velocity resolution.

The ACC modules are plastic scintillators (Bicron BSC414); the 16 paddles have a height of 83.2 cm and form a cylinder with an inner diameter of 109.1 cm. Their thickness is 1 cm and their signal is read by 16 PMTs at both ends. The power system and the read-out electronics are very similar for the TOF and the ACC phototubes. The ACC anodes will be sent to the scintillator front-end anti-coincidence board, that will send the discriminated signal to the trigger electronics. Since the ACC signals will also be used to check for back-scattering from the calorimeter, they will be used at the first level trigger stage in conjunction with the signals coming from the TOF and the ECAL system, as described in Section 2.4.

The Transition Radiation Detector

The Transition Radiation Detector (TRD) is a gas detector that measures the energy deposited by the X-rays produced by high energy charged particles crossing the radiator. When a charged particle crosses the boundary between two media with dielectric constants $\epsilon_1 \neq \epsilon_2$, it has a small probability ($\sim 10^{-2}$) of emitting transition radiation photons. Fleece material of type LRP-375 is used as radiator and the transition radiation photons are detected in straw tube chambers, working in the proportional regime, filled with a Xe/CO_2 (80/20) gas mixture.

The TRD has 20 layers, each with 21 mm fleece and modules of 16 tubes, 6 mm in diameter, assembled as a double layer of kapton-aluminum foil of 72 μm wall thickness. The upper and the lower four layers run parallel to the magnetic field, while the middle 12 layers are perpendicular, to provide 3D tracking.

Figure 2.7 shows measured single tube spectra with MIP signals from protons; additional transition radiation photon signals are clearly visible in the electron spectrum at energies above 6 KeV. Test beam results have shown that a 20 layer TRD small prototype, with fleece radiator and Xe/CO_2 straw tube detection, will provide proton rejection between 100 and 1000 for particle momenta up to 250 GeV [36].

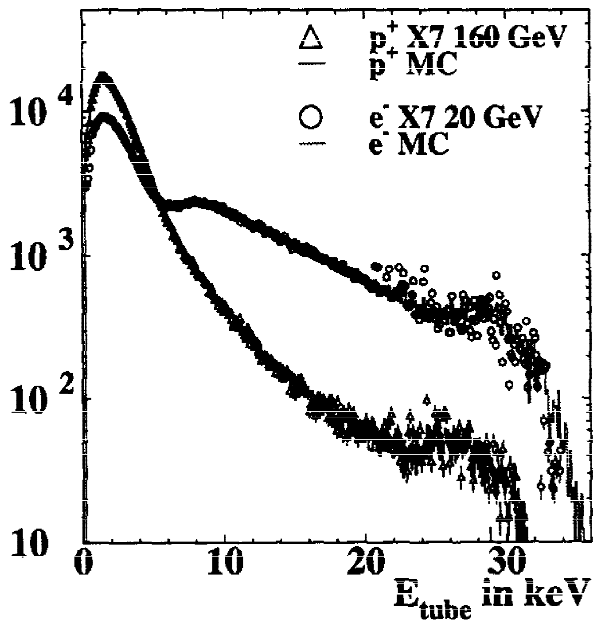

Figure 2.7: TRD test beam e^- and p tube spectra.

The Ring Imaging Čherenkov detector

The Ring Imaging ČHerenkov (RICH) counter is designed to provide the experiment with a precise measurement of the charged particle velocity, needed to perform isotope separation in a wide energy range. The RICH will also provide AMS with an extra electron-proton separation, needed to achieve the required rejection factor in positron and anti-proton identification. Moreover, the RICH will be able to supply AMS with an independent measurement of the particle electric charge up to Iron ($Z = 26$).

The detector main components are the Čherenkov radiator, the light detection system and the external conical reflector. Particles crossing the radiator layer with energy above the Čherenkov threshold will cause the emission of optical photons, eventually reaching the pixel plane (directly or after being reflected by the conical mirror) placed about half meter below the radiator. In the middle of the pixel plane there is a square hole in order to avoid having material in front of the electromagnetic calorimeter. The photon detection system consists of a set of 680 multi-anode PMTs Hamamatsu Inc. R7600-M16); the multi-anode structure (4×4 pads) together with the small PMT cross section (25×25 mm^2) provide the required accuracy in the photon position determination.

The overall reconstruction efficiency for events above the Čherenkov threshold ($2 \div 3$ GeV/n depending on the aerogel refraction index) is estimated to be greater than 70% for unit-charge particles and above 80% for $z > 1$ [37]. The reconstruction inefficiencies regard mainly uncontained events with a large fraction of the Čherenkov photons falling into the ECAL region of the detection plane. This sample could be partially recovered with the substitution of few aerogel tiles, in a central square, by another radiator with higher refraction index, e.g. NaF, so that the Čherenkov angles are big enough to avoid the central region. With the current configuration the RICH will provide AMS with a velocity resolution of about $\sim 0.1\%$ for protons.

2.4 The AMS-02 trigger

The *trigger* is the digital/analog signal which starts the data acquisition (DAQ) chain. By extension, this term is often used to represent the logic conditions required for it to be generated by the electronics.

In high energy physics experiments it is customary to define three types of trigger logics, depending on the type of data they act on: the *first level trigger* (including a pre-trigger called *fast trigger*) is generated imposing conditions on fast signals only (i.e. on logic signals coming from discriminators); the *second level trigger* is generated after the first level trigger if digitized data of any single subdetector satisfy the required conditions, and the *third level trigger* follows the second level trigger signal when the digitized data of the whole detector are checked against the desired set of conditions.

The general tasks of the AMS-02 trigger system are:

1) provide fast start signal for readout system in response to crossing of AMS-02 detector by particles of certain types with certain kinematic parameters (direction, momentum, velocity). The decision may be based on the analog signals from “fast” (PM-equipped) detectors like TOF, ECAL and ACC;

2) confirm or reset readout sequence based on more complicated analysis of the signals (analog or even digitized) from “fast” detectors and digital information from “slow” detectors (TRD and Tracker).

In AMS-02 two kind of triggers are performed: one for charged particles, and one for photons.

In the first case the validation (acquisition) of the event is done combining the response of different sub-detectors: TOF, ECAL and ACC. In this combination the TOF has to send to the trigger box the signals used to create the fast trigger signal: this is the very first step of the data acquisition electronics. This signal is used by the TOF electronics as the "time zero", which the scintillator time signals are referred to. The TOF system could also use the energy loss measurement to send to the trigger box a special flag for ions events, that can be used at *third level* to disable the anti-coincidence counters veto, that would suppress more strongly higher charges (whose flux is low).

While the one for photons is a stand-alone ECAL trigger. In fact the AMS-02 calorimeter has an excellent imaging capability (as will see later) which allows to implement a very efficient trigger for photons with energies down to few GeV and to reject most of the background (protons and electrons), increasing the total trigger rate only of few percents. The trigger is made up of two steps: a fast decision, available within 180 ns, given by the count of PMs above threshold in the central part of the ECAL; a *level 1* trigger decision, well before 1 μs, obtained with a fast reconstruction of the particle direction.

The ECAL stand-alone trigger is also able to provide an electron trigger that allows to recover the inefficiency introduced by the Anti-coincidence counters on high energy electrons with backsplash on calorimeter.

2.5 The AMS-02 prospect

1) Helium – AntiHelium

AMS-01 during the 10 days precursor flight on the Shuttle, has pushed the limit on the $^4\overline{He}$ at a level of less than about one part in a million; AMS-02 will eventually reach a sensitivity a thousand times better: in three years on the ISS, AMS will collect approximately 2×10^9 Helium events up to 3 TV (Figure 2.8).

2) $\mathbf{protons, anti-protons, electrons, positrons}$

In three years on the ISS the estimated collected data include:

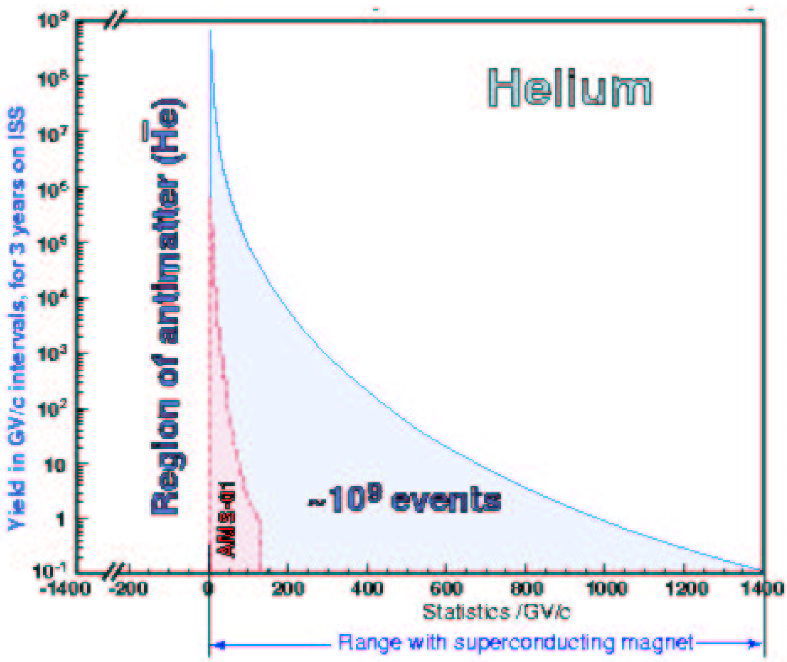

Figure 2.8: The expected Helium spectrum with AMS-02 after 3 years on the ISS compared to the AMS-01 measurement.

- ⋆ $\sim 10^6$ proton events above 1 TeV;
- ⋆ $\sim 10^6$ anti-proton events above 5 GeV;
- ⋆ $\sim 10^7$ electrons above 10 GeV up to 1.4 TeV;
- ⋆ $\sim 2 \times 10^6$ positrons above 5 GeV.

3) γ sources

EGRET [38] has detected more than 60 blazar AGNs with a mean redshift near $z = 1$ and more than 10 unidentified, likely blazar γ-rays sources. AMS will detect about one thousand such objects in three years [39].

4) isotopes

Regarding the stable light isotopes, AMS will be able to identify ^2H from ^1H and ^3He from ^4He up to $\simeq 10\ GeV/n$ and, after 3 years of data taking, AMS will collect $\sim 10^8$ ^2H and ^3He. Among all β-radioactive secondary nuclei in cosmic rays, ^{10}Be is the lightest isotope having a half-life comparable with the confinement time of cosmic rays in the galaxy. AMS will be able to separate ^{10}Be from the stable ^9Be [37].

These measurements can provide a detailed description of the cosmic ray propagation history for individual elements. Moreover, the ratio of selected unstable isotopes of the same origin is directly related to the cosmic ray confinement time in the galaxy.

Chapter 3

The electromagnetic calorimeter

The main goals of the experiment include dark matter search and cosmic ray physics in the energy range from few GeV up to 1 TeV. In particular AMS-02 will search for dark matter mainly in the e^+ and γ channels. An excess signal or a distortion of the energy spectra in these two channels might provide a signature for $\chi\chi$ annihilations.

The accurate measurement of the e^+ spectrum at energies greater than 10 GeV requires a high rejection power ($\sim 10^{-5}$) of a cosmic ray background mainly consisting of protons (Figure 3.1). This requirement can be achieved by means of a fine-grain sampling electromagnetic calorimeter able to image the shower development in 3D, thus allowing a discrimination between hadronic and electromagnetic cascades.

The calorimeter can be used as well to identify and measure the γ spectrum thanks to a very efficient stand-alone trigger.

In AMS-02 the design of such a detector has to take into account the peculiar characteristics of a space mission, imposing many constraints: the most restrictive ones concern weight (≤ 640 kg) and power consumption (≤ 100 W). Furthermore the calorimeter is required to operate in a residual magnetic field generated by the AMS-02 superconductive magnet with an intensity up to 200 $Gauss$.

3.1 The calorimeter structure

The electromagnetic calorimeter (**ECAL**) is a sampling device with a lead - scintillating fibers structure. The calorimeter is designed as a square parallelepiped with 65.8 cm side and 16.5 cm thickness. It is subdivided into 9 superlayers along

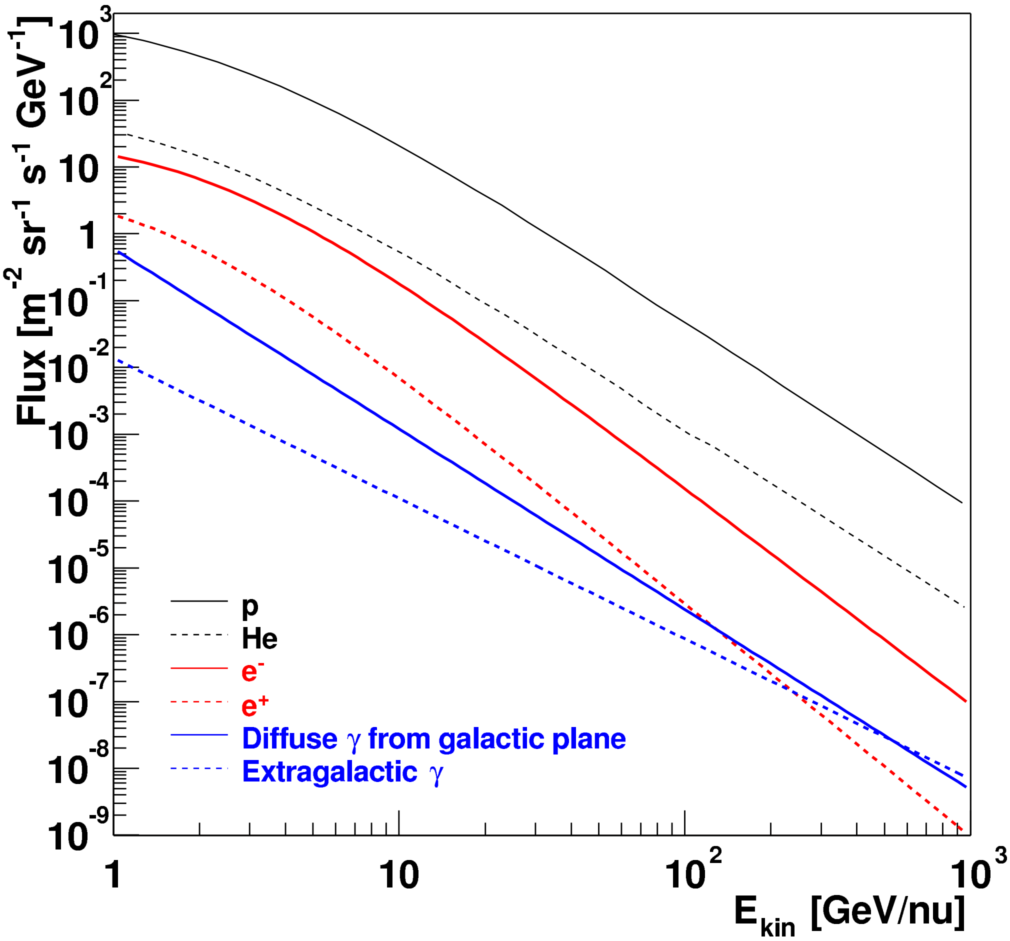

Figure 3.1: Cosmic rays spectra in the kinetic energy range $1 - 1000\ GeV$. The proton and Helium spectra are taken from AMS-01 measurements at polar latitudes. The spectra over the rigidity range $10 - 200\ GV$ are fitted respectively by a power law $E^{-2.78}$ (protons) and $E^{-2.74}$ (Helium nuclei). The points above $200\ GV$ rigidity are calculated by extrapolation of these power law spectra. The e^+ and e^- spectra are theoretical interstellar spectra [40]: no separate e^+ and e^- flux measurements above $100\ GeV$ have been performed so far. The extragalactic γ-ray emission and the diffuse γ-ray emission from the galactic plane were first measured by EGRET; the points above a few tens of GeV are extrapolated from the power law fits (respectively $E^{-2.1}$ and $E^{-2.7}$) of the experimental spectra.

its depth. Each superlayer, 18.5 mm thick, consists of 11 grooved lead foils, 1 mm thick, interleaved with layers of 1 mm diameter scintillating fibers glued by means of an epoxy resin. The resulting composite structure (Figure 3.2) has a lead-fiber-glue volume composition of 1 : 0.57 : 0.15 cm^3 and an average density of 6.8 ± 0.3 g/cm^3. According to these values, the calorimeter has a total weight of approximately 498 kg

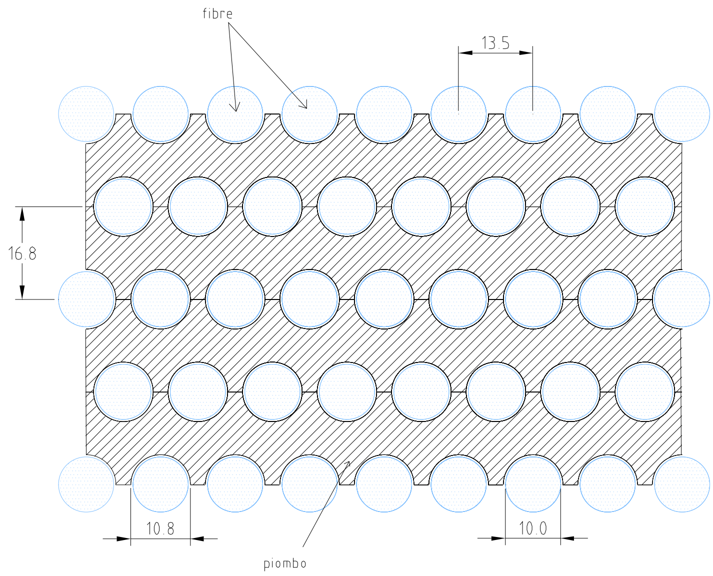

Figure 3.2: ECAL lead and scintillating fibers structure.

and a radiation length of about 10 mm, so that the total calorimeter thickness corresponds to about 17 radiation lengths.

Within each superlayer, fibers run along a single direction; the detector capability for 3D shower reconstruction is obtained by alternating superlayers having fibers along the X axis with superlayers having fibers along the Y axis (Figure 3.3). The calorimeter has 4 superlayers in the X view and 5 in the Y view (bending plane of the spectrometer magnetic field).

In order to improve the e^+/p rejection power, the detector is characterized by high granularity: each square element (with 9 mm side) covers an area of about 35 fibers and corresponds to half a Molière radius in transverse dimension and one radiation length in depth. Each superlayer can be seen as built up by two 9 mm thick layers. As a result (Figure 3.4) the calorimeter has a total of 1296 read-out elements (cells) allowing for 18 samplings in depth (10 in the Y and 8 in the X

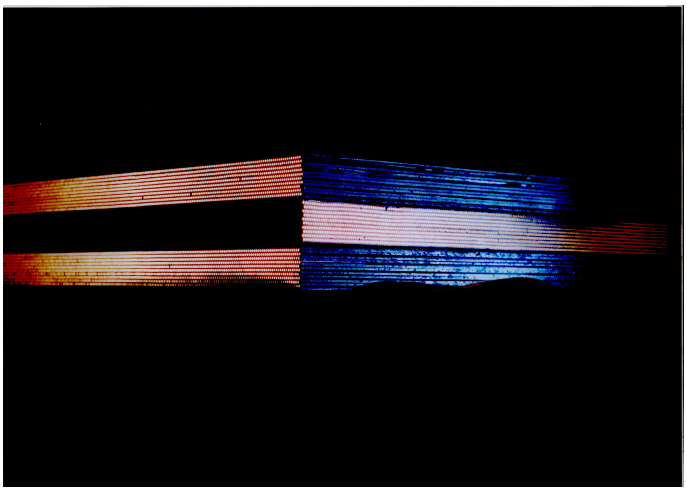

Figure 3.3: Assembling of three superlayers.

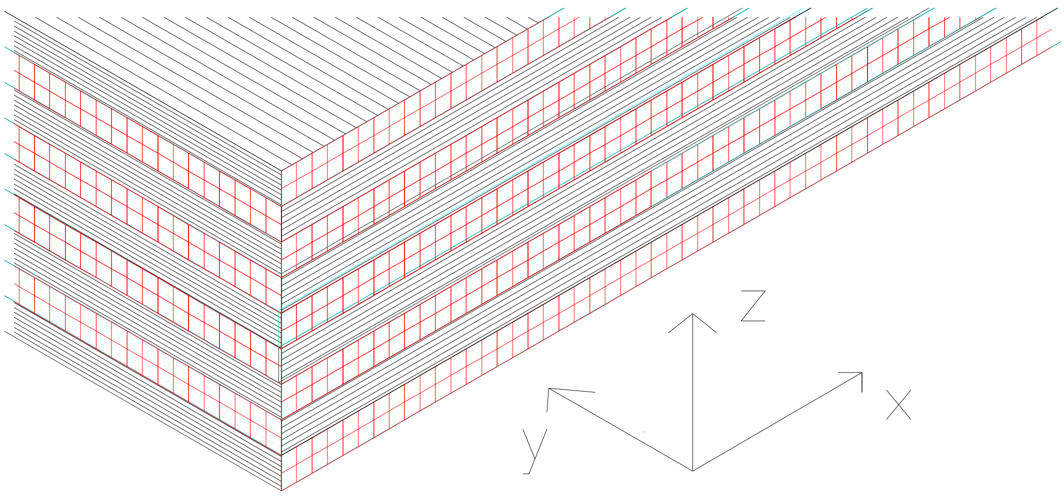

Figure 3.4: ECAL 3D view. All nine superlayers (5 along Y and 4 along X) are shown. The red squares represent the read-out cells; four adjacent cells are read by a single PM.

view).

3.1.1 The mechanical assembly

The mechanical assembly of the calorimeter is show in Figure 3.5 and is designed to fulfill four main requirements:

- minimum weight;
- first resonance frequency above 50 Hz;
- capability to face accelerations up to 14 g in any direction;
- capability to maintain the detector temperature within a ±5℃ interval, while the outside temperature ranging from −40℃, up to 50℃, with a periodicity of about 90 minutes.

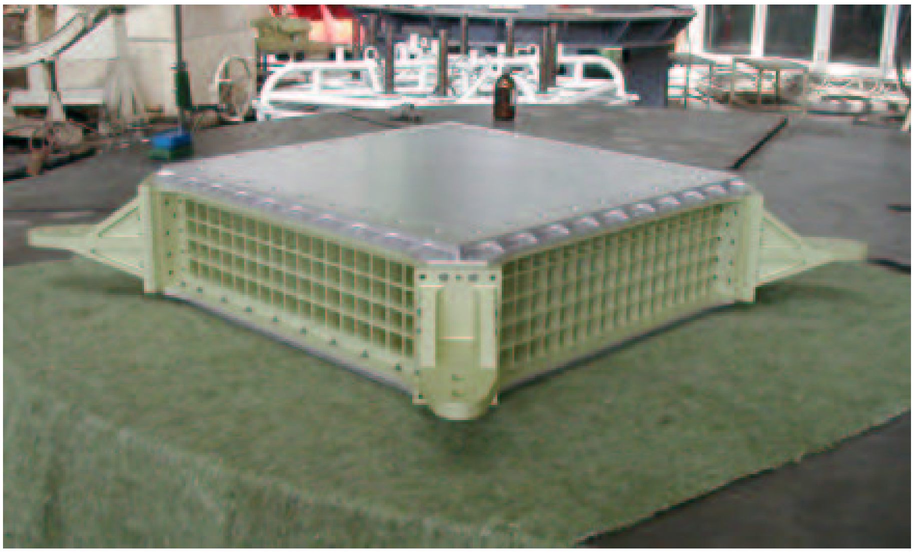

Figure 3.5: The ECAL mechanical support structure.

The optimization of the mechanical project through Finite Element Analysis studies led to an Aluminum alloy support frame, composed of four lateral panels lodging the light collection system and two (top and bottom) honeycomb plates.

According to the present configuration the detector total weight is 637 kg.

The structure has a first resonance frequency at 89 Hz for $X - Y$ vibrations and 62 Hz for Z vibrations as measured during the tests performed both at Beijing (January 2003) and at Terni (November 2003).

During the Space Qualifying verification in Beijing, three different tests were performed:

1) Random vibration test; at the maximum expected flight level.

2) Sine-Burst test; at frequency of 17 Hz and test level equal to 12 g. This test is equivalent to a centrifugal one.

3) Sine-Sweep test; in the range $20 \div 300$ Hz, at level equal to 0.25 g.

The SQ test was successful: the ECAL structure has enough strength and passed the verification with no damage.

The sine sweep test was repeated at Terni where the ECAL was equipped with some photomultipliers. At the end, no damage occur to the light collecting system, the PMs and the electronics boards.

3.1.2 The light collection system

The light signal from fibers is read-out on one end only by four-channel multi-anode Hamamatsu photomultipliers (R7600-00-M4). These devices have an active area of 9×9 mm^2 for each anode (pixel). Each superlayer is read by 36 PMs alternatively arranged on the two opposite sides in order not to create mechanical interference.

To maximize light yield and reduce cross-talk between pixels, photons from fibers are collected by means of Plexiglas light guides, shaped as a truncated pyramid and inserted inside a polycarbonate support tube. Two transparent Silicon joints positioned on both ends of each light guide ensure good optical contact between fibers and PMs even when high mechanical stresses are applied.

The residual magnetic field ($\simeq 200$ $Gauss$) of the AMS-02 superconductive magnet imposes the use of a magnetic shield able to keep the field intensity below 20 $Gauss$. The weight limitation and the small space available between photomultipliers makes it necessary to optimize the thickness of the material used for magnetic shielding. According to both Finite Element simulations and measurements taking into account also the final PMs reciprocal position, the best shielding resulted to be 1 mm thick soft Iron tubes shaped as square parallelepipeds, having a size of 30.5 mm and a length of 100 mm. It has been verified that the response of the photomultiplier is affected by less than 10% by such a field [41].

3.1.3 Photomultiplier bases and front-end electronics

Several tests with different divider ratios led to the choice of a particular tapered bleeder able to reduce the photomultiplier power consumption down to 100 mW (at the standard working point of 650 V) but preserving the response linearity over a very wide dynamic range: at a gain of 10^5, the PMs are able to detect signals up to the maximum energy deposition by 1 TeV electrons in one cell ($\sim$ 55000 photo-electrons, according to Monte Carlo simulation) with a deviation from linearity of about $\sim$ 20% [42] (see Fig. 3.6). The PM base is assembled in a polycarbonate supporting tube: each divider consists of two electronics cards with $2.6 \times 2.6\ mm^2$ cross-section, both embedded in a potting to avoid sparks at low air pressure.

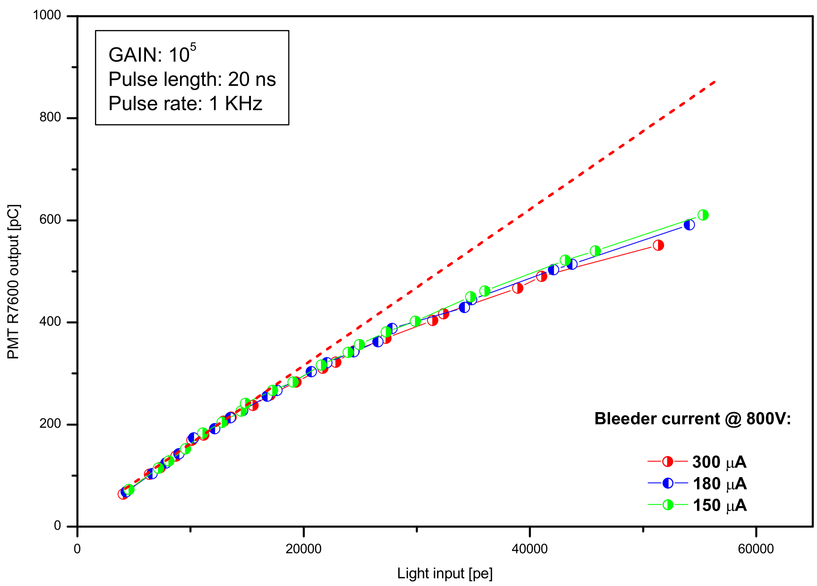

Figure 3.6: The PM linearity plot. The three curves represent measurements made by means of bleeders with different current, but with the same HV distribution ratio.

Behind the PM base is mounted the front-end card containing the "Sample and Hold" electronics and the digitization system.

The energy released by one *Minimum-Ionizing Particles* (*MIP*) traversing a cell corresponds to about 8 photo-electrons, so that the maximum energy released in a single cell by a 1 TeV shower is approximately equivalent to 7000 $MIPs$. Choosing to set a MIP signal equivalent to 5 LSBs (Least Significant Bit) of the ADC, the corresponding dynamic range of $3.4 \cdot 10^4$ requires a 16 bits ADC. In order to use "standard" 12 bit ADCs, digitization is performed at two different gains. Such a scheme was implemented by means of a dedicated ASIC chip operating over the required dynamic range (see Fig. 3.7) and with a very low power consumption (21 mW).

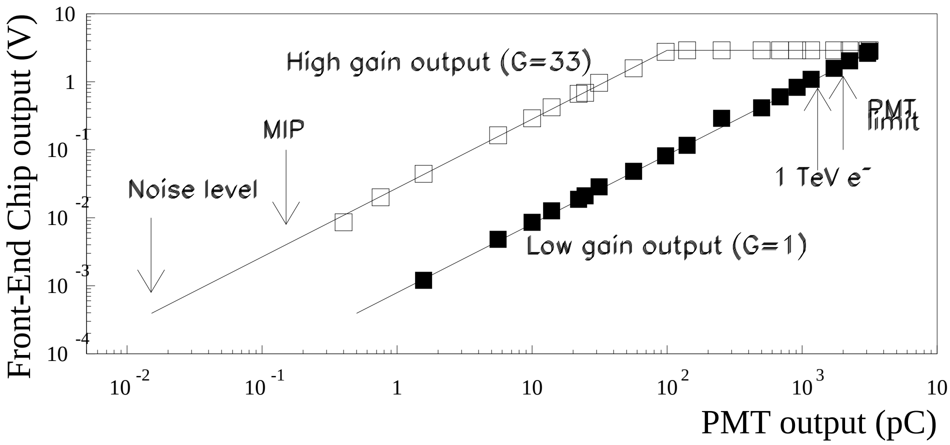

Figure 3.7: The dynamic range of front-end chip. The maximum expected PM signal is around 1000 pC.

Besides the 8 signals coming from the PM anodes, the front-end chip provides also the last dynode signal: this signal will be used to build up the ECAL stand alone trigger.

3.2 The electromagnetic shower

The dominant energy loss mechanism of high-energy electrons in matter is bremsstrahlung, while for high-energy photons it is e^+e^- pair production. Above approximately 1 GeV the cross-sections of these processes become energy independent. A high-energy electron or photon impinging on a thick absorber, produces an iterative sequence resulting in a cascade of electrons, positrons and photons with lower energy. Electron energies eventually fall below the critical energy at which point electrons start dissipating their energy by ionization and excitation rather than by the generation of more shower particles.

The *critical energy* E_C is defined as the energy at which rate of energy loss by bremsstrahlung equals that by ionization. A widely used parameterization for the critical energy is:

$$E_C = \frac{800\ MeV}{Z + 1.2}$$

where Z is the atomic number of the material. For Lead $Z = 82$; therefore the critical energy in the ECAL is:

$$E_C \simeq 9.6\ MeV.$$

The longitudinal development of the shower is governed by the high-energy part of the cascade, and thus it scales as the radiation length in the material.

The *radiation length* X_0, usually measured in cm, is the mean distance over which a high-energy electron loses all but $1/e$ of its energy by bremsstrahlung. The e-folding distance for pair production by a photon is $\frac{7}{9}X_0$.

The ECAL radiation length depends on the volume ratios for the different materials [1]:

$$\frac{1}{X_0} = \frac{1}{X_{0Pb}}\frac{V_{Pb}}{V} + \frac{1}{X_{0sci}}\frac{V_{sci}}{V}$$

(X_{0Pb}= 0.56 cm, X_{0sci}= 42.4 cm) the lead-fiber-glue volume composition is 1:0.57:0.15 cm^3, hence the design value of the ECAL radiation length is:

$$X_0 \simeq 0.96\ cm.$$

In describing the shower behavior it is convenient to introduce the scale variable $t = x/X_0$ so that distances are measured in units of the radiation length.

The mean longitudinal profile of the energy deposition of an electromagnetic cascade is reasonably well described by the *Gamma* distribution:

$$\frac{dE}{dt} = E_0 \frac{b^{(\alpha+1)}}{\Gamma(\alpha+1)} t^{\alpha} e^{-bt} \tag{3.1}$$

where E_0 is the energy of the incident electron or photon, and $b \sim 0.5$ with a weak dependence on Z.

The maximum t_{max} occurs at α/b and it can be expressed as a function of E_0 as:

$$t_{max} = \frac{\alpha}{b} = ln\left(\frac{E_0}{E_C}\right) + C_j \qquad\qquad j = e, \gamma \tag{3.2}$$

where $C_e = -0.5$ for an electron-induced shower and $C_\gamma = +0.5$ for a photon-induced shower.

Energy	t_{max}	plane number where the shower maximum is
10 GeV	6.4	$6 \div 7$
20 GeV	7.1	$7 \div 8$
100 GeV	8.7	9
500 GeV	10.4	$10 \div 11$
1 TeV	11.0	$11 \div 12$

Table 3.1: Position of the shower maximum in the calorimeter for different electron incident energies.

From Equation 3.2 it is possible to estimate the plane number where the shower maximum is, for different incident electron energies; as shown in Table 3.1, the maxima are well contained in the calorimeter at least for $\lesssim 1\ TeV$ electrons. This implies that it is possible to reconstruct the particle energy, even if the shower is not fully contained in the calorimeter, up to an incident energy of $\sim 1\ TeV$.

For a completely contained shower the following parametrization for the shower length (at 98% longitudinal containment) can be used:

$$L(98\%) \simeq t_{max} + 4\lambda_{att} \tag{3.3}$$

where λ_{att} is the exponential attenuation length for the second part of the shower (i.e., the parameter $1/b$ in longitudinal development 3.1). The attenuation length λ_{att} is a calorimeter feature and it does not depend on the particle energy:

$$\lambda_{att} \sim (2.3 \pm 0.3) \cdot X_0.$$

We have already seen that for the ECAL $X_0 \simeq 0.96\ cm$, thus $\lambda_{att} \sim (2.2 \pm 0.3)\ cm$. In Table 3.1 is shown how the shower maximum for a 10 GeV electron is between plane number 6 and 7. From Equation 3.3 it follows that cascades of energy $\lesssim 10\ GeV$ are contained in the calorimeter, with a leakage of a few percent. As we shall see in following, a full longitudinal shower containment is not necessary to reconstruct the electron energy.

[1] The contribution from glue is considered together with the scintillating material

The transverse development of the electromagnetic showers in different materials scales fairly accurately with the *Molière radius* R_M, given by:

$$R_M \simeq X_0 \frac{21\ MeV}{E_C\ [MeV]}$$

where, for ECAL, $E_C \simeq 9.6\ MeV$, so that $R_M \simeq 2\ cm$. On average, only 10% of the energy lies outside a cylinder with radius R_M.

The resolution of sampling calorimeters is usually dominated by sampling fluctuations, leading to a fractional resolution $\sigma(E)/E$ scaling as the inverse square root of the incident energy. At high energies deviations from $1/\sqrt{E}$ occur because of noise, non-uniformities, calibration errors and incomplete shower containment. Such effects are usually included by adding a constant term to $\sigma(E)/E$:

$$\frac{\sigma(E)}{E} = \frac{\sigma_{sampl}(E_C, X_0, s)}{\sqrt{E}} \oplus \sigma_{const}$$

where s is the active material thickness.

3.3 The hadronic/electromagnetic discrimination

The hadronic showering process is dominated by a succession of inelastic hadronic interactions. At high energy, these are characterized by multi-particle production and particle emission originating from nuclear decay of excited nuclei. Due to the relatively frequent generation of π^0, there is also an electromagnetic component present in hadronic showers. Secondaries are mostly pions and nucleons. The hadronic multiplication process is expressed in terms of the *nuclear interaction length* λ_I [2], which is essentially energy-independent (for Lead: $\lambda_I = 17.1\ cm$).

To maximize the discrimination between hadronic and electromagnetic showers in the calorimeter, the critical quantity to maximize is the ratio λ_I/X_0, which is approximately proportional to $Z^{1.3}$; this allows to contain electromagnetic showers over a short distance, without initiating too many hadronic showers. The ECAL, using Pb as passive absorber, is designed according to this rule; its total thickness is equivalent to 17 X_0 and about one λ_I. The probability of interaction for protons in ECAL is:

$$P = 1 - e^{-T/\lambda_I} \sim 60\%$$

[2]Defined as..

where T is the total thickness of the calorimeter.

One has 95% radial containment of an hadronic shower for $R_{95\%} \simeq \lambda_I$. Therefore a large ratio for λ_I / X_0, together with a fine granularity, also allows to discriminate between the lateral shape of the different cascades.

In Figure 3.8 is shown a typical electromagnetic shower generated by a 10 GeV electron impinging perpendicularly on the calorimeter. As expected, the shower begins in the first radiation lengths of the detector, depositing almost all of its energy in the calorimeter with a narrow lateral spread. Figure 3.9 shows a Minimum Ionizing proton (MIP) (*top*) and an hadronic cascade (*bottom*). Hadrons tend to interact in the rear part of the calorimeter and their cascades have a wide lateral spread, while a non-interacting proton is recognized as a straight line pattern with an energy deposition compatible with the ionization loss rate dE/dx given by the Bethe-Block formula.

The good e/h discrimination capability of the AMS-02 calorimeter also derives from its imaging capability. In fact, taking advantage of its fine granularity and geometry with alternate planes of fibers oriented along mutually orthogonal directions, the calorimeter can image the longitudinal and lateral development of electromagnetic and hadronic showers, providing two orthogonal views for each event (see Figures 3.8 and 3.9).

If an hadronic shower were completely contained in the calorimeter, the visible energy deposited in the calorimeter would be smaller than that measured for an incident electron of the same energy. This is due to the fact that only a small fraction of the hadronic energy converted into nuclear excitation and break-up appears as detectable signal. Moreover there are large event-to-event fluctuations. In addition, highly penetrating particles like μ or ν from π decay escape the calorimeter carrying away energy. Therefore it is also possible to discriminate hadronic from electromagnetic showers comparing the ratio between the energy measured in ECAL and the particle momentum measured from the tracking system.

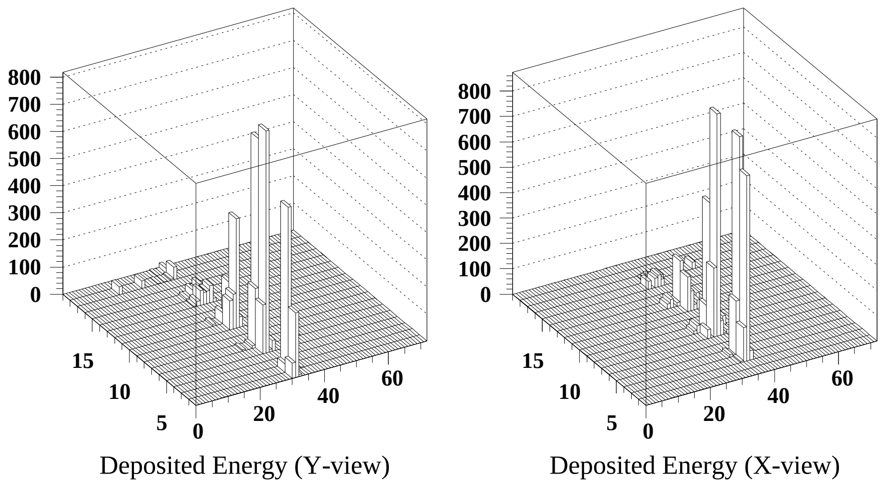

Figure 3.8: Typical electromagnetic shower generated by a 10 GeV electron (energy depositions are in MeV).

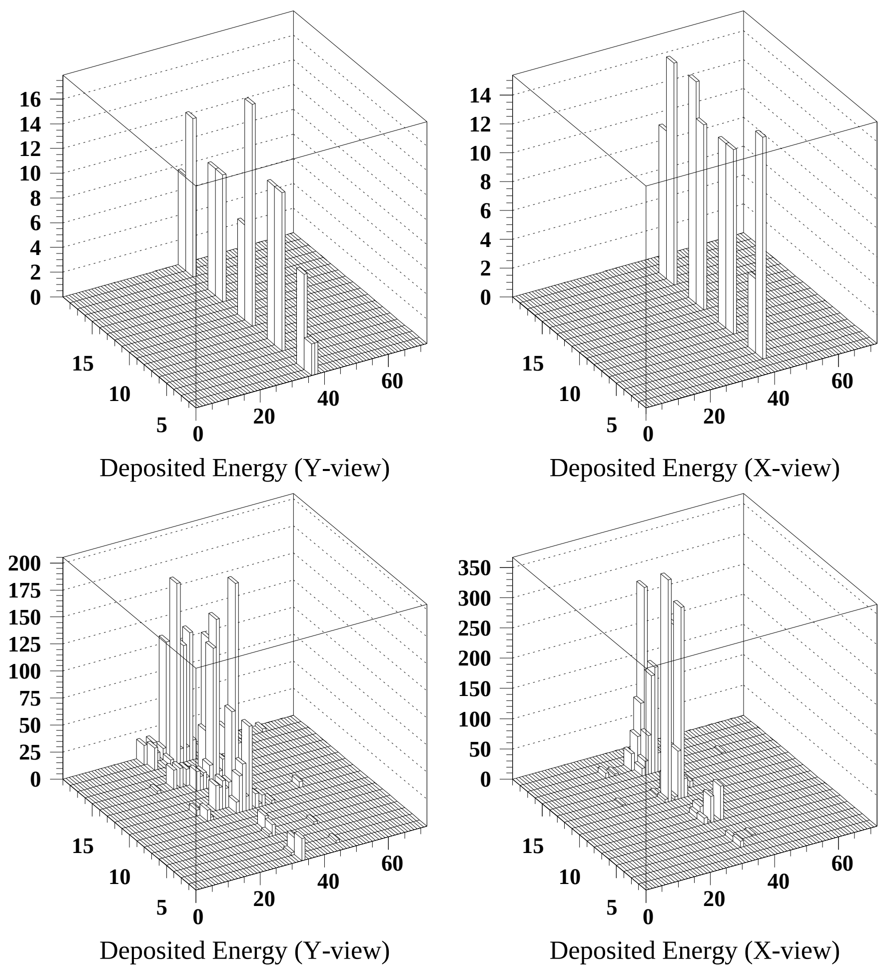

Figure 3.9: Energy deposited (MeV) by 10 GeV protons. *Top*: a Minimum Ionizing proton (MIP). *Bottom*: a hadronic cascade.

Chapter 4

Analysis of ECAL Test Beam data

4.1 Description of Test Beam set-up

In July 2002 a full-scale prototype of the AMS02 electromagnetic calorimeter was tested at CERN SPS the H6 beam line using beams of muons, protons and anti-protons at 120 GeV and electrons with energy ranging from 3 to 180 GeV. The calorimeter was only partially equipped with photomultipliers: 63 were used instead of the 324 foreseen in the final configuration. This corresponds to 7 PMTs per layer, i.e. a corner with an effective active area of 126×126 mm^2 was completely equipped. A scheme of the geometrical arrangement is shown in Figure 4.1. The PMTs high voltage was adjusted to fix the gain at a value around 2×10^5.

The optical coupling between fibers and PMTs was realized in air, through truncated pyramid polycarbonate supports covered with a special high reflectivity Aluminum foil. Fibers are only read only at one end; during the Test Beam.

Beam particles were triggered by means of a 3-fold coincidence of scintillators aligned along the beam line. Two Čherenkov detectors were operational as part of the beam instrumentation: a CEDAR (Čherenkov Differential counter with Achromatic Ring focus) was used with proton beams to reject the contamination of pions, kaons and electrons; while a threshold counter was used to tag low energy electrons ($\lesssim$20 GeV).

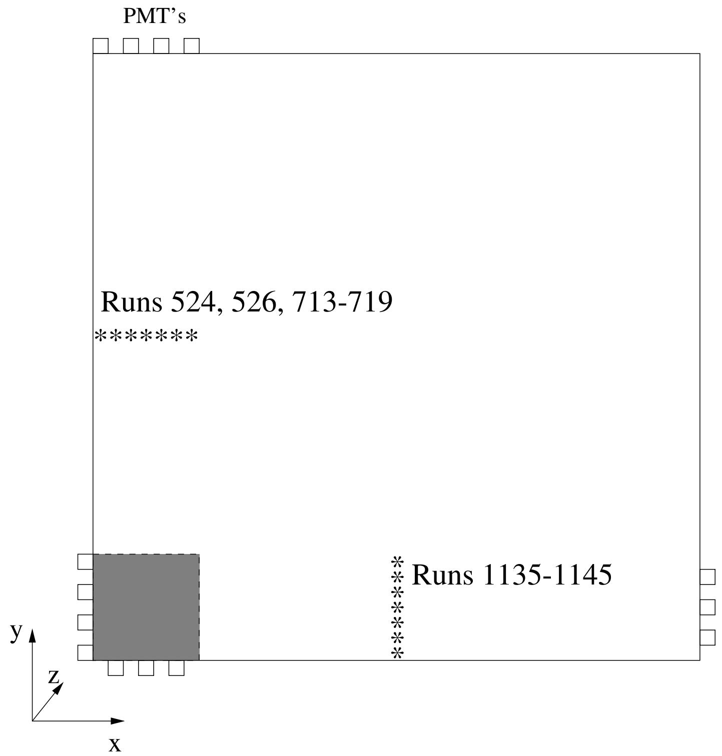

Figure 4.1: Scheme of the test beam set-up; the beam direction is along the z axis. The asterisks show the beam impact points for the runs used for the PMs equalization with MIPs.

4.2 Preliminary analysis

4.2.1 The Attenuation Length

Electrons of 120 GeV were used to determine the signal attenuation along the fibers of the ECAL. Using electrons a size-able signal can be extracted with the low gain, thus the potential uncertainty linked with the change of relative gain of the high gain signals is avoided; nevertheless, due to the lateral development of the electromagnetic shower, together with the lateral spread of the beam, particles with impact points very close to the edge of the calorimeter cannot be used.

To measure the attenuation length, the position of the beam impact point for each run is needed, thus the coordinates used are extracted from the database. Data were selected by choosing set of runs taken at the same X (resp. Y), so the signal was read by the same PM.

The amplitude of the signal was extracted by fitting a gaussian on top of an exponentially falling background.

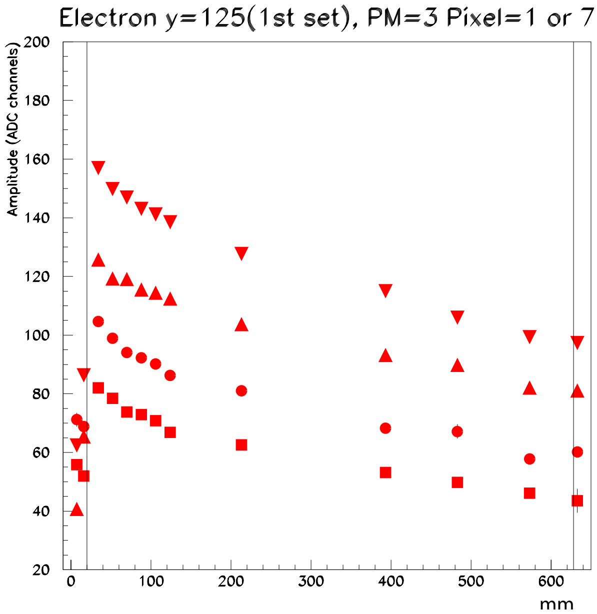

Figure 4.2: Sets of data points from the electron runs, which were used in the global fit of the attenuation length. Each of them represents an individual pixel.

Once the amplitude of the signal at each position is known, the attenuation as a function of the distance of the impact point from the PM can be obtained. Figure 4.2 displays the amplitude of the signal as a function of the distance from the PM, for the different sets of runs considered and for several PMs in depth.

Light undergoes an approximately exponential attenuation along each fiber. More precisely, one observes the combined effect of a fast attenuation, characterized by a short decay length, and a slow attenuation, having a typical decay length of $\sim 2 \div 3\ m$.

We have therefore fitted each set of points with the following function:

$$g(x) = A(0)\left(f \cdot e^{-\frac{x}{fast}} + (1-f) \cdot e^{-\frac{x}{slow}}\right)$$

where $A(0)$ is the amplitude of the signal without attenuation (i.e. measured when the beam is close to the PM) and f is the fraction of the fast-decaying component. $fast$ and $slow$ are the attenuation lengths respectively of the fast and the slow component.

From this analysis, assuming no reflection at the fiber aluminised end, an attenuation function common to all the ECAL cells was obtained [43]:

$$f \simeq 0.19 \qquad fast \simeq 130\ mm \qquad slow \simeq 2200\ mm.$$

4.2.2 The High/Low gain ratio

The dedicated ECAL front-end chip was designed to perform digitization at two different gains in order to operate over the required dynamic range (see Sect. 3.1.3). The high/low gain ratio can be measured by selecting cells having large energy deposit (i.e. the central cells of showers from electrons with energy $\geq 20\ GeV$) and plotting for each one the high vs. low gain output. The high/low gain ratio is given by the slope of this scatter plot in the linear region, before the high gain output starts saturating. Some unexpected effects emerge out from these studies; the first is that each cell shows two different slopes in the ratio plot. Moreover the two slopes are different from pixel to pixel. As shown in Figure 4.3, this behavior is common to all the different beam energies: the change in slope starts at the same value of the ADC counts (about 45 in the low gain output).

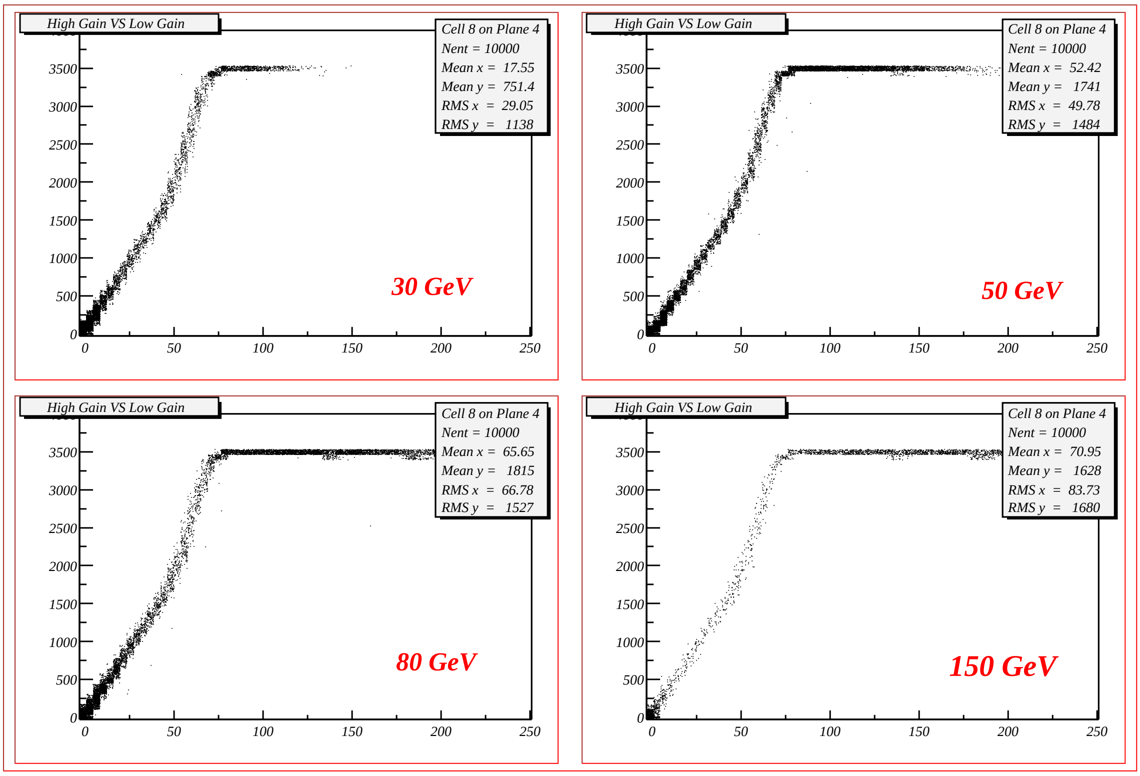

Figure 4.3: High gain vs. low gain output of the same cell for different beam energies.

To find the correction factors for the measured energy, a fit for each slope in the high/low gain ratio was performed; an example is shown in Figure 4.4 for cell number 6 in plane 3. The mean value of the initial slope, for all the ECAL cells, is about 36 (instead of the nominal 33); the dispersion due to the fit fluctuations is about 3% while the maximum dispersion among differernt cells is $\sim$ 15%; it is thus necessary to determine the value of the ratio for each cell. The mean value of the slope in the second part of the plots is about 70.

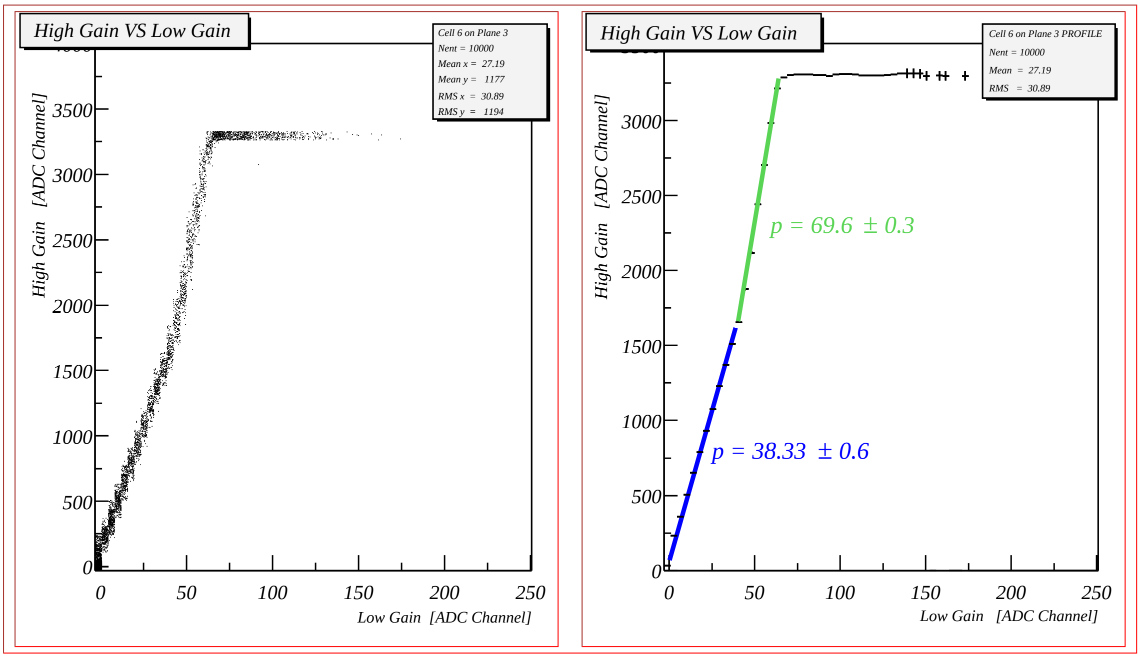

Figure 4.4: High gain output vs. low gain output in a cell; the two slopes are fitted separately.

The observed behavior may be attributed to a current limitation in the chip supply. As far as the present analysis is concerned, two correction factors were introduced for each cell, considering both slopes.

4.3 Photomultipliers equalization

The ECAL cells show different responses to the same input energy because of gain differences among PMs, of non-uniformity among the four pixels of each PM and of fluctuations in light collection; therefore an equalization has to be applied in the offline analysis.

Two different equalization procedures were performed: the first method is based on measurements of the individual response of each cell to MIPs, the second one requires a study of the ECAL response to electromagnetic showers.

4.3.1 Equalization with *MIP*s

Proton and pion beams of 120 GeV were used for the equalization procedure with MIPs. This was done by selecting events where the incident particle traversed the calorimeter with a minimum energy loss.

A complete scanning of the instrumented cells along both x and y was performed moving the beam on the ECAL surface. The x direction was scanned keeping the y position equal to half of the fiber length and in an analogous way for the scanning along y (as shown in Figure 4.1). In this way the light attenuation along the fibers is the same for PMs on opposite sides and the equalization procedure is decoupled from the light attenuation correction.

For each cell traversed by the MIP the energy distribution was plotted and fitted with a Landau function (see Figure 4.5). The most probable values of the Landau distributions obtained were used as coefficients to weigh each pixel signal.

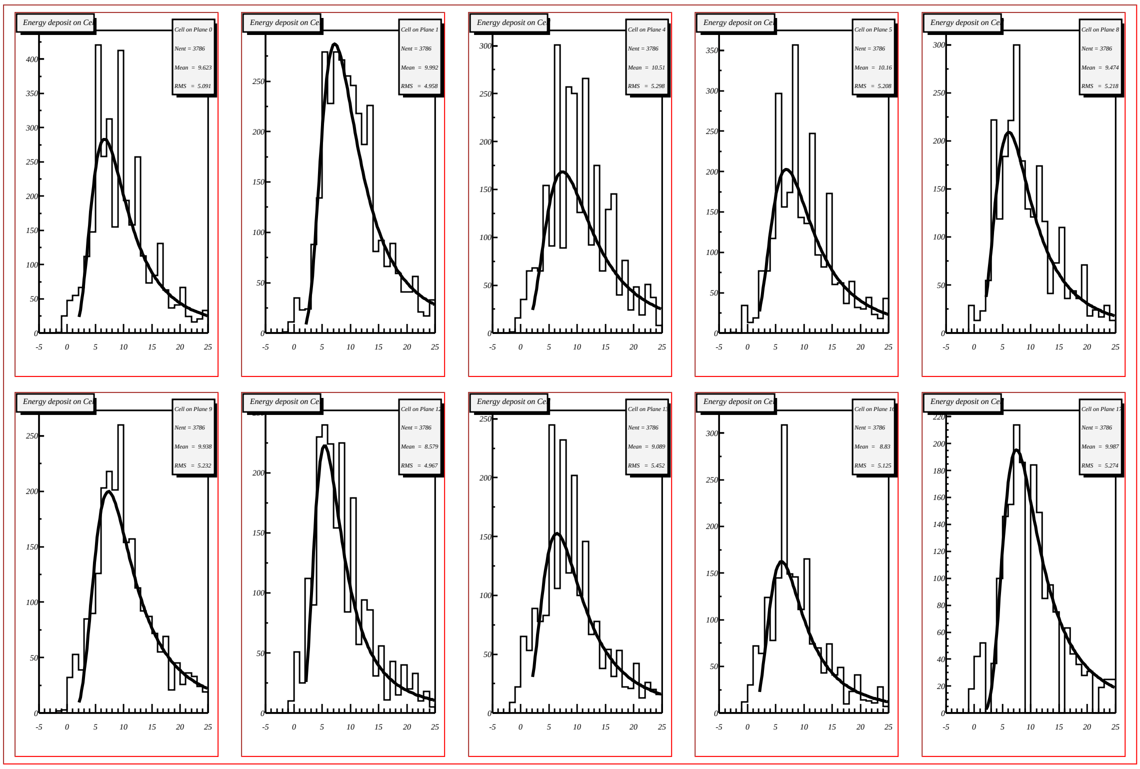

Figure 4.5: MIPs energy distributions in some cells in y view (once per plane). The distributions are fitted by a Landau function.

In Figure 4.6 is shown the distribution of the MIP peak signals measured in all the ECAL instrumented cells. The average MIP signal was:

$$MIP = (7.09 \pm 0.09)\ \ ADC\ counts\ /\ cell$$

where the charge seen by each cell is expressed in ADC counts.

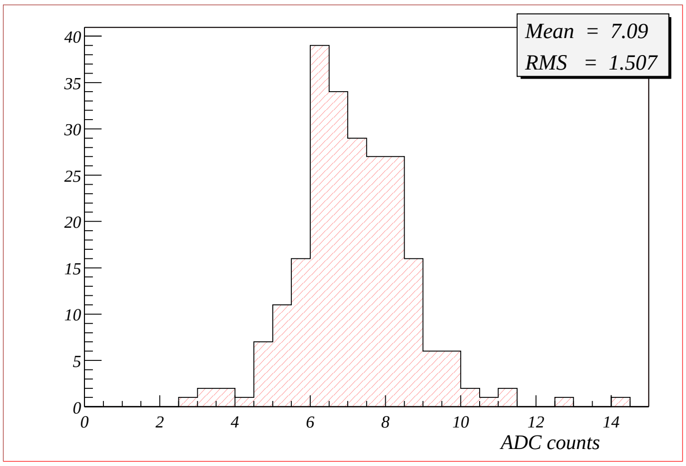

Figure 4.6: MIP peak signals measured in all the ECAL instrumented cells.

4.3.2 Equalization with electrons

This equalization procedure was first applied in the analysis of the ECAL test beam data taken in 2001 [44]. In fact, for this data sample the signal of a MIP for a single cell was too small to obtain a good determination of the energy deposition from the fit. The reasons behind this problem were solved before the ECAL test beam in 2002. Nevertheless this procedure provides better results and was therefore used again during the 2002 data analysis.

As far as the equalization procedure using electromagnetic showers is concerned, the equalization with MIPs and the correction due to the light attenuation along the fibers can be consider as a pre-equalization. Particularly, the light attenuation correction cannot be decoupled from this equalization procedure.

Equalization of cells within the same plane

The first step of this procedure consists in the equalization of the cells within the same plane. This method is based on the fact that for electrons impinging perpendicularly on the calorimeter, most of the energy deposit is contained within a narrow column in the z direction[1], as shown in Figure 4.7 for simulated electrons. This shows the energy deposit summed over the whole ECAL depth; the x axis is the distance in pixel units (1 cell = 0.925 cm) from the initial particle direction. This distribution can be compared with the lateral energy distribution obtained in a run of 100 GeV electrons as the one shown in Figure 4.8 (2001 test beam data); as can be clearly seen, the extension of these distributions is due to the beam width

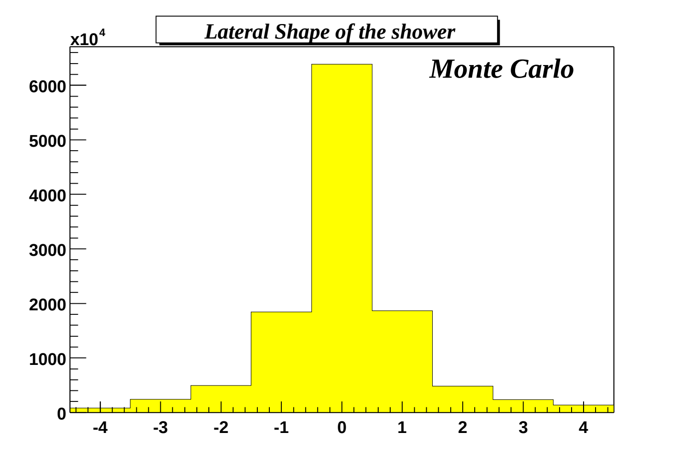

Figure 4.7: Lateral shape of the energy deposit; Monte Carlo simulation for 128 GeV electrons impinging perpendicularly on the ECAL. The x axis is the distance in pixel units (1 cell = 0.925 cm) from the initial particle direction.

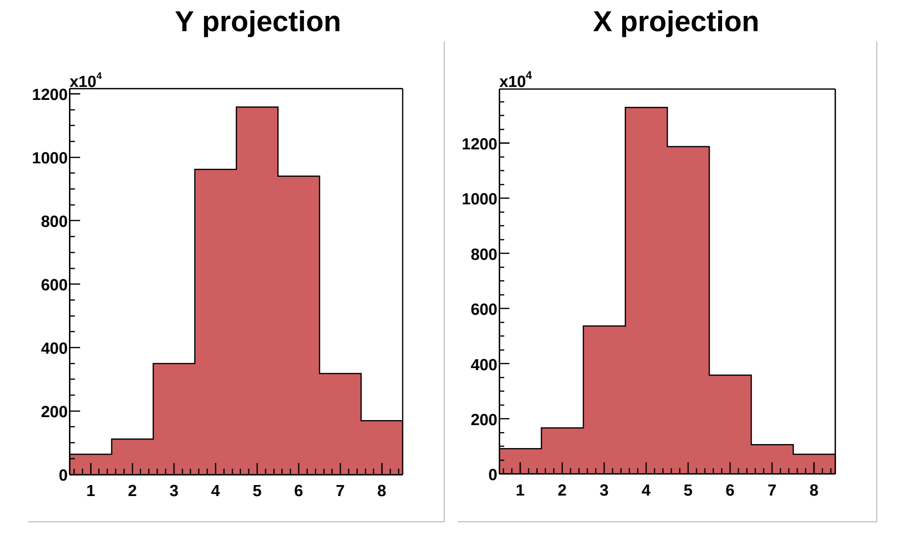

Figure 4.8: Lateral shape of the energy deposit in the two views during the 100 GeV electron run of 2001.

[1]More precisely a column in the x view and one in the y view.

and not to the intrinsic width of the electromagnetic showers in the ECAL.

Because of the beam width, in each run particles hit the calorimeter in different cells. Figure 4.10 shows the energy deposit in plane number 10 for 100 GeV electrons (2001 test beam data); this layer is oriented along y i.e. the direction where the beam is wider. In the cells, different peaks, corresponding to a high energy deposit, can be clearly noted; these correspond to different impact points of the particles on the ECAL: electrons impinging on one column release a large amount of energy in the cells of the same column and small amount in the surrounding cells. In Figure 4.10 the shaded regions correspond to the same events: (*top*) events with a large energy deposit in cell number 5, have a low energy release in cell numbers 4 and 6; (*bottom*) events with a large energy deposit in cell number 6, have a small energy release in cell number 5 and an even smaller one in cell number 4. As can be clearly seen, events lying in one high energy peak are independent from those in another peak.

Moreover, it is important to notice that the mean energy value corresponding to each high energy peak depends also on shape of the beam (i.e. the abundance and the position of the particles) and on the position of the beam impact point relative to the ECAL cells. During the 2001 ECAL test beam, the beam was ~ 3 pixel wide in the y direction and ~ 2 pixel wide in the x direction; within this area the particles were uniformly distributed. For all the runs used to equalize the ECAL, the beam was well centered on the cells (see Figure 4.9); this is also consistent with the fact that the integrals above the three high energy peaks shown in Figure 4.10 are almost the same.

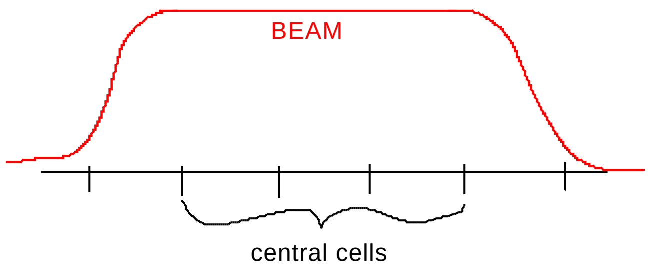

Figure 4.9: Beam profile along y during the 2001 ECAL test beam. The beam was centered over three cells. Thus the number of particles impinging on these central cells was the same, and they were uniformly distributed over the surface of each pixel.

By assuming that for each plane the high energy peaks in different cells correspond to the same energy release, the peak parameters can be used to equalize the

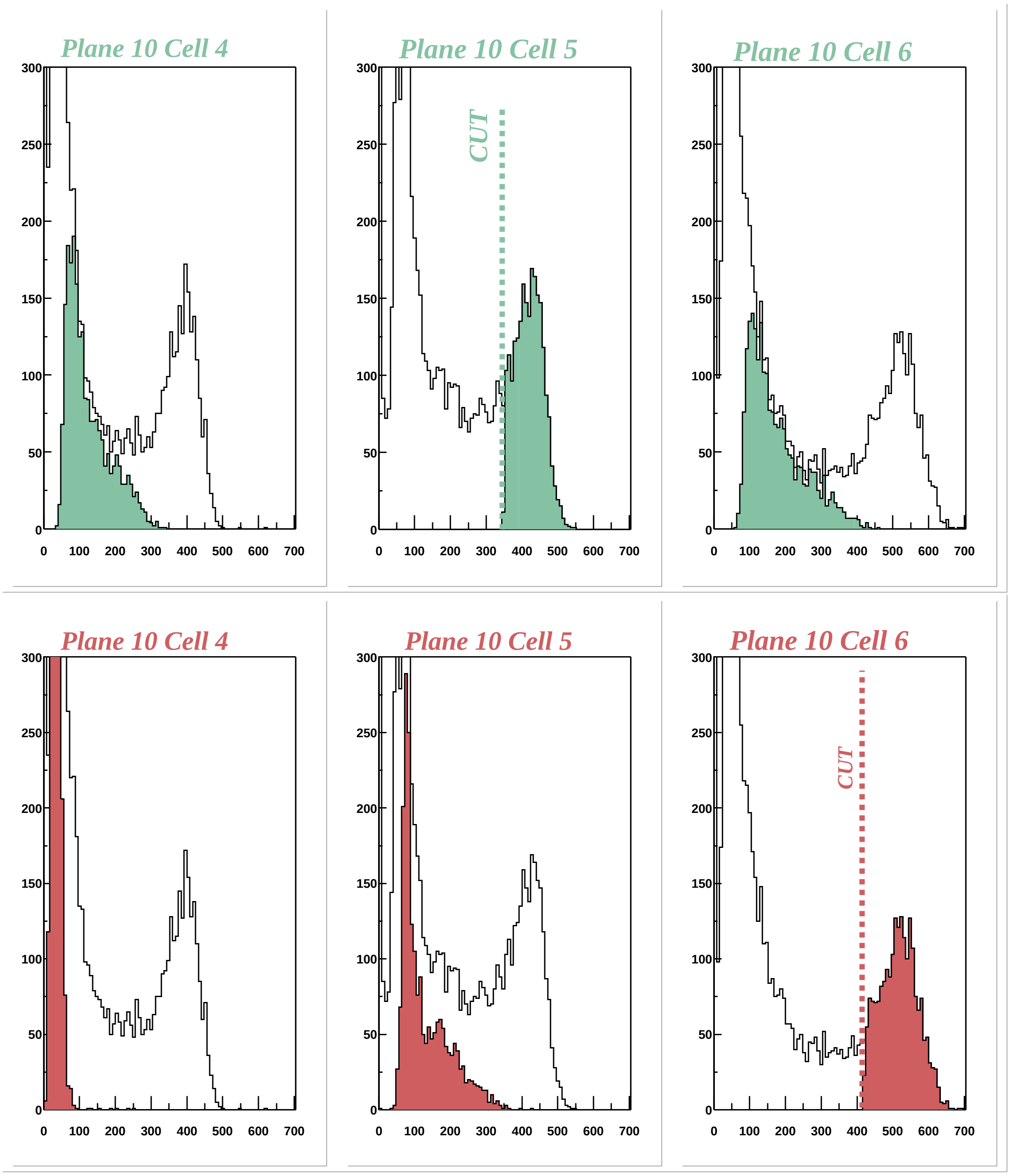

Figure 4.10: Energy deposit in the central cells of plane number 10 by 120 GeV electron events. *Top*: cut on the energy deposit in cell number 5; *bottom*: cut on the energy deposit in cell number 6. Shaded regions correspond to the same events.

response of these cells.

During the 2002 ECAL test beam a complete scanning of the instrumented cells of both the x and y views was performed with 120 GeV electrons. In this case the beam was narrower in both directions: the spot diameter was $\sim 1.8\ cm$ along x ($\simeq 2$ pixels), and $\sim 1\ cm$ along y ($\simeq 1$ pixel). The fact that the beam is still well centered on the cells during the entire scanning (the step between two consecutive runs is equal to 0.9 cm) allows to assume that the central column for each run contains the same number of particles.

Therefore, taking for each run the cells in the central column (both in x and y) a gaussian fit was carried out and the mean value was set to a common value (for each plane) given by the average of different peaks.

Equalization among different planes

The second step in the equalization procedure with electrons concerns the equalization among different planes.

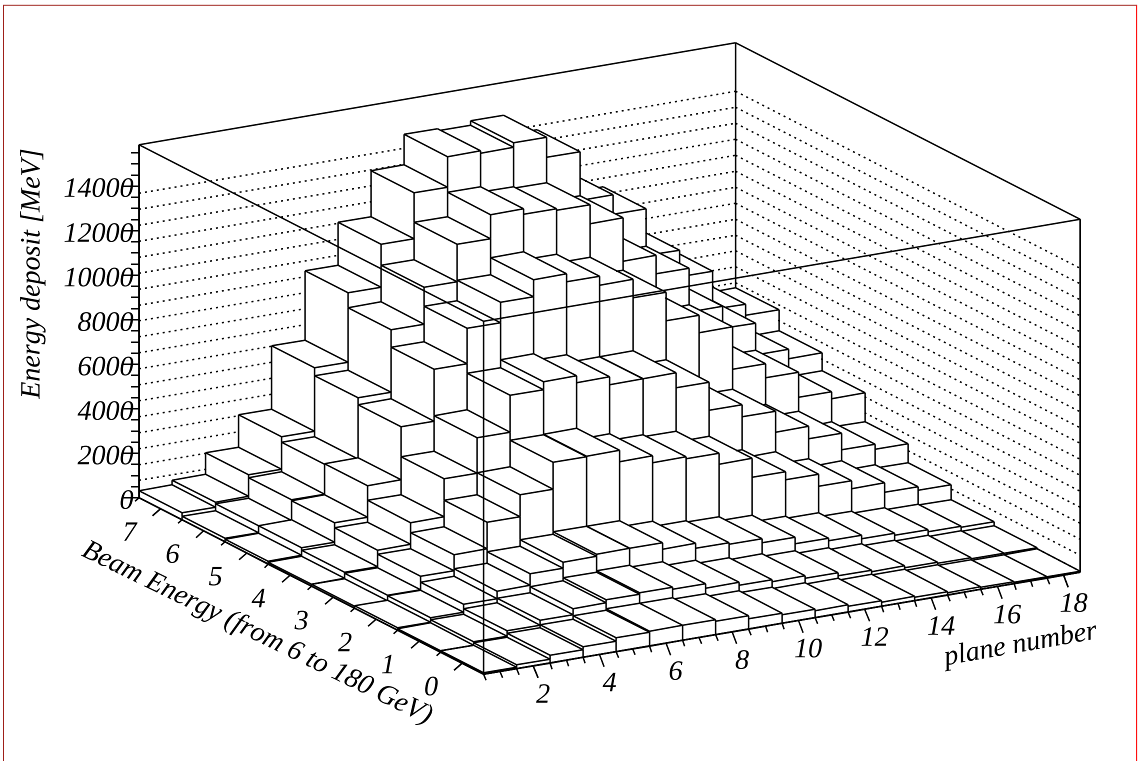

Figure 4.11: Average longitudinal shapes of electromagnetic showers for different beam energies (before equalization among different planes).

As seen in Section 3.2 the longitudinal shape of an electromagnetic shower can be fitted by a Gamma function (see Eq. 3.1). Thus a *multifit* on the average longitudinal shapes of the electromagnetic showers at different beam energies was performed. The beam energies used for this fit were 6, 10, 20, 50, 80, 120, 150 and 180 GeV. For each beam energy the average longitudinal development of the showers was calculated using about 10,000 electrons impinging perpendicularly on the middle of the instrumented part of the ECAL. Then the *multifit* was performed: a fit with 3 different *free parameters* for each fixed energy, corresponding to b, α and E_0 (see Eq. 3.1) and 18 more parameters, common to all the longitudinal shapes for different energies, that weigh the signal of each plane. Figure 4.11 shows the bidimentional histogram input to the fit procedure. The *multifit* was performed using the *MINUIT* libraries.

The results for the 18 parameters from the *multifit* were used as equalization coefficients for the ECAL planes.

4.4 Comparison between the results of the two equalization methods

At the end of the equalization procedure with MIPs on the 2002 ECAL test beam data, the average longitudinal shapes for different beam energies were obtained. Each average longitudinal development was obtained fitting the energy distribution in each ECAL plane, with a gaussian function, and taking the mean value. The resulting longitudinal shapes at 6, 10, 20, 50, 80, 120, 150 and 180 GeV are shown in Figure 4.12 together with their fits, performed with Gamma functions. As can be clearly seen, these distributions show some problems, moreover the energy deposit in each layer does not follow very well a Gamma distribution, especially in the exponential drop.

Another problem was evidenced studying the different energy distributions for runs with different impact points on the ECAL surface. During the test beam, the instrumented part of the ECAL was scanned with electrons of 10 and 120 GeV; unfortunately for the other beam energies there are just a few runs with impact points different from the middle.

Figure 4.13 shows the normalized energy distributions of 120 GeV electron runs

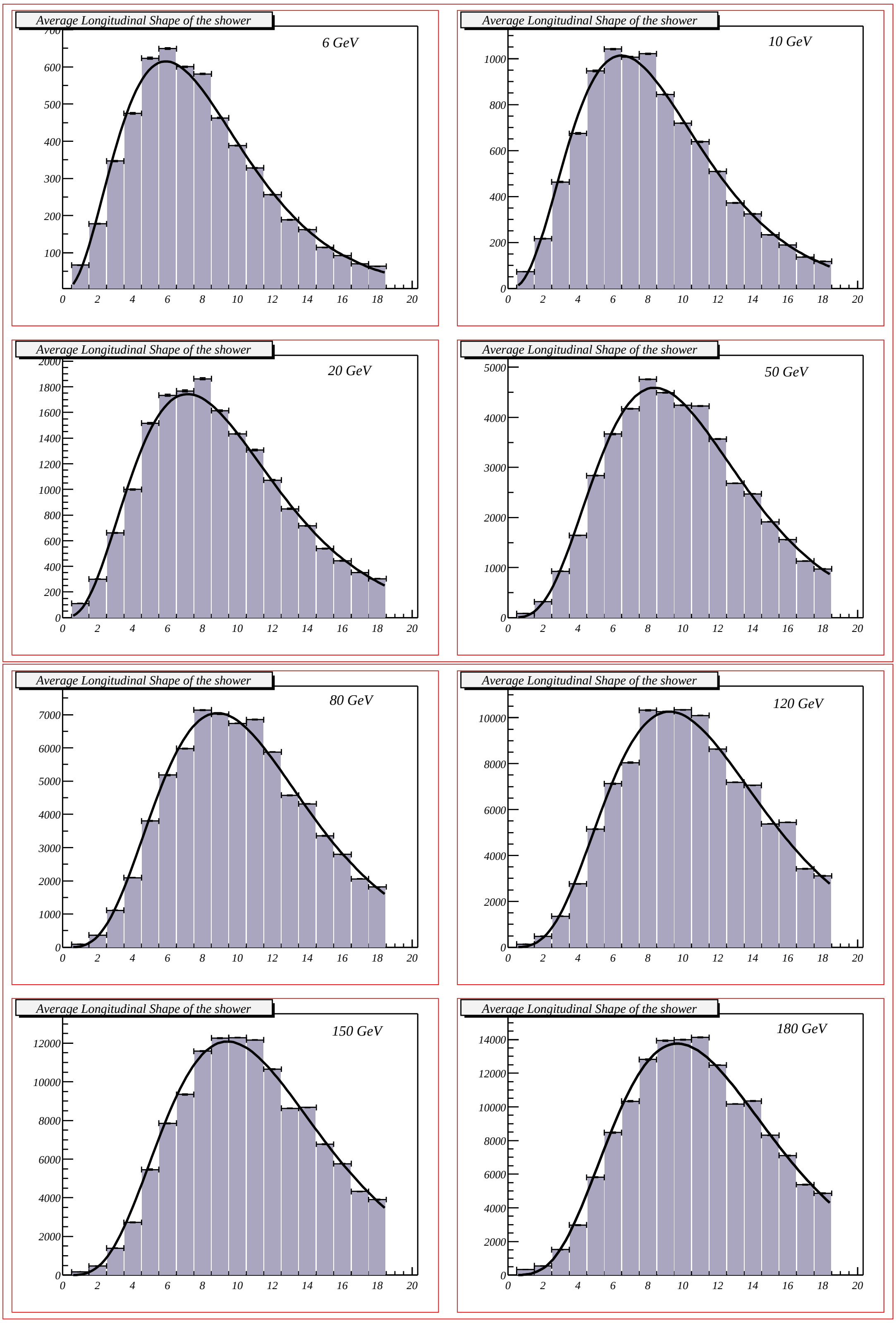

Figure 4.12: Average longitudinal shapes for different beam energies, resulting from the equalization with MIPs.

with different impact points on the ECAL; each impact point is 0.9 cm away from the preceding one in both x and y, along a diagonal line on the ECAL surface. The histogram in *red* shows the energy distribution for events impinging almost in the middle of the instrumented part of the ECAL; this sample contains about 10,000 events, each of the others contain about 4,000 events. These energy distributions have very different mean values and some of them also a larger width.

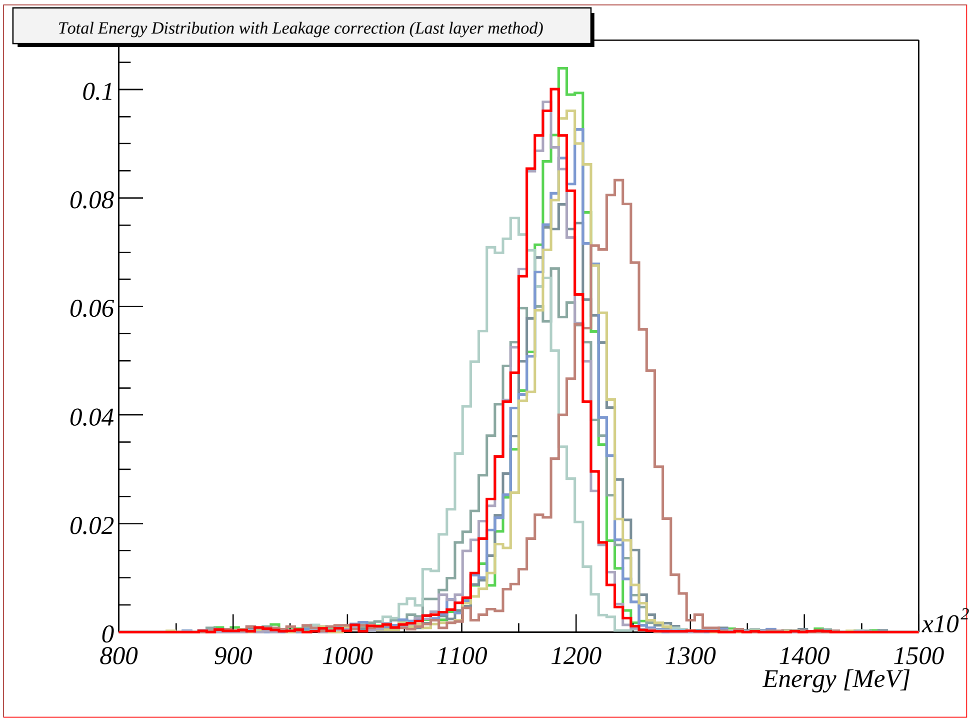

Figure 4.13: Normalized energy distributions of 120 GeV electrons runs for different beam impact points on the ECAL, after equalization with MIPs. The histogram in *red* gives the energy distribution of events impinging almost in the middle of the instrumented part of the ECAL.

It is evident that differences in cell responses are still present, thus the equalization with electrons was carried out.

The results are shown in Figure 4.14 for the average longitudinal shapes, and in Figure 4.15 for the energy distributions. As it is possible to notice, the results are better in both cases.

The longitudinal shapes follow very well a Gamma distribution; except for superlayer number 4 (planes number 7 and 8) that seems to have too high a gain, but this effect is visible only for beam energies smaller than 80 GeV.

The energy distributions for 120 GeV electrons have the same mean value and

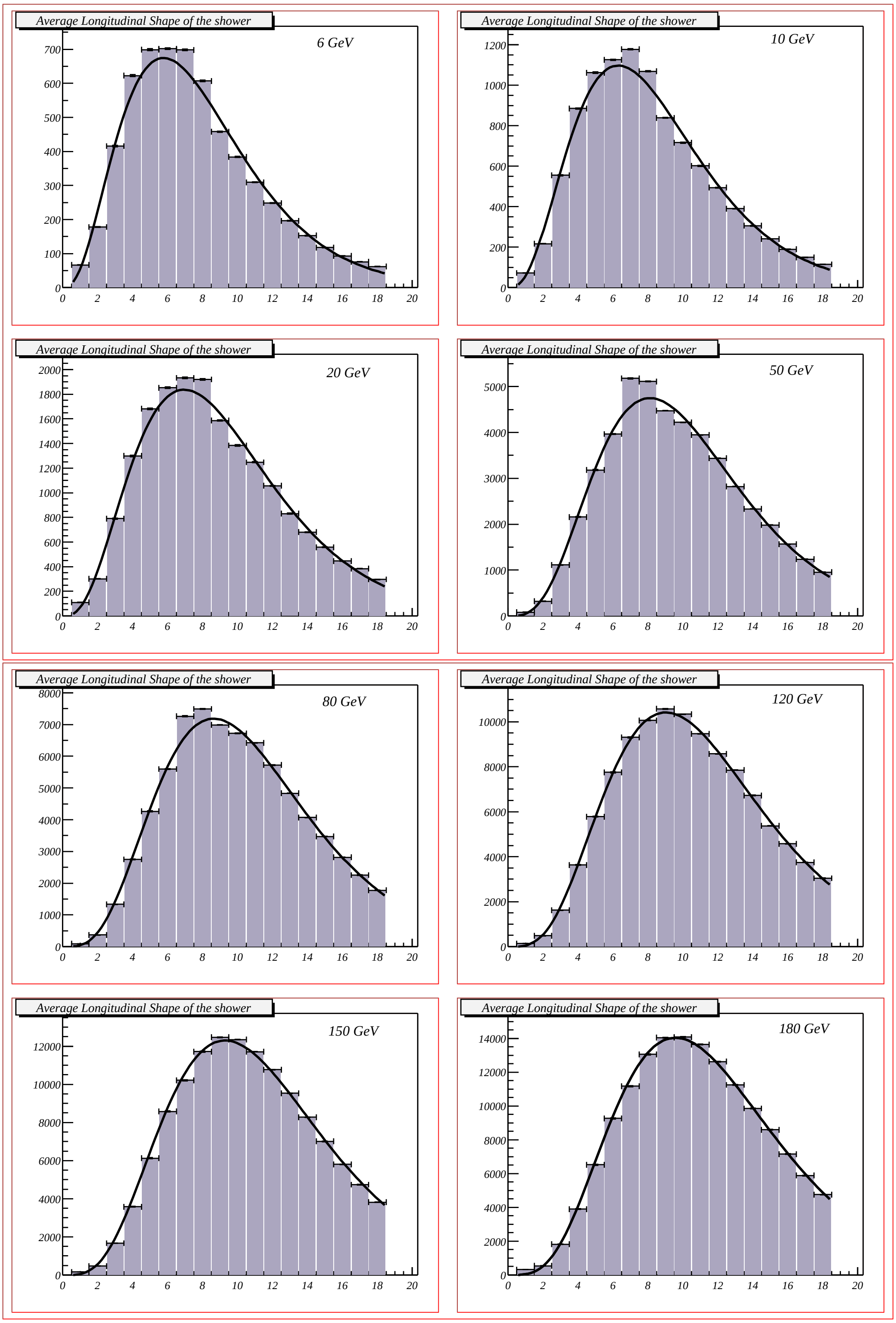

Figure 4.14: Average longitudinal shapes for different beam energies, after the equalization using electrons.

the widths of the distributions are now very similar; with the only exception a run (in *light-blue*) where beam impact direction crosses a dead PM. All the dead PMs or pixels were replaced by an energy deposit that is the mean value between the nearby ones in the longitudinal direction for the same view. This correction seems to work well, but some problems are still visible if the dead PM or pixel is in the high energy deposit part of the shower.

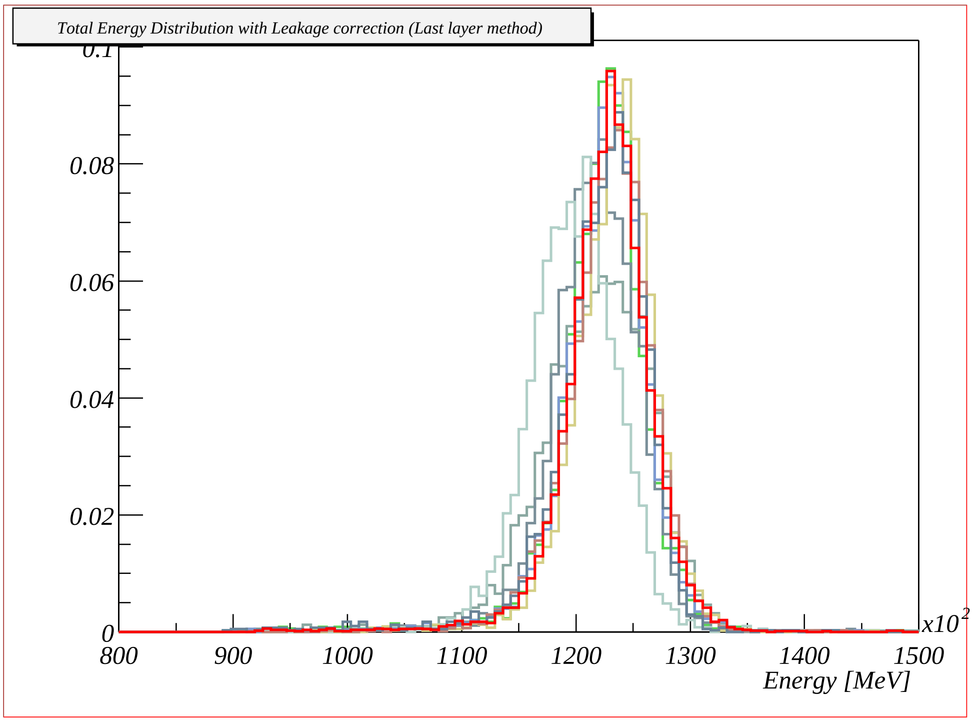

Figure 4.15: Normalized energy distributions of 120 GeV electrons runs for different beam impact points on the ECAL, after the equalization using electrons. The *red* line is for the energy distribution of events impinging almost in the middle of the instrumented part of the ECAL.

4.5 Measurement of the radiation length

As seen in Section 3.2, there is a logarithmic relationship between the maximum of the electromagnetic shower and the energy of the initial particle (see Eq. 3.2). Measuring the position of the maximum of the shower in the ECAL (z_{max}) for different electron energies, it is possible to estimate the radiation length X_0 of the calorimeter. In fact, from Equation 3.2, we obtain:

$$z_{max} = X_0 \;\; ln(E_0) + const \tag{4.1}$$

where, if the maximum of the shower is expressed in layer units (1 $l.u. = 0.925\ cm$), also the radiation length is expressed in layer units.

The shower maximum, for each different beam energy, was obtained in three different ways:

a) fitting the average longitudinal profile at a given beam energy;

b) fitting the longitudinal profile event by event and taking the mean value of the z_{max} distribution;

c) fitting the longitudinal profile event by event and taking the mean value of a gaussian fit performed around the maximum of the z_{max} distribution.

The results of the fits for the average longitudinal profiles (Figure 4.14) are shown in Table 4.1. Here the α and b parameters are given together with the z_{max} calculated[2] (procedure **(a)**).

Energy	α	b	z_{max} $[l.u.]$
6 GeV	2.682 ± 0.005	0.4656 ± 0.0008	5.76 ± 0.02
10 GeV	2.956 ± 0.005	0.4694 ± 0.0007	6.30 ± 0.02
15 GeV	3.031 ± 0.005	0.4523 ± 0.0007	6.70 ± 0.02
20 GeV	3.003 ± 0.006	0.4326 ± 0.0008	6.94 ± 0.02
30 GeV	3.590 ± 0.009	0.478 ± 0.001	7.51 ± 0.03
50 GeV	3.830 ± 0.005	0.4721 ± 0.0006	8.11 ± 0.02
80 GeV	3.983 ± 0.005	0.4611 ± 0.0005	8.64 ± 0.02
120 GeV	4.061 ± 0.005	0.4500 ± 0.0005	9.02 ± 0.02
150 GeV	4.073 ± 0.005	0.4384 ± 0.0005	9.29 ± 0.02
180 GeV	4.236 ± 0.006	0.4424 ± 0.0006	9.57 ± 0.02

Table 4.1: Results of the fits for the averages longitudinal shape of the shower, performed using the Eq. 3.1.

Two examples of longitudinal shower profiles of single events are shown in Figure 4.16; the one on *top* is a 10 GeV electron while the *bottom* one is an 80 GeV electron. In these plots the energy deposits in each ECAL plane are shown; the

[2] $z_{max} = \alpha/b$ as shown in Sect 3.2

vertical error bars correspond to the *sigma*s of the energy deposit distributions in each plane for a fixed beam energy. For each event a fit to the longitudinal profile

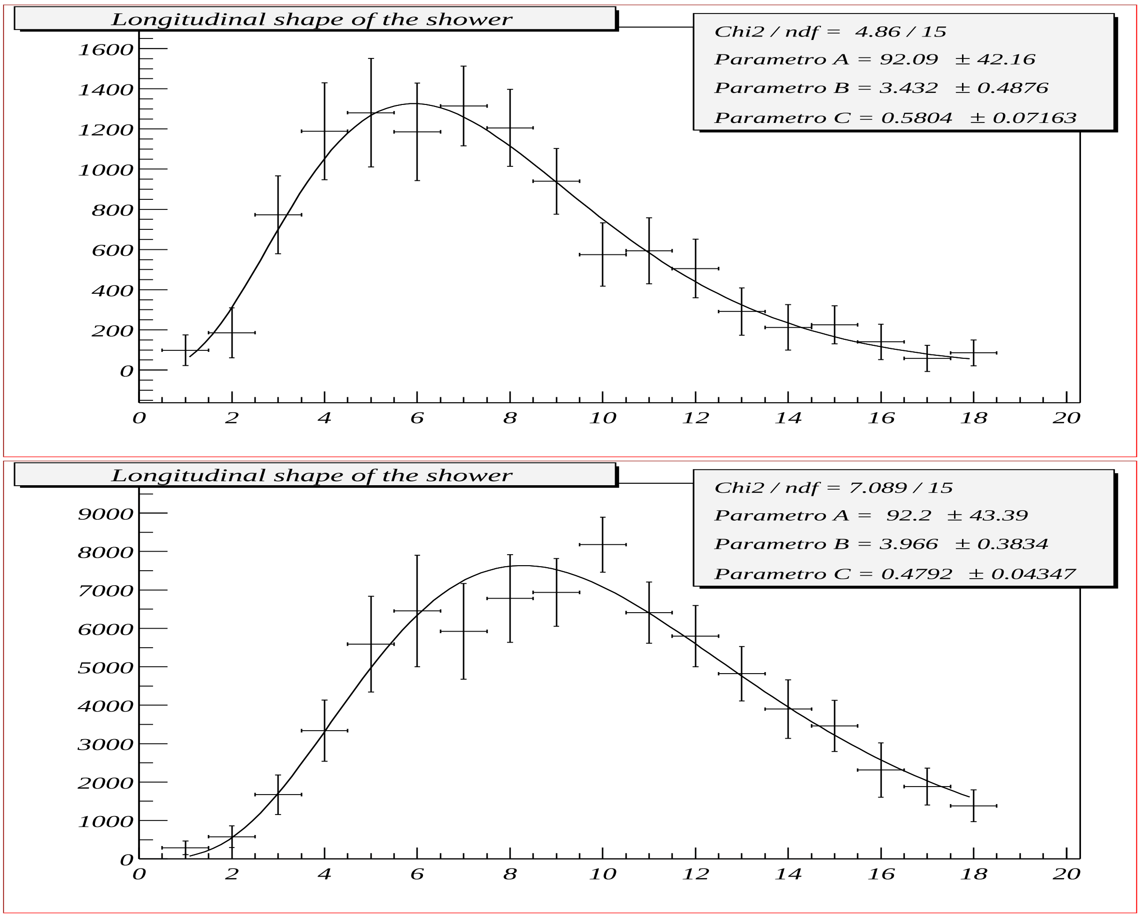

Figure 4.16: Fits of the longitudinal profiles for a single electron of 10 *GeV* (*top*) and an electron of 80 *GeV* (*bottom*).

was performed with Gamma functions (Eq. 3.1) and the maximum ($z_{max} = \alpha/b$) was calculated. In Figure 4.17 the distributions of z_{max} for different beam energies are shown. From these distributions both the mean values (procedure **(b)**) and the mean values of the gaussian fits of the peaks (procedure **(c)**) were extracted.

The results obtained using the different procedures are shown in Figure 4.18. Here the position of the maximum (in layer unit) is plotted as a function of $ln(E_0)$ (E_0 is the beam energy). From the slopes of these three curves is possible to obtain an estimate of the radiation length. The results of the fits are given in Table 4.2: they are clearly consistent with each other.

This implies an ECAL total thickness of $\simeq 17\ X_0$.

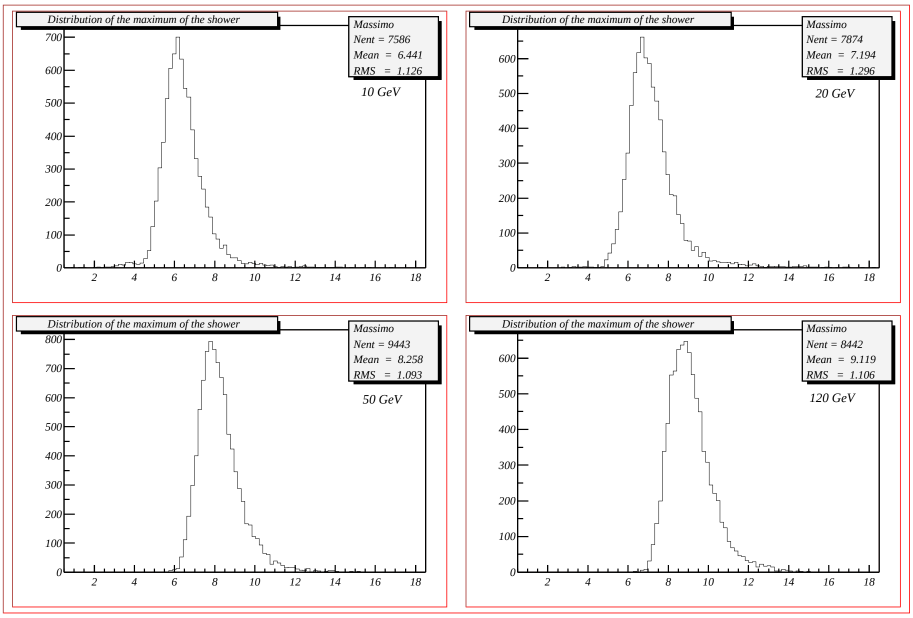

Figure 4.17: Distributions of z_{max} obtained from fits of the longitudinal shape event by event, for beam energies of 10, 20, 50 and 120 GeV.

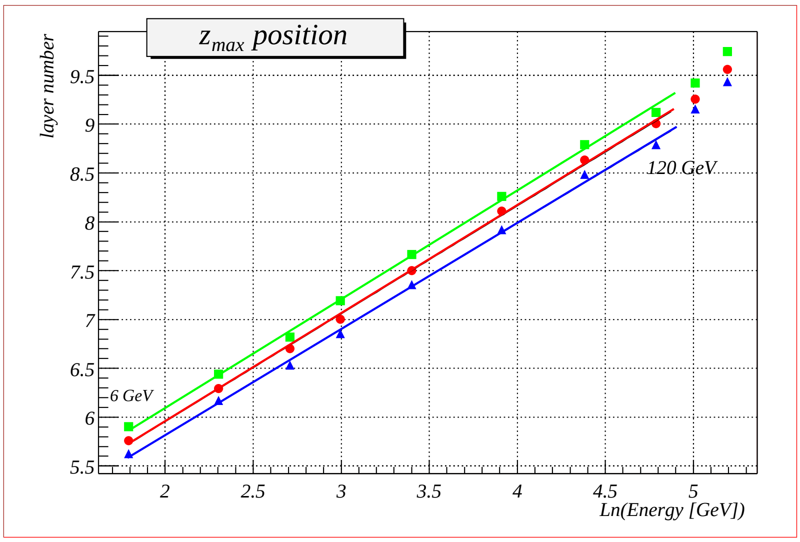

Figure 4.18: Maxima of the shower (z_{max}), estimated with the three different procedures, plotted as a function of $ln(E_0)$. *Red circles*: maxima of the average longitudinal profiles (procedure **(a)**); see Table 4.1. *Green squares*: mean values of the distributions of maxima (procedure **(b)**). *Blue triangles*: mean values of the gaussian fits of the distributions of maxima (procedure **(c)**).

Procedure	X_0 $[l.u.]$	X_0 $[cm]$
(a)	1.10 ± 0.02	1.02 ± 0.02
(b)	1.11 ± 0.03	1.03 ± 0.03
(c)	1.08 ± 0.03	1.00 ± 0.03

Table 4.2: Radiation length measurements resulting from the three different calculations.

4.6 Corrections for longitudinal leakage

For electrons with an initial energy $\gtrsim$10 GeV the longitudinal leakage is not negligible, as it is possible to observe in Figure 4.14. Thus the energy measurement needs a correction for the longitudinal leakage; two methods were applied.

The first method is based on the fit, event by event, of the longitudinal shape of the shower: the energy leaking out of the ECAL is obtained by integrating the curve resulting from the fit, over the t range lying outside the calorimeter (i.e. for $t > 18$) and is then added to the energy deposited inside (see Figure 4.19).

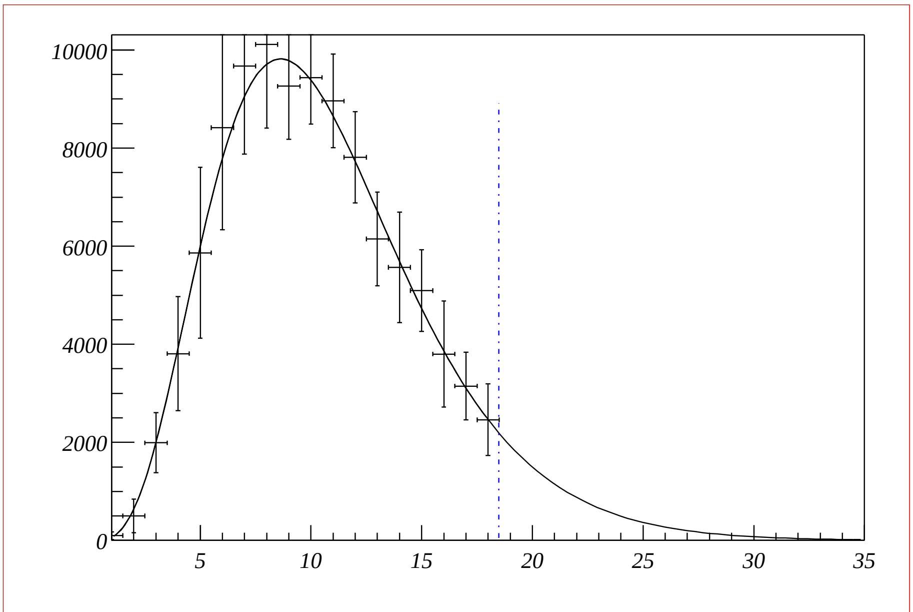

Figure 4.19: Fit of the longitudinal profile for a 120 GeV electron. The integral of the curve on the right of the dashed line (out of the ECAL) is added to the energy deposit inside the calorimeter.

The second method is called "last layer" method. It is based on the hypothesis that the energy deposit in the layers with index $M > N$ depends mostly on the ratio between the energy deposit in layer N and that deposited in all the layers with index $\leq N$. This means that the energy leaking off the ECAL is a function ot the ratio between the energy deposit in the last layer and the total energy deposit in the calorimeter. Assuming that the energy leakage has a linear dependence on this ratio, one can write:

$$E - E_{DEP} = \alpha \, \frac{E_{LAST}}{E_{DEP}} \tag{4.2}$$

where E_{DEP} is the energy deposit in the calorimeter and E_{LAST} is the energy deposit in the last layer of the ECAL. In Figure 4.20 are plotted the E_{DEP}/E_{BEAM} vs. E_{LAST}/E_{DEP} for different beam energies (E_{BEAM} is just a costant in each

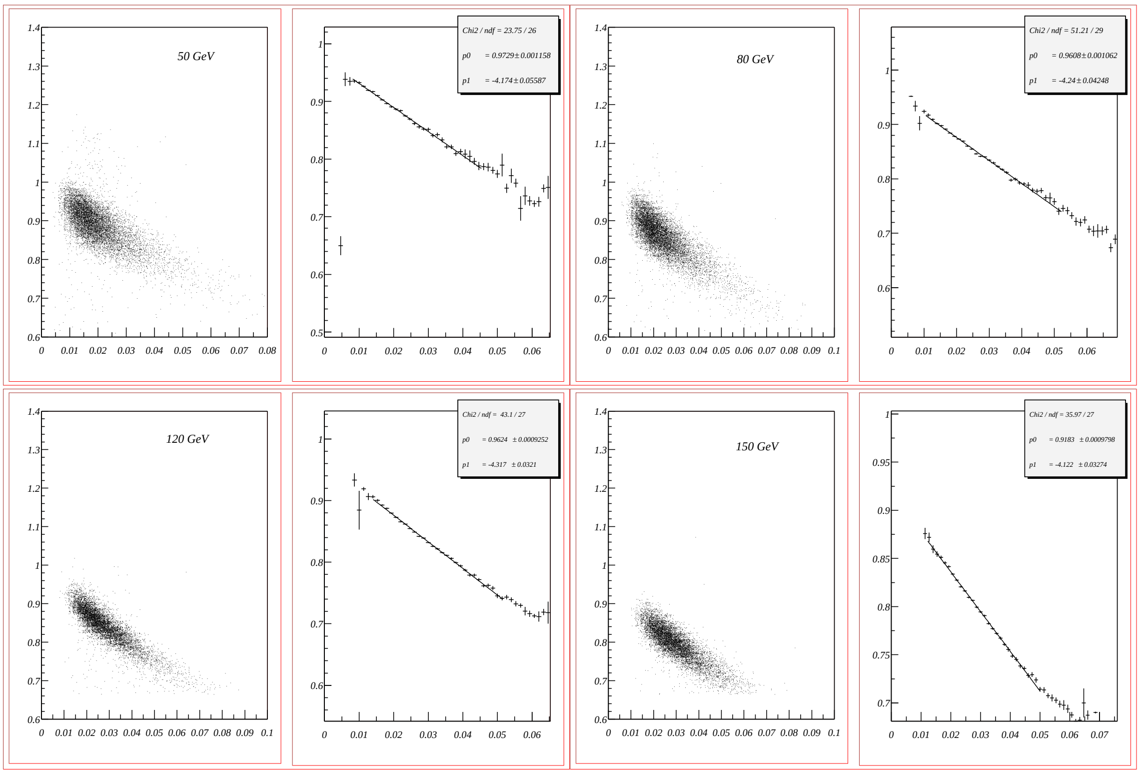

Figure 4.20: Plots of E_{DEP}/E_{BEAM} vs. E_{LAST}/E_{DEP} for different beam energies. E_{DEP} is the total energy deposit in the calorimeter from each electron, E_{BEAM} is the beam energy and E_{LAST} is the energy deposit in the last plane of the ECAL. On the left of each scatter plot, there is the profile of the plot; it is fitted with a straight line.

plot); it can be noticed that the assumption of a linear dipendence of $E - E_{DEP}$ on E_{LAST}/E_{DEP} is correct; in fact Eq. 4.2 can be written as:

$$\frac{E_{DEP}}{E_{BEAM}} = \frac{E}{E_{BEAM}} - \alpha' \, \frac{E_{LAST}}{E_{DEP}}$$

where $\alpha' = \alpha/E_{BEAM}$. From the fits of the profiles of these plots, α' was extracted and parameterizated as a function of E_{BEAM}. Approximating $\alpha'(E_{BEAM}) \simeq \alpha'(E_{DEP})$, the energy of each electron can be calculated from E_{DEP} as follow:

$$E = E_{DEP} - \alpha'(E_{DEP})\ \frac{E_{LAST}}{E_{DEP}}$$

where $\alpha'(E_{DEP})/E_{DEP}$ is a negative costant.

The results of these leakage correction methods are shown in Figure 4.21 for 10, 20, 50, 80, 120 and 150 GeV beam energies: the *shaded* distributions show the distributions of total energy deposit in the calorimeter; the *blue dashed* lines are the energy distributions after the leakage corrections using the longitudinal fits event by event; the *red solid* lines are the energy distributions after the leakage corrections using the "last layer" method. The results of the two methods differ by a few percent at each beam energy (the mean values obtained with the "last layer" method are slightly larger) which can be corrected by a constant factor in the calibration, and the width of the distributions are almost equal; it means that the two correction methods for the longitudinal leakage are equivalent.

4.7 ECAL Linearity and Resolution

As it is possible to notice in Figure 4.21 at the end of the present analysis some problems are still present in the energy linearity. In Figure 4.22 are shown the linearity curves and the residuals between measured and nominal beam energy before and after the leakage correction using the "last layer" method. The red circles are the results for runs with beam impact points in the middle of the instrumented part of the ECAL; while the blue ones are for different impact points. The differences in the results of different runs at the same beam energy provide an estimate of the systematic error in the energy measurement. The systematic error is mostly due to the equalization procedure, the correction for dead PMs and pixels, for light attenuation and for the high-low gain ratio.

The energy leaking off the calorimeter is $\sim 4\%$ of the total energy at 10 GeV and $\sim 20\%$ at 180 GeV. A good linearity, after the leakage correction, is found between 6 and 20 GeV. The linearity deviation at 3 GeV is probably due to the poor purity of the electron beam. From 30 to 120 GeV there is a residual constant missing energy equal to $\sim 5\%$ of the total energy and at 150 and 180 GeV the deviation

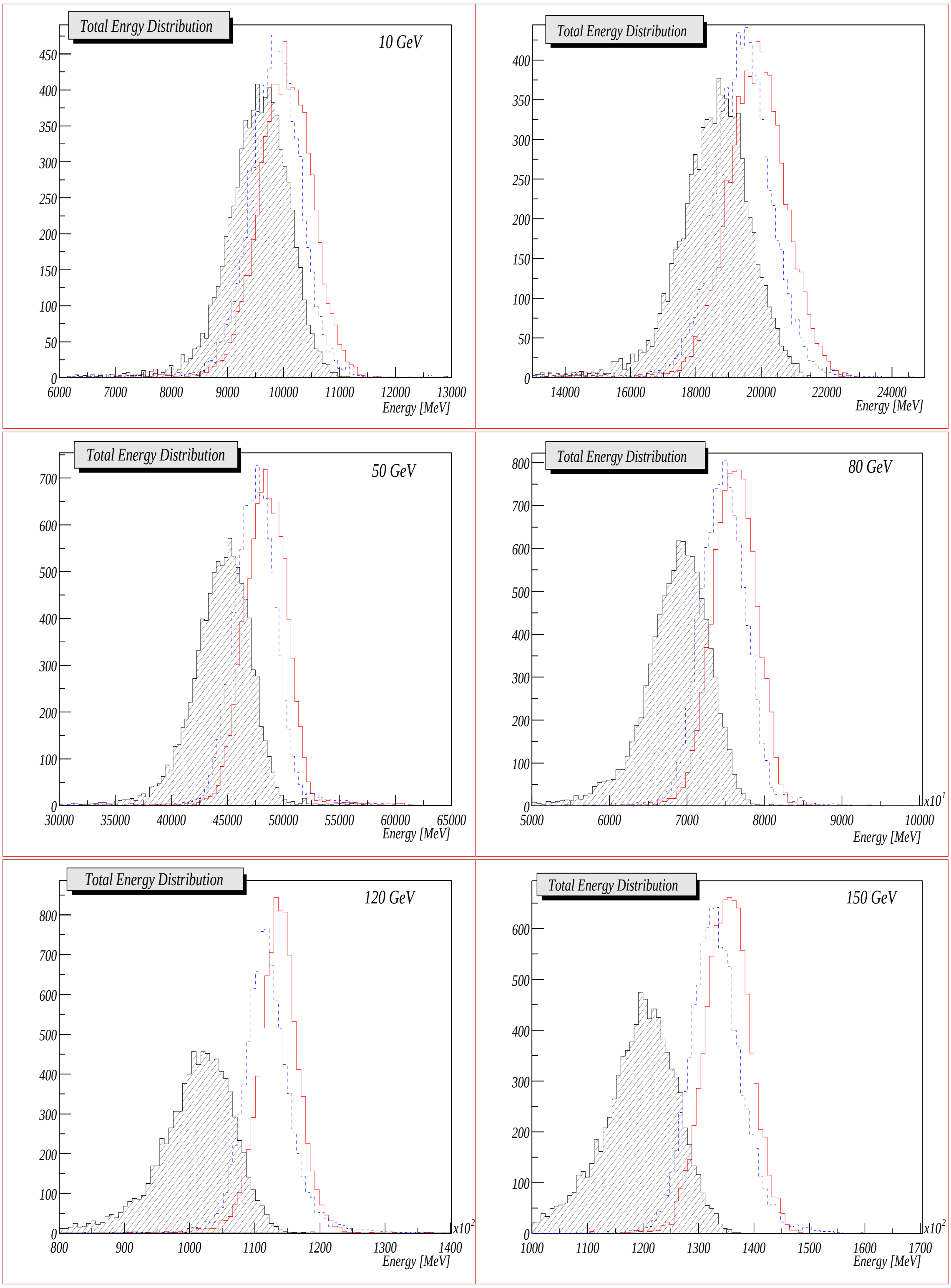

Figure 4.21: Total energy distributions for different beam energies. The *shaded* distribution is the total energy deposited in the calorimeter; the *blue dashed* line is the energy distribution after the leakage correction using longitudinal fits event by event; the *red solid* line is the energy distribution after the leakage correction using the "last layer" method.

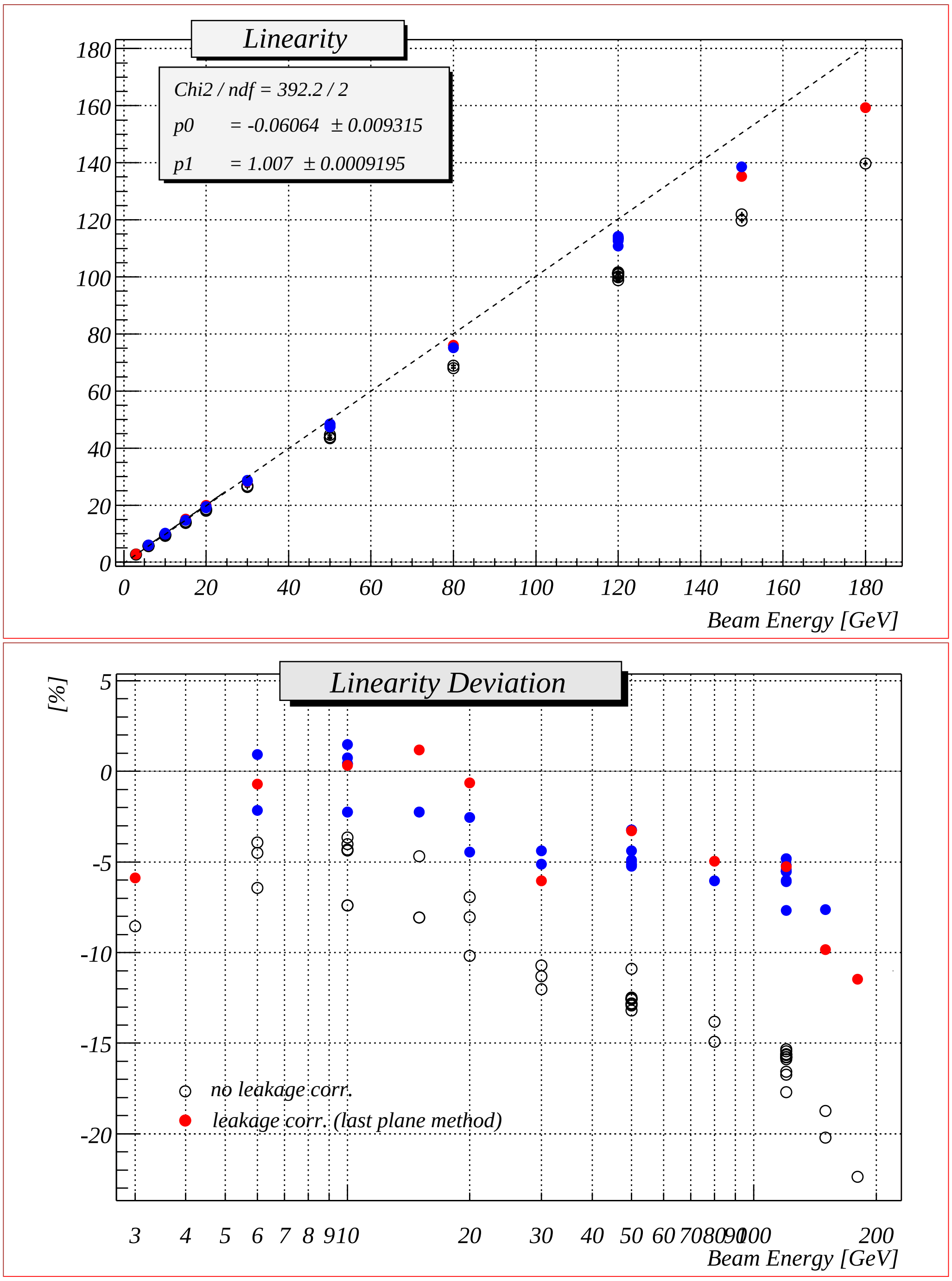

Figure 4.22: *Top*: Energy linearity curve; the fit is carried out in the energy range between 6 and 20 *GeV*. *Bottom*: Residuals between measured energy and nominal beam energy. The open circles are for the total energy deposit in the calorimeter without the leakage correction The filled circles are corrected for leakage with the "last plane" method; the red ones are for runs with beam impact points in the middle of the instrumented part of the ECAL, the blue ones are for runs with different impact points.

from linearity is greater. Probably the difference between the two energy ranges, below 20 GeV and above 30 GeV, is due to ADC non-linearity such as already seen in the high/low gain ratio calibration (the energy deposit for events with energies larger than 30 GeV is mostly obtained from the low gain output); probably two different calibration factors for the two ranges will be needed.

The energy resolution of the calorimeter is shown in Figure 4.23 where the fractional uncertainty on the energy measurement, $\sigma(E)/E$, is plotted as a function of the nominal beam energy. The red circles are for runs with beam impact points in the middle of the instrumented part of the ECAL and the blue ones are for runs with different impact points.

The result of a fit to the energy resolution distribution, after equalization with electrons and the leakage correction, is:

$$\frac{\sigma(E)}{E} = \frac{(12.0 \pm 0.1)\%}{\sqrt{E[GeV]}} \oplus (2.99 \pm 0.01)\%$$

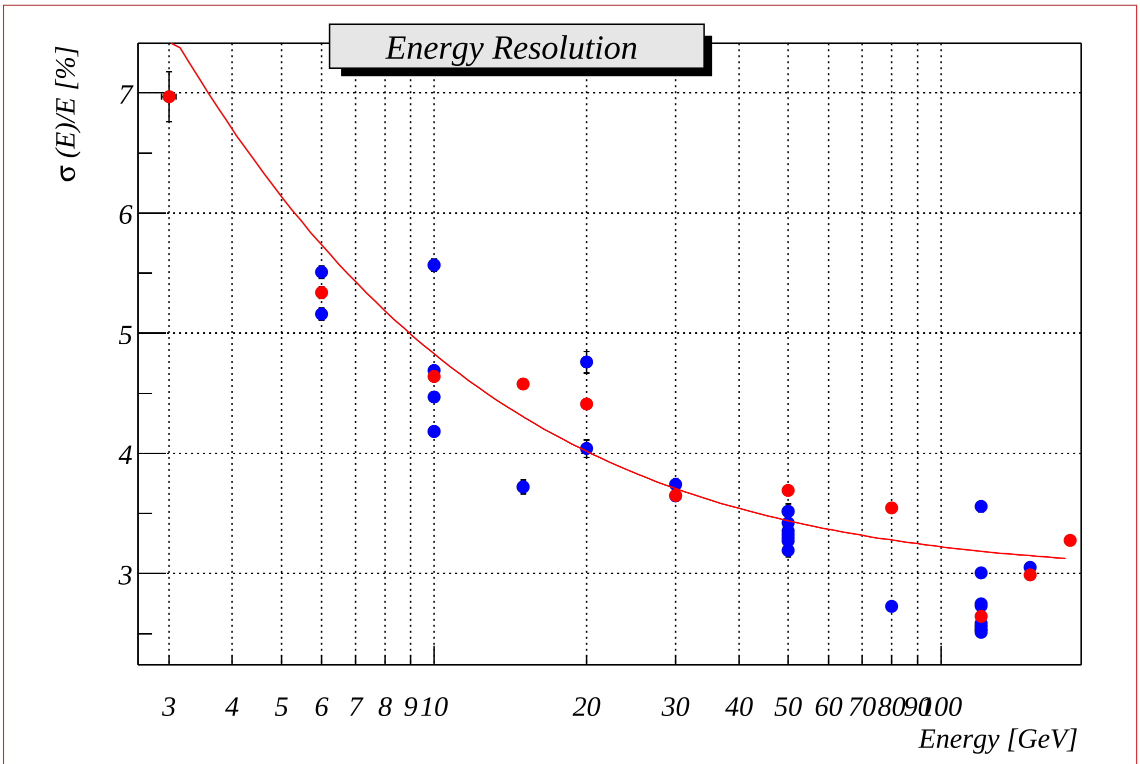

Figure 4.23: Energy resolution vs. beam energy; the red circles are for runs with beam impact points in the middle of the instrumented part of the ECAL, the blue ones are for runs with different impact points.

Chapter 5

e/p discrimination with AMS-02

5.1 The AMS-02 Monte Carlo simulation and the reconstruction program

The AMS-02 capability to identify positrons and to reject the proton background is investigated on a sample of events generated by the AMS-02 Monte Carlo simulation.

The AMS-02 geometry and performance are simulated with the dedicated AMS official simulation and reconstruction program based on the GEANT package.

A standalone program was written to read the standard AMS-02 ntuples (ROOT files) and to provide the reconstruction of the events in the calorimeter starting from the data contained in the ECALHITS block. No reconstruction is performed on the other sub-detectors and only the relevant information recorded in the ntuple was used.

Figure 5.1 shows a simulated 16 GeV positron event passing through the whole AMS-02 detector. A particle that hits the calorimeter has to pass through the other sub-detectors above: since the equivalent thickness of these materials is approximatively 0.4 X_0, the probability of emitting a bremsstrahlung γ for electrons and positrons, before reaching the ECAL, is $\sim$ 30% and the average energy of the photon corresponds to about 40% of the initial particle energy. Basically, the radiative positrons events may be classified into two different types. On one hand, the bremsstrahlung γ can convert either above or inside the spectrometer, producing tracks in addition to the primary e^+ track, and eventually well resolved showers in the ECAL. Alternatively, it can traverse the Tracker without converting and enter in the ECAL where it generates a second electromagnetic shower. In the case of

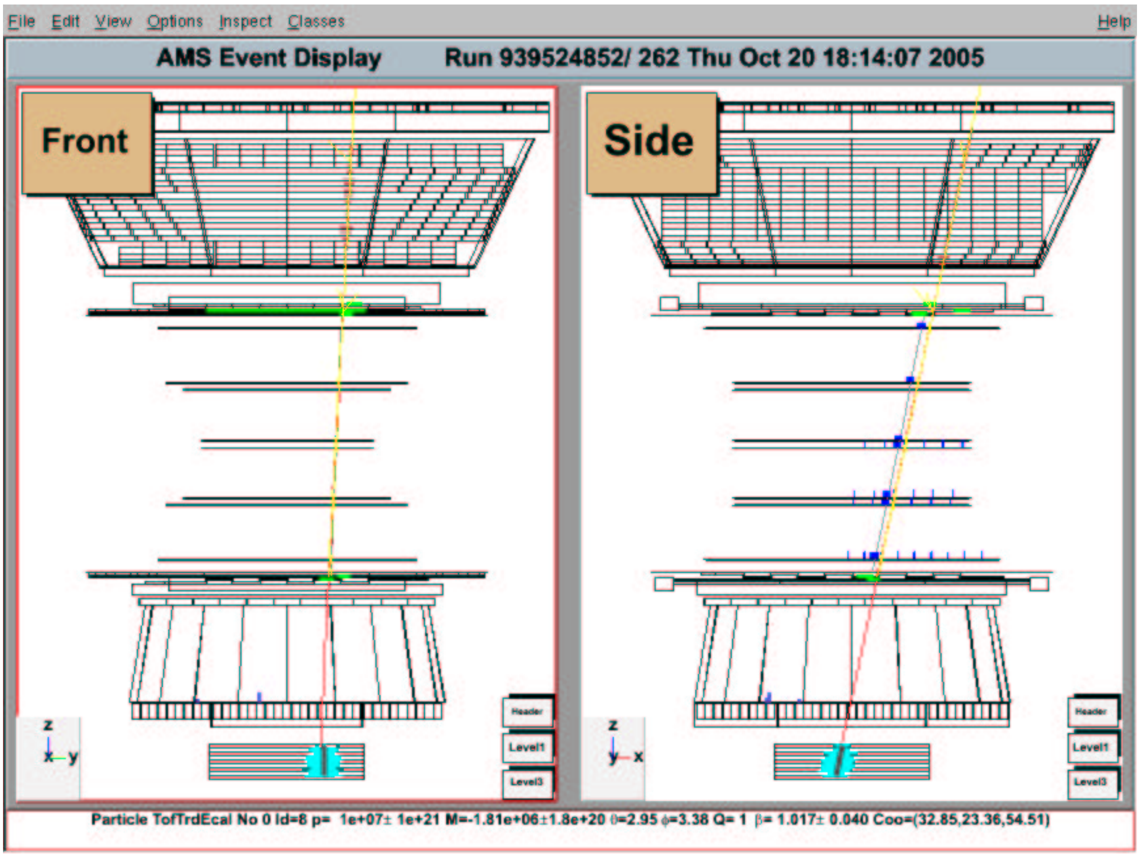

Figure 5.1: A simulated 16 *GeV* positron event in the AMS-02 detector. The particle pass through the TRD, the TOF's planes, the Tracker and the RICH, and than reaches the ECAL and originates the shower.

low energy positrons ($\lesssim$30 *GeV*), the strong deflection of the primary e^+ track in the spectrometer magnetic field produces a clear separation of the two showers in the ECAL. In the opposite case, as the energy is large enough that the bending of the primary e^+ becomes negligible compared to the spatial resolution of ECAL, the photon and positron showers overlap.

The standalone reconstruction program contains a cluster algorithm to recognize the two distinct showers inside the ECAL, for each shower the directions and impact points are calculated. To obtain the total energy measurement for the primary particle, the energies of each shower in the ECAL are added. The correction for longitudinal leakage is done using the "last layer" method as seen in Section 4.6. Figure 5.2 shows the linearity curves obtained.

The energy resolution of the calorimeter is shown in Figure 5.3 where the fractional uncertainty on the energy, $\sigma(E)/E$, is plotted as a function of the generated

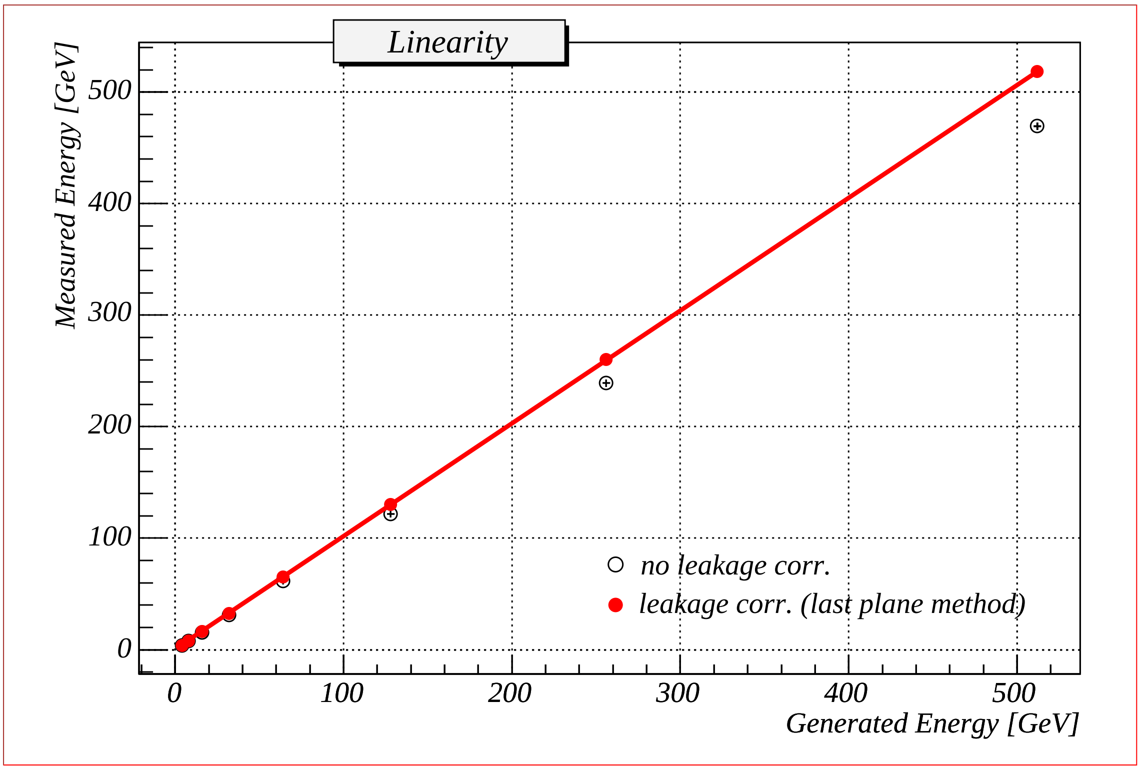

Figure 5.2: ECAL energy linearity curve for simulated positrons. The open circles are for the total energy deposit in the calorimeter without the leakage correction The filled circles are corrected for leakage with the "last layer" method.

energy. The result of a fit to the energy resolution distribution is:

$$\frac{\sigma(E)}{E} = \frac{(11.27 \pm 0.06)\%}{\sqrt{E[GeV]}} \oplus (1.02 \pm 0.01)\%.$$

To check if the simulation reproduce correctly the real ECAL scintillating fibers - lead structure (with the correct amount of glue in between), we can compare the radiation length obtained in this case with the one measured with the Test Beam data as seen in Section 4.5. The average longitudinal profiles for positrons at 4, 8, 16, 32, 64, 128, 256 and 512 GeV are shown in Figure 5.4 together with their fits, performed with Gamma functions. These longitudinal shapes (as the linearity curve and energy resolution plot) comes from averages over all events triggered and pre-selected (as we will see in Section 5.2) so, for each generated momentum, particles impact almost over all the ECAL surface and with an impinging angle between $\sim$ $(-20° \div 20°)$. The results of the fits for the average longitudinal profiles are shown in Table 5.1. Here the α and b parameters are given together with the

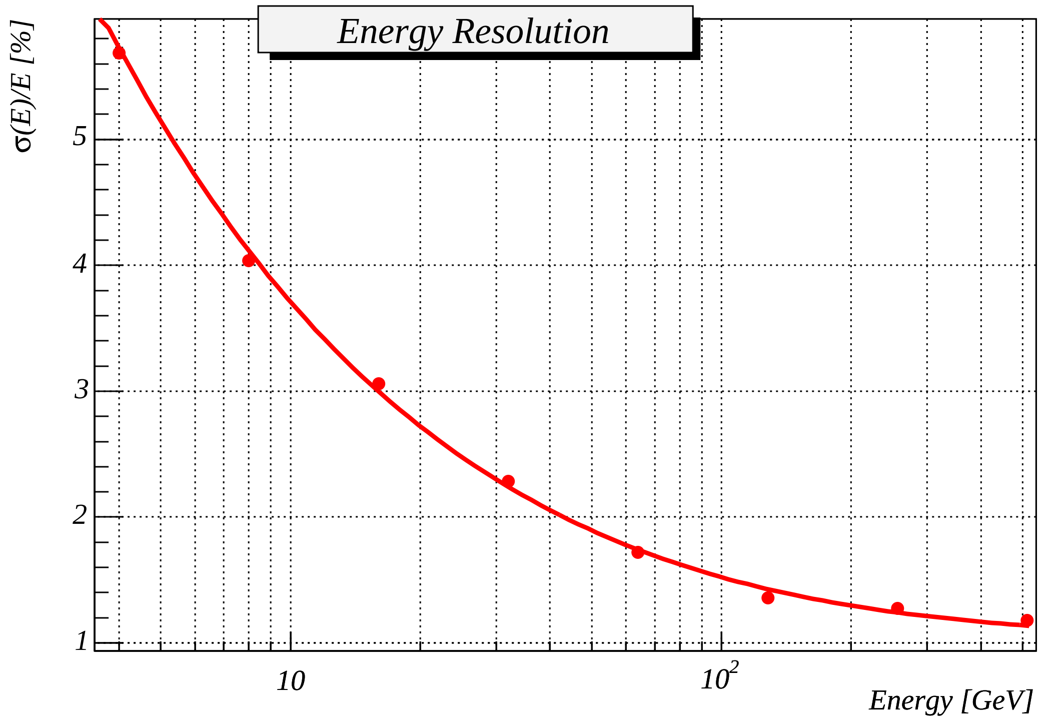

Figure 5.3: ECAL energy resolution vs. generated energy, for MC positrons.

corresponding z_{max}[1]. The radiation length obtained is:

$$X_0 = (0.93 \pm 0.01)\ cm$$

This value is quite different from the one experimentally measured during the Test Beam ($X_{0\ meas} \simeq (1.02 \pm 0.2)\ cm$). Some differences were expected because of the fact that particles in the simulated sample don't imping perpendicularly in the ECAL surface (as it was the case in the Test Beam): for these particles the "apparent radiation length" would be smaller. Nevertheless the fiber-lead-glue structure in the simulated calorimeter still has a density a little bit greater than the one of the ECAL used during the Test Beam; a new calorimeter (the flying one) is under construction and its density will be very similar to the simulated one.

[1] $z_{max} = \alpha/b$

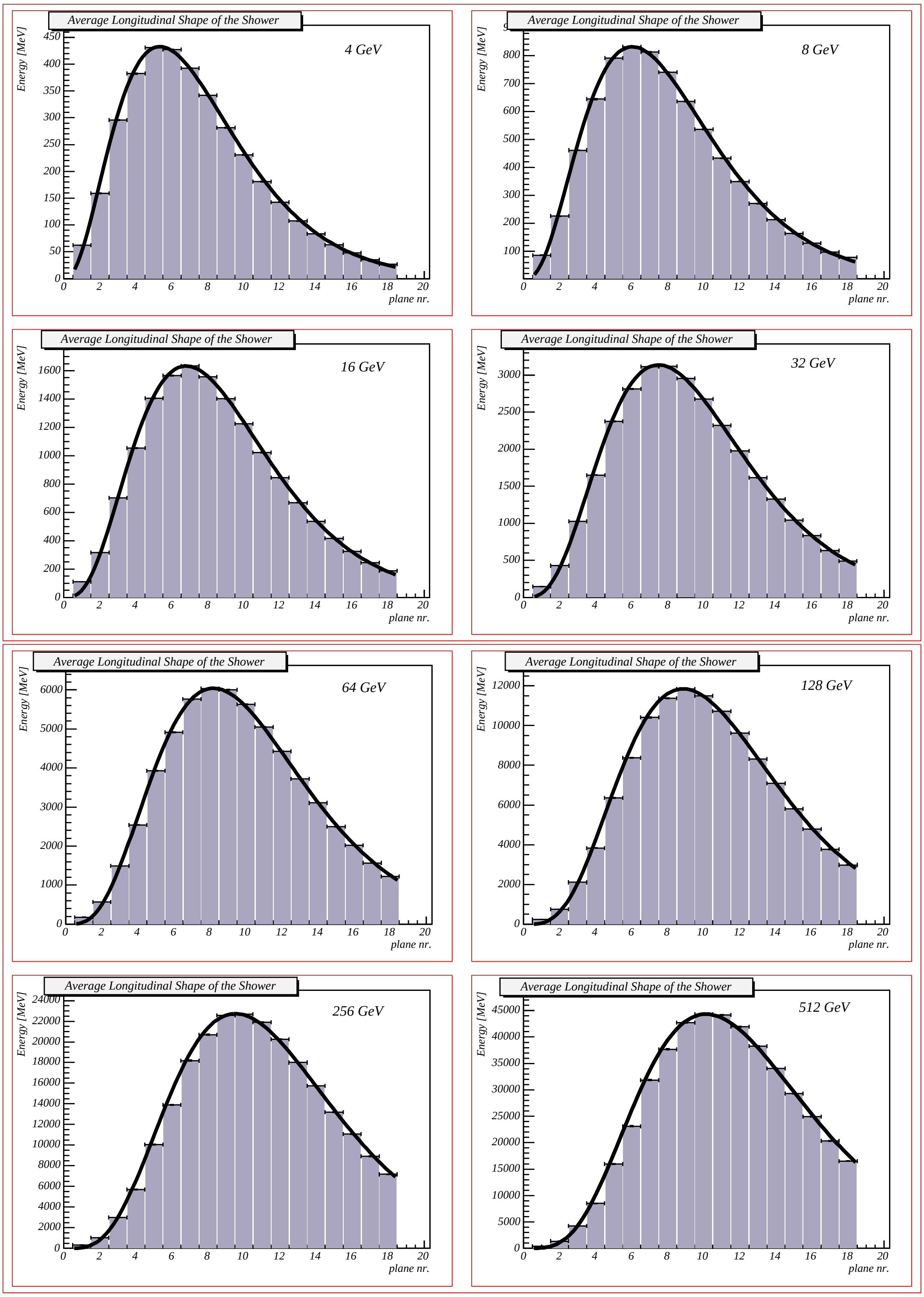

Figure 5.4: Average longitudinal shapes for different generated energies.

Energy	α	b	z_{max} $[l.u.]$
4 GeV	2.46 ± 0.19	0.46 ± 0.02	5.3 ± 0.4
8 GeV	2.76 ± 0.10	0.46 ± 0.01	6.0 ± 0.2
16 GeV	3.24 ± 0.23	0.48 ± 0.02	6.7 ± 0.5
32 GeV	3.51 ± 0.21	0.47 ± 0.02	7.5 ± 0.4
64 GeV	3.82 ± 0.17	0.47 ± 0.02	8.1 ± 0.4
128 GeV	4.14 ± 0.50	0.47 ± 0.05	8.8 ± 0.9
256 GeV	4.33 ± 0.19	0.46 ± 0.02	9.4 ± 0.4
512 GeV	4.54 ± 0.12	0.45 ± 0.01	10.1 ± 0.3

Table 5.1: Results of the fits of the average longitudinal shapes of the shower, done using Eq. 3.1.

5.2 Monte Carlo sample and pre-selection

The sample of ntuples used in this work comes from the AMS-02 MC 2004 Mass Production [45] (started on January 2004 and ended on June 2004). Simulated ntuples were produced both at fixed momentum, namely powers of two from 4 to 2048 GeV, and with a distribution uniform in the momentum logarithm within a given range. In each ntuple, the events were generated as coming from the upper surface of a cube with side 3.9 m, surrounding the detector, and with momentum direction in the range: $-1 < \cos\theta < -0.7$ (the solid angle is $\Omega = 2\pi \cdot 0.3$). The geometrical acceptance for this distribution of generated events is $A_{geo} = 2\pi{\cdot}0.3\, L^2 = 28.67\ m^2 sr$ $(L = 3.9\ m)$.

The MC events were triggered by the coincidence of three out of four TOF planes or by a large energy deposit in ECAL. The trigger efficiency for positrons and protons is shown in Figure 5.5. The efficiency increases with the particle momentum because of a lower bending in the magnetic field between the upper and lower TOF planes.

Pre-selection

Out of the total number of triggered ones, events are pre-selected requiring that:

- the energy deposited in ECAL is greater than 2 GeV;
- no significant lateral leakage is estimated in ECAL;

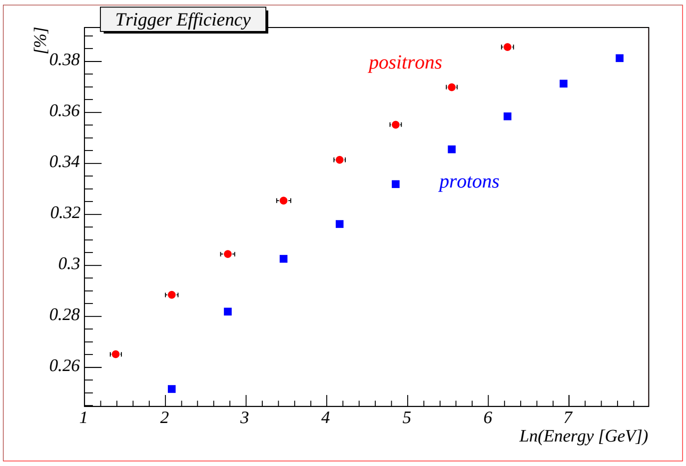

Figure 5.5: Trigger efficiency for positrons and protons as a function of the momentum.

- at least one particle track is reconstructed in the Tracker with charge +1;
- the particle is reconstructed by the TOF as moving downward ($\beta_{TOF} > 0$).

The pre-selection acceptance for positrons ($4 \div 512\ GeV$) and protons ($8 \div 2048\ GeV$) is shown in Figure 5.6.

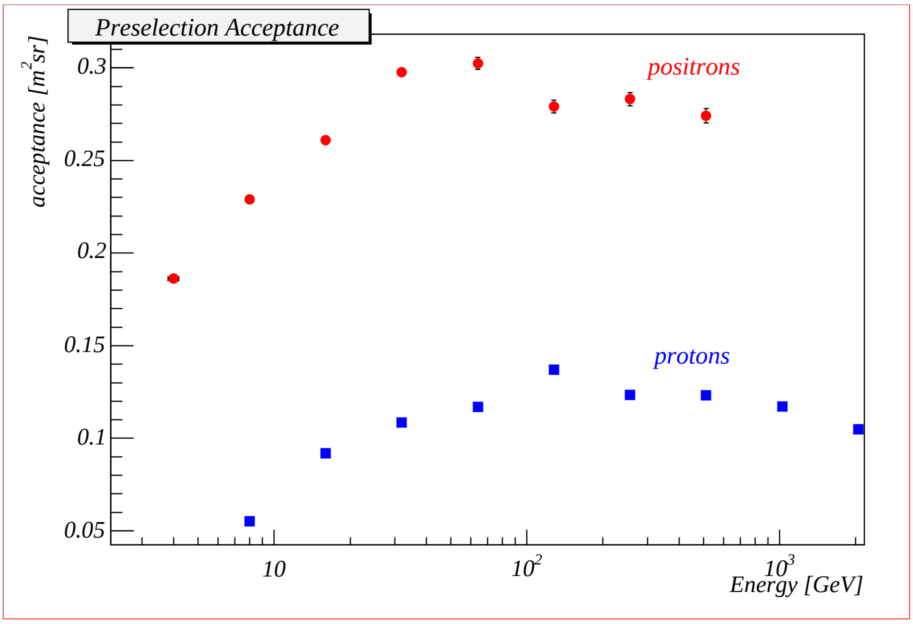

Figure 5.6: Preselection Acceptance for positrons and protons as a function of particle momentum.

5.3 Discrimination criteria for e/p separation

The detection of a positron signal over a wide energy range with a low proton background contamination, requires the combination of different detection techniques: the energy measurement and the shower imaging provided by the ECAL, the momentum determination from the Tracker and the discrimination based on the transition radiation emission in the TRD.

In this analysis two discriminant variables come from the ECAL imaging capability (the *central energy fraction* and the χ^2 *of the longitudinal shape*) and are based on the differences in longitudinal and lateral development of electromagnetic and hadronic showers, as seen in Section 3.2 and 3.3. The third cut is a combination of the energy measurement performed with ECAL, and the momentum measurement provided by the Tracker (*energy and momentum match*). The last cut is performed using only the information from the TRD.

5.3.1 Central energy fraction

The lateral development of the electromagnetic shower scales with the *Molière radius*: on average, only 10% of the energy lies outside a cylinder with radius R_M. On the other hand, an hadronic cascade has usually a wider lateral extent.

The variable used to discriminate an electromagnetic shower from a hadronic cascade, exploiting the differences in the lateral behavior, is the ratio between the energy deposited in the central part of the shower and the total energy deposited by the particle.

For each shower reconstructed in ECAL, the direction is calculated fitting the barycenter of the energy deposits in each plane (for each projection). The "central part" of the shower is defined as the tree cells that overlap the shower direction in that plane. To obtain the energy deposited in the central part is enough to add the contribution from all the central cells.

If more than one shower is reconstructed in ECAL, the central energy fraction for this event is given by the sum of all central energy fractions of each shower.

In Figure 5.7 the distributions of the central energy fraction for positrons and protons at 16, 32, 64, 128, 256, 512 GeV are shown. As we can see, in the central part of an electromagnetic shower is contained from the 80% and the 90% of the total energy deposited. At low energies ($\lesssim$30 GeV) the distributions have a tail for

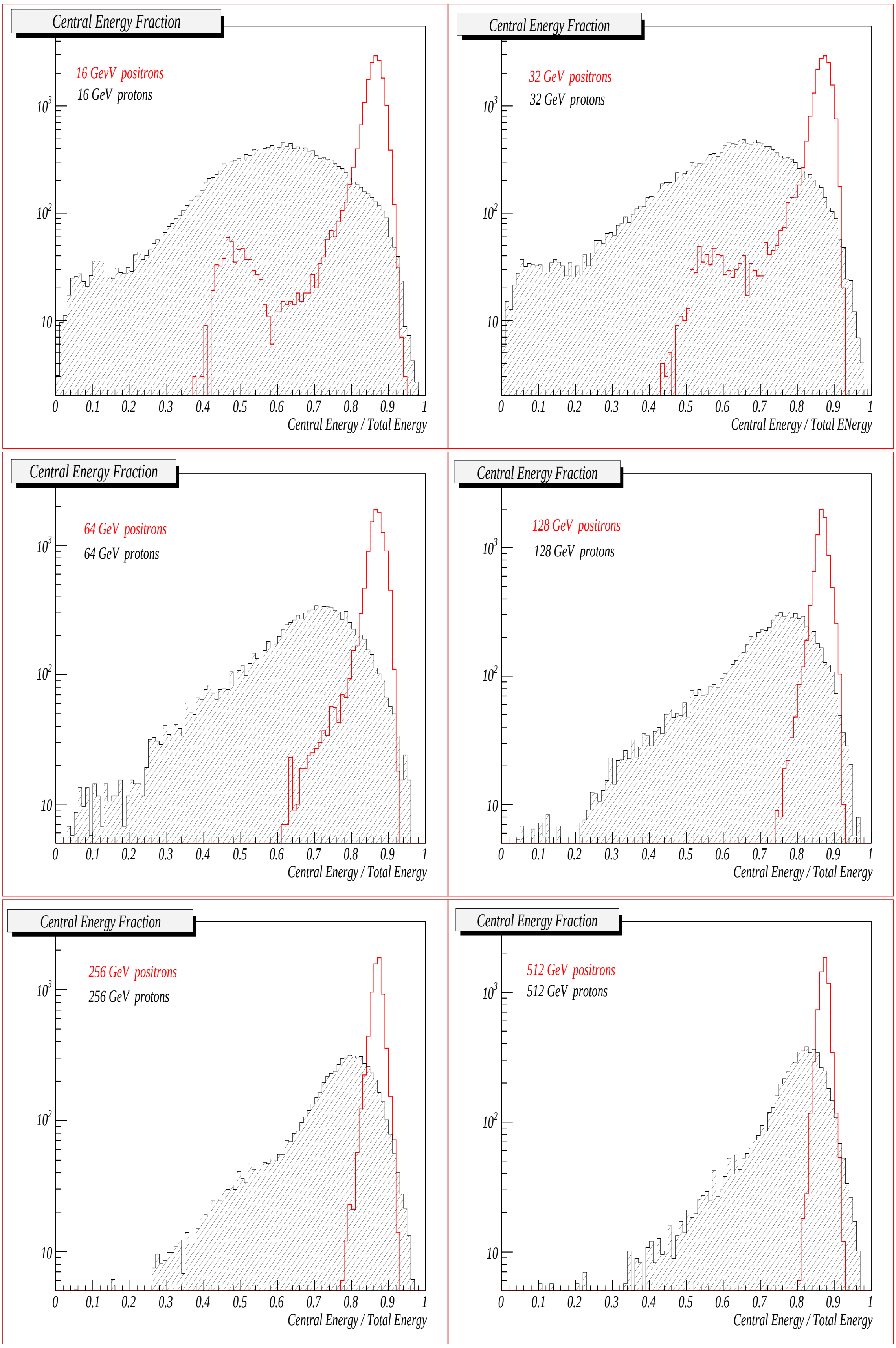

Figure 5.7: Central Energy Fraction distributions for positrons (red lines) and protons (black lines) for generated momentum equal to 16, 32, 64, 128, 256 and 512 GeV.

lower value of E_{centr}/E_{TOT}; this is due of an inefficiency in showers reconstruction that happens when the primary positron and the bremsstrahlung photon are very near but not overlap.

Figure 5.8 shows the efficiencies of this discrimination criterion as a function of

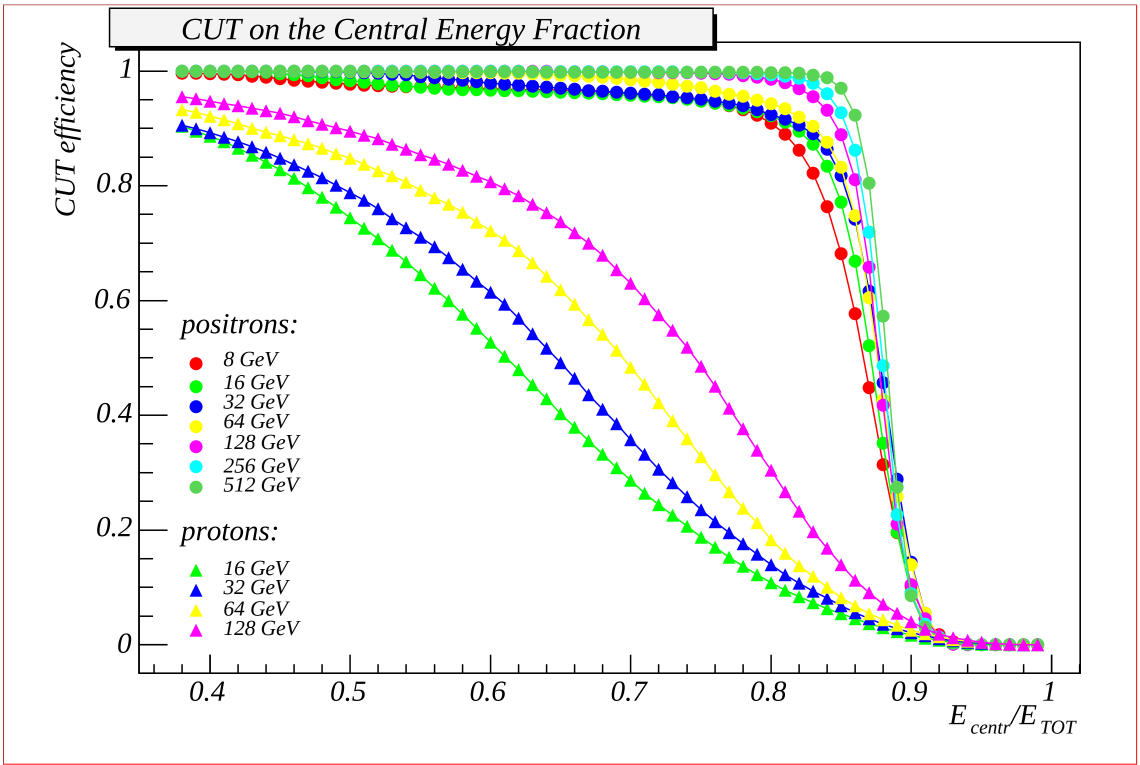

Figure 5.8: Efficiencies of the discrimination criteria based on the central energy fraction as a function of the applied E_{centr}/E_{TOT} cut on different positrons and protons samples.

the value of the applied E_{centr}/E_{TOT} cut, for the different positrons and protons samples. To be sure to have a good efficiency at low energies as well as at large energies, a dependence of the cut value on energy is calculated. The cut values that provide an efficiency of 90% on the positrons samples are fitted by a function of the form:

$$A + B\log(E\ [GeV])$$

and the result of the fit, as shown in Figure 5.9 is:

$$CUT(E_{centr}/E_{TOT}) = (0.778 \pm 0.004) + (0.012 \pm 0.001) \cdot \log(E_{TOT}\ [GeV]).$$

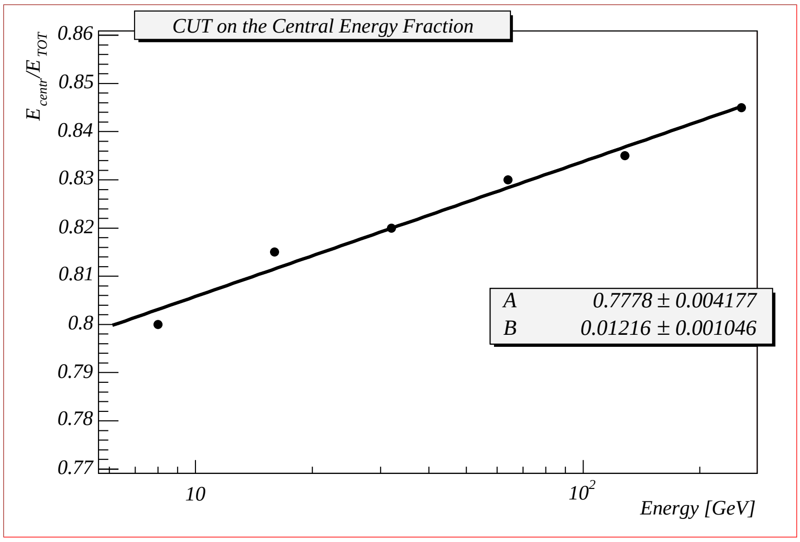

Figure 5.9: Parametrization of the cut value E_{centr}/E_{TOT} to obtain an efficiency equal to 90% for positrons from 8 to 512 GeV.

5.3.2 χ^2 of the longitudinal shape

The average longitudinal profile of electromagnetic showers is well described by the *Gamma* distribution of Eq. 3.1. Therefore a good discriminant variable could be the χ^2 of the longitudinal shape of each shower in the ECAL.

To calculate the χ^2, a parametrization of the average energy deposited in each plane of the ECAL is necessary. For each sample of positrons with generated at fixed momentum, the energy deposit distribution in each plane is fitted with a *Gaussian* function. The mean value (E_p^m) and the standard deviation (σ_p) are extracted from the fits. These values are then fitted as a function of the total energy (in the range $8 \div 512$ GeV). The results are:

$$E_p^m(E_{TOT}) = e^{(A_p + B_p \cdot \log(E_{TOT}[GeV]))}$$

$$\sigma_p(E_{TOT}) = e^{(C_p + D_p \cdot \log(E_{TOT}[GeV]))}$$

where p is the ECAL plane number.

Event by event the reduced χ^2 of the longitudinal shape can be calculated with the following formula:

$$\chi^2 = \frac{1}{15} \sum_{p}^{plane\ nr.} \frac{(E_p - E_p^m(E_{TOT}))^2}{(\sigma_p(E_{TOT}))^2}$$

where E_p is the energy deposited in plane p for the considered event.

In Figure 5.10 are shown the distribution of the χ^2 for positrons and protons at 16, 32, 128 and 256 GeV. Figure 5.11 shows the efficiencies of this discrimination criterion as a function of the value of the applied χ^2 cut, for different positrons and protons samples. As before, to provide an efficiency of 90% on the positrons samples, the cut value is parametrized as a function of the energy. In Figure 5.12 is shown the result of the fit:

$$CUT(\chi^2) = (20 \pm 1) - (10 \pm 1) \cdot x + (2.0 \pm 0.3) \cdot x^2 - (0.13 \pm 0.03) \cdot x^3$$

where $x \equiv \log(E_{TOT}\ [GeV])$.

5.3.3 Energy and momentum match

The positrons energy are well reconstructed in ECAL, while the hadron cascades are not fully contained and the reconstruction fail, so a comparison between the energy measurement performed with ECAL and the momentum measured by the Tracker could be a good discriminant. The variable used for this discriminant criterion is the ratio between the energy measured by the ECAL (E) and the momentum measured by the Tracker (p).

In Figure 5.13 the distributions of the ratio E/p are shown for positrons and protons samples at 32, 64, 128 and 256 GeV.

The distributions for the positrons samples have a peak at $E/p \sim 1$ and a big tail for greater values; these events are the radiative ones, in which the positrons momentum is measured by the Tracker after the bremsstrahlung photon emission. In fact in this case, the measured momentum may result significantly lower than the sum of the energy deposited by the two (e^+ and γ induced) showers in the ECAL.

Figure 5.14 shows the efficiencies of this discrimination criterion as a function of the applied E/p cut, for the different positrons and protons samples.

The cut value is chosen equal to $1 - \epsilon$ where the value of ϵ takes into account the combined resolutions of ECAL and Tracker:

$$\epsilon = \frac{\sigma_{ECAL}(E)}{E} \oplus \frac{\sigma_{Tracker}(E)}{E}$$

where the resolutions are parametrized from Monte Carlo data respectively as:

$$\frac{\sigma_{ECAL}(E)}{E} = \frac{0.113}{\sqrt{E[GeV]}} \oplus 0.0102,$$

$$\frac{\sigma_{Tracker}(E)}{E} = 0.5\ E[TeV] \oplus 0.03.$$

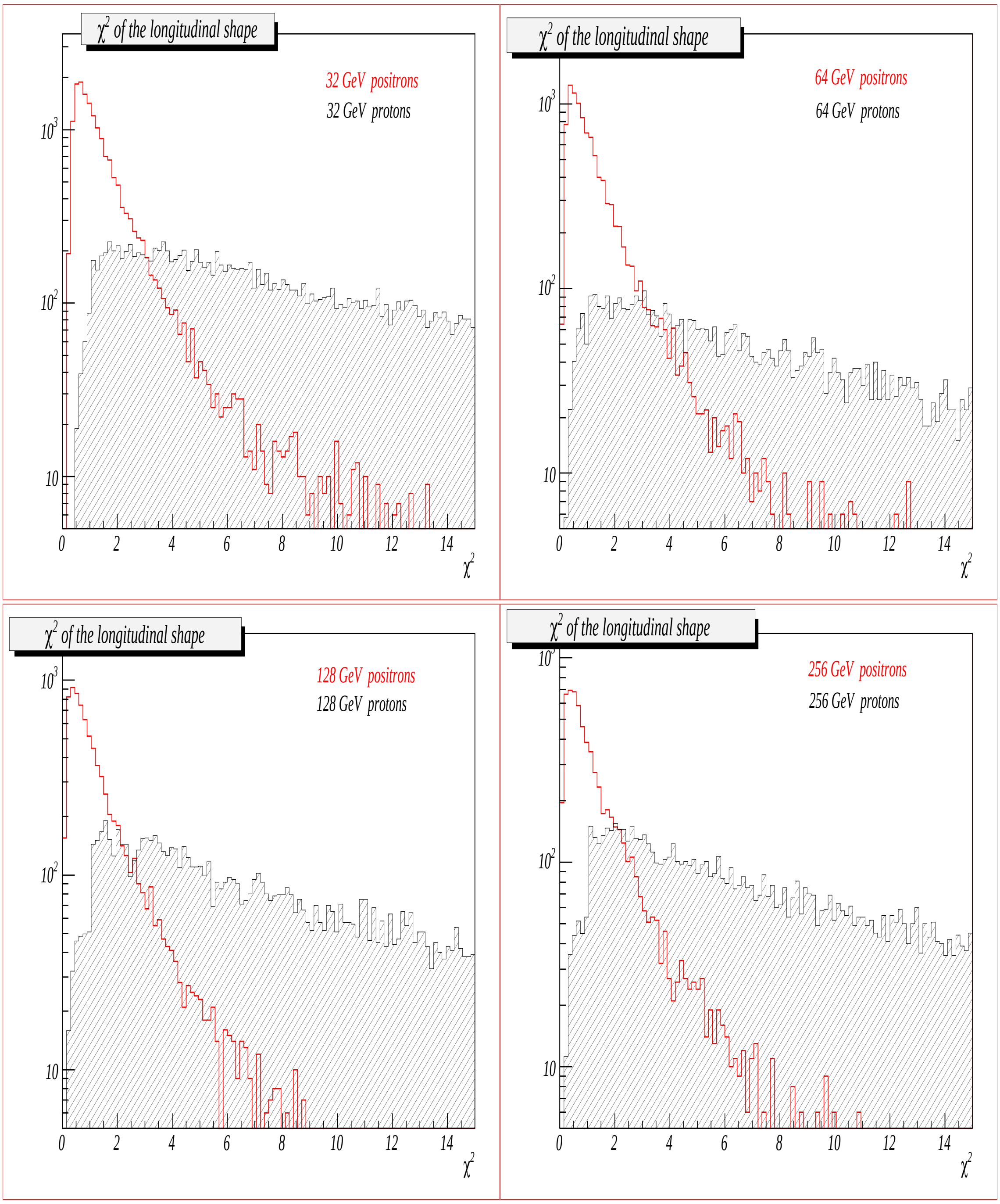

Figure 5.10: Distributions of χ^2 of the longitudinal shapes for positrons (red lines) and protons (black lines) at fixed momentum equal to 32, 64, 128 and 256 *GeV*.

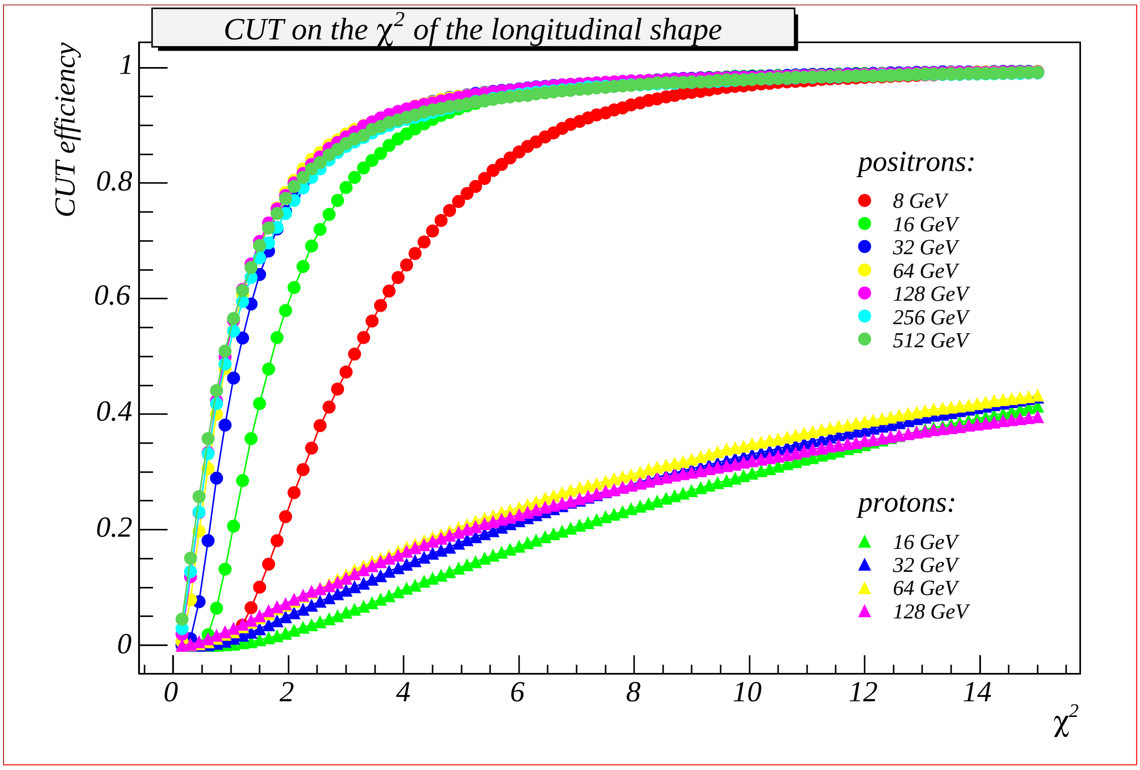

Figure 5.11: Efficiencies of the discrimination criterion based on the the longitudinal shape as a function of the applied χ^2 cut on different positrons and protons samples.

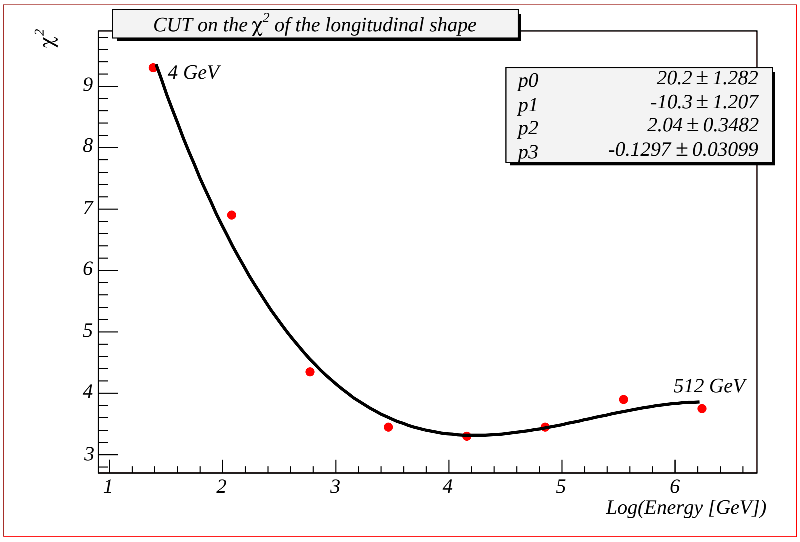

Figure 5.12: Parametrization of the cut value of χ^2 to obtain an efficiency equal to 90% for positrons from 4 to 512 GeV.

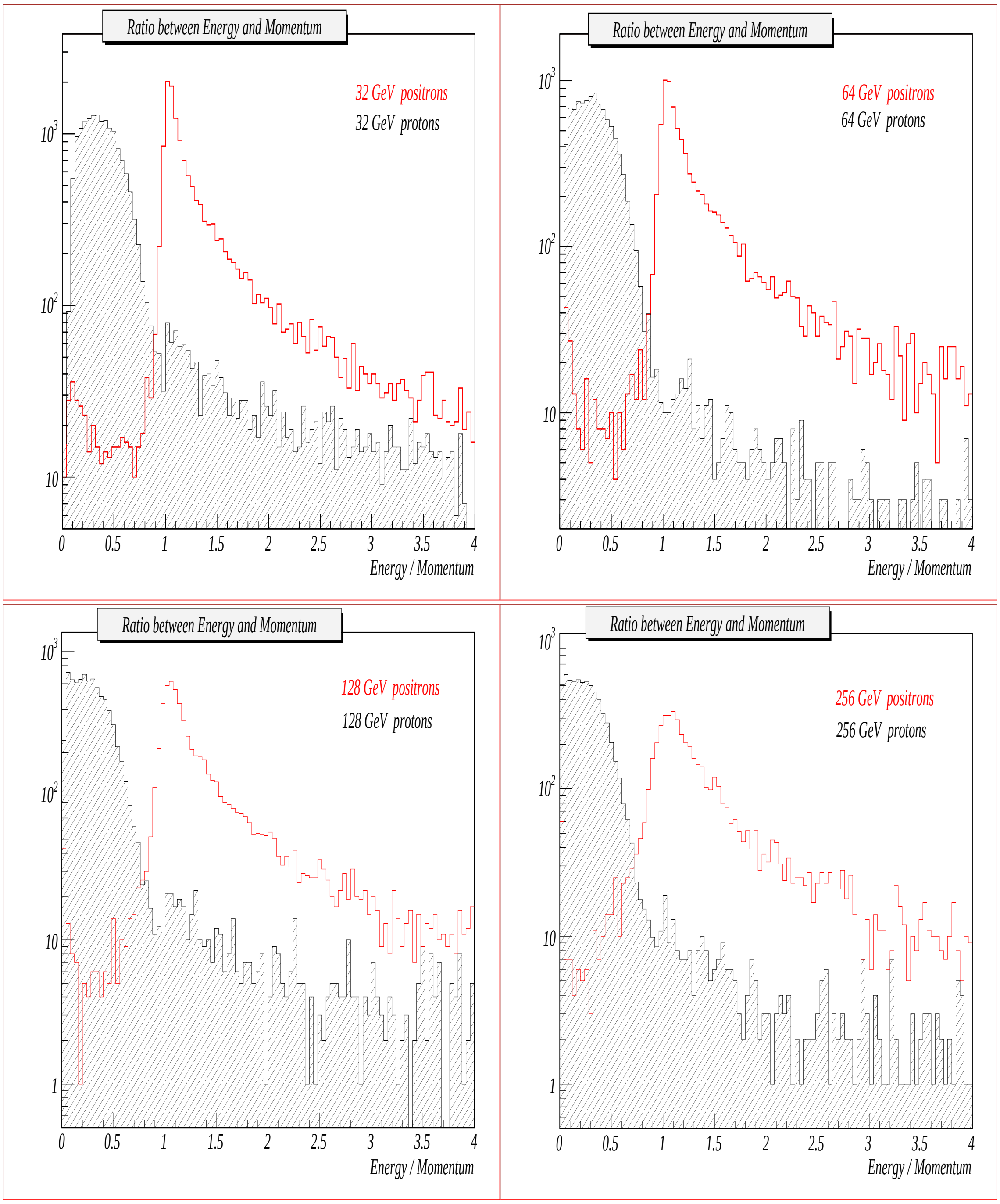

Figure 5.13: Distributions of the ratio E/p for positrons (red lines) and protons (black lines) for generated momentum equal to 32, 64, 128 and 256 GeV.

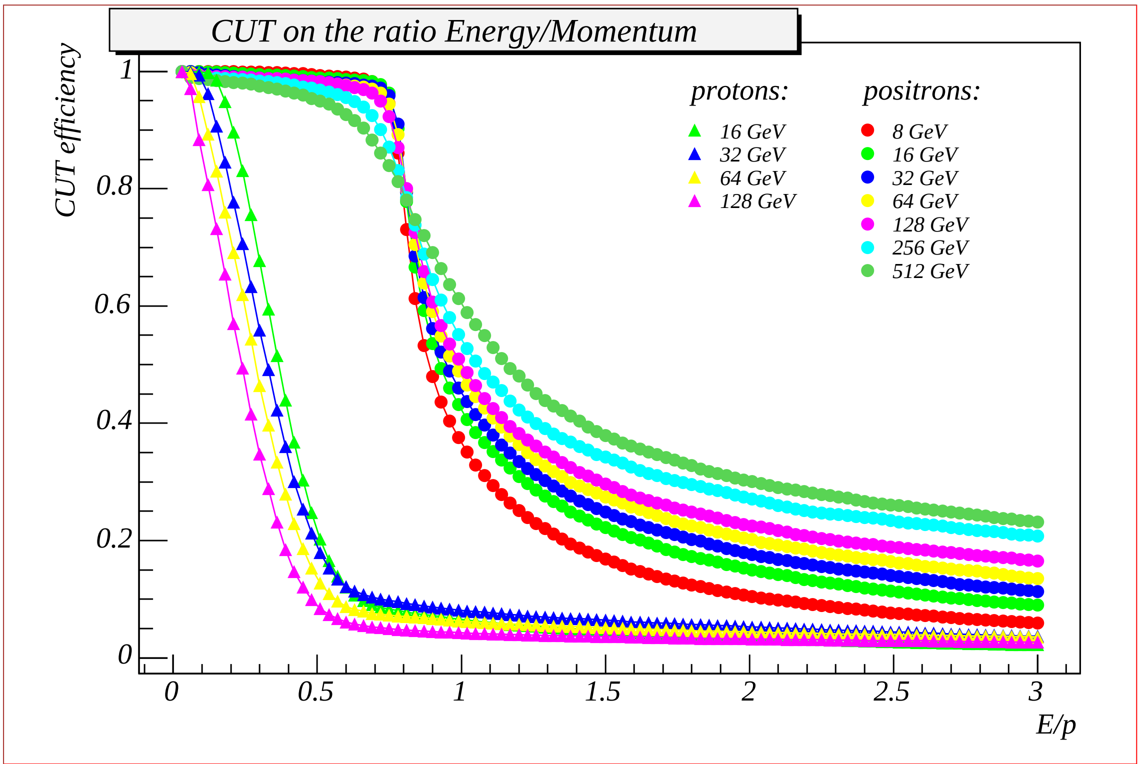

Figure 5.14: Efficiencies of the discrimination criterion based on the energy and momentum match as a function of the applied E/p cut on different positrons and protons samples.

5.3.4 TRD cut

Particle identification using the TRD exploits differences in deposited energy in the straw tubes for particles with high and low relativistic γ. Energy is deposited by normal ionizing processes as well as transition radiation $x - rays$. Since transition radiation turns on for $\gamma > 10^3$, positrons will give off transition radiation $x - rays$, while protons will have negligible $x - rays$ production, in the momentum range from a few GeV up to $\sim 300\ GeV$ (see Figure 2.7).

For the TRD cut, the number of fired TRD tubes cluster has to be greater than 5 (see Figure 5.15). Clusters are counted only when their energy deposit is greater than the threshold energy ($\sim 6\ KeV$) for transition radiation emission.

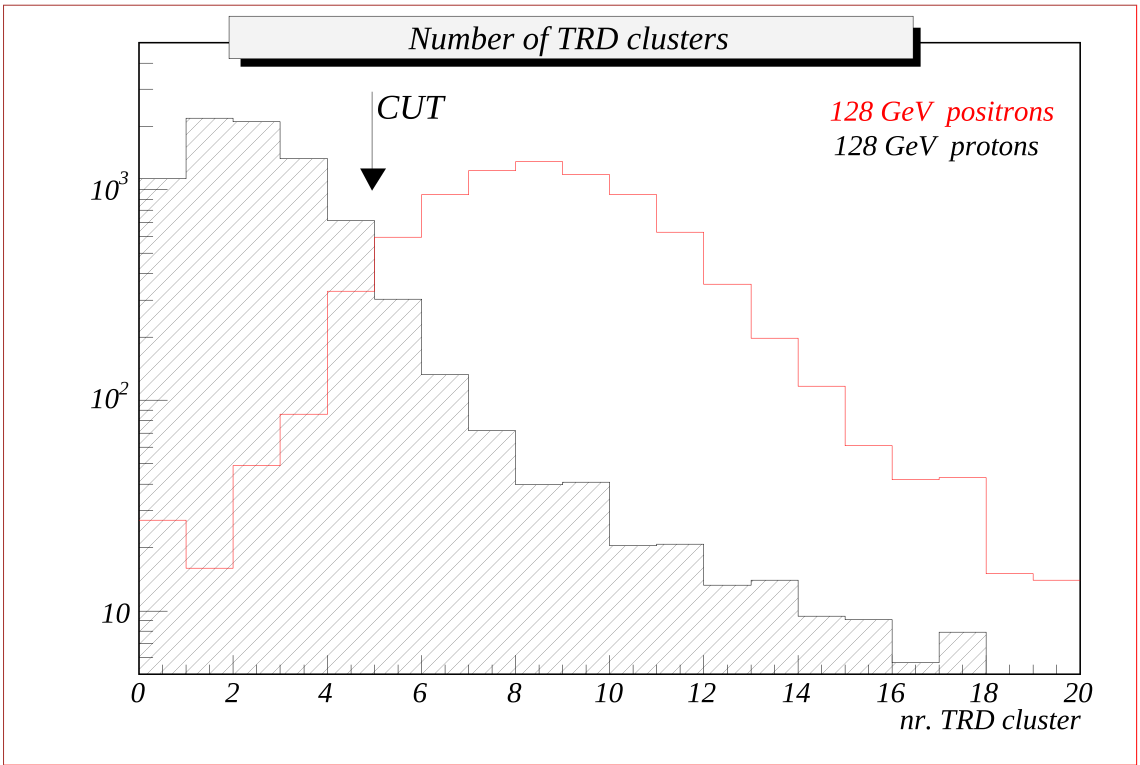

Figure 5.15: Distribution of number of TRD clusters for a positrons and a protons sample at 128 GeV.

5.4 Positrons efficiency and protons contamination

The positrons efficiencies for each cuts are shown in Table 5.2; in the last column there is the efficiency of the combined analysis.

momentum	E_{centr}/E_{TOT} [%]	χ^2 [%]	E/p [%]	TRD [%]	$All\ CUTs$ [%]
4 GeV	82.9 ± 0.3	81.7 ± 0.3	95.1 ± 0.2	92.9 ± 0.2	60.4 ± 0.4
8 GeV	88.4 ± 0.2	89.7 ± 0.2	96.2 ± 0.1	93.0 ± 0.2	71.6 ± 0.3
16 GeV	89.5 ± 0.2	92.4 ± 0.2	96.7 ± 0.1	93.2 ± 0.1	75.7 ± 0.3
32 GeV	89.2 ± 0.2	92.1 ± 0.2	96.0 ± 0.1	93.3 ± 0.1	74.5 ± 0.3
64 GeV	88.4 ± 0.4	91.0 ± 0.3	94.8 ± 0.2	94.5 ± 0.2	73.5 ± 0.4
128 GeV	91.0 ± 0.3	91.3 ± 0.3	94.5 ± 0.2	93.8 ± 0.3	74.4 ± 0.5
256 GeV	90.7 ± 0.4	90.4 ± 0.4	93.0 ± 0.3	95.2 ± 0.3	73.4 ± 0.5
512 GeV	90.1 ± 0.4	91.7 ± 0.4	93.1 ± 0.3	94.5 ± 0.3	73.3 ± 0.6

Table 5.2: Cut efficiencies for positrons at different momentum values. The efficiencies are normalized to the pre-selection samples.

After all the cuts, the total energy distribution for each positrons sample has the same shape that the one before the cuts (as shown in Figure 5.16): the mean values and the standard deviations don't change.

In Table 5.3 are shown the efficiencies for all the cuts over the protons samples, and the total efficiency for the combined analysis. But these values must be interpreted after a look at Figure 5.19 where are shown the distributions of the measured energy before and after all the cuts on the protons samples for generated momentum equal to 32, 64, 128 and 256 GeV. As we can clearly see, the total energy measured in the ECAL (also after the leakage correction) for protons is always less than the particle momentum. Therefore these efficiencies values are not worthy for estimating the e/p rejection power: after the cuts, the protons spectrum will be deformed and the rejection power will be better at high energies than at low energies. To have a good estimate of the rejection power is necessary to apply this analysis to a proton sample generated with the real momentum distribution.

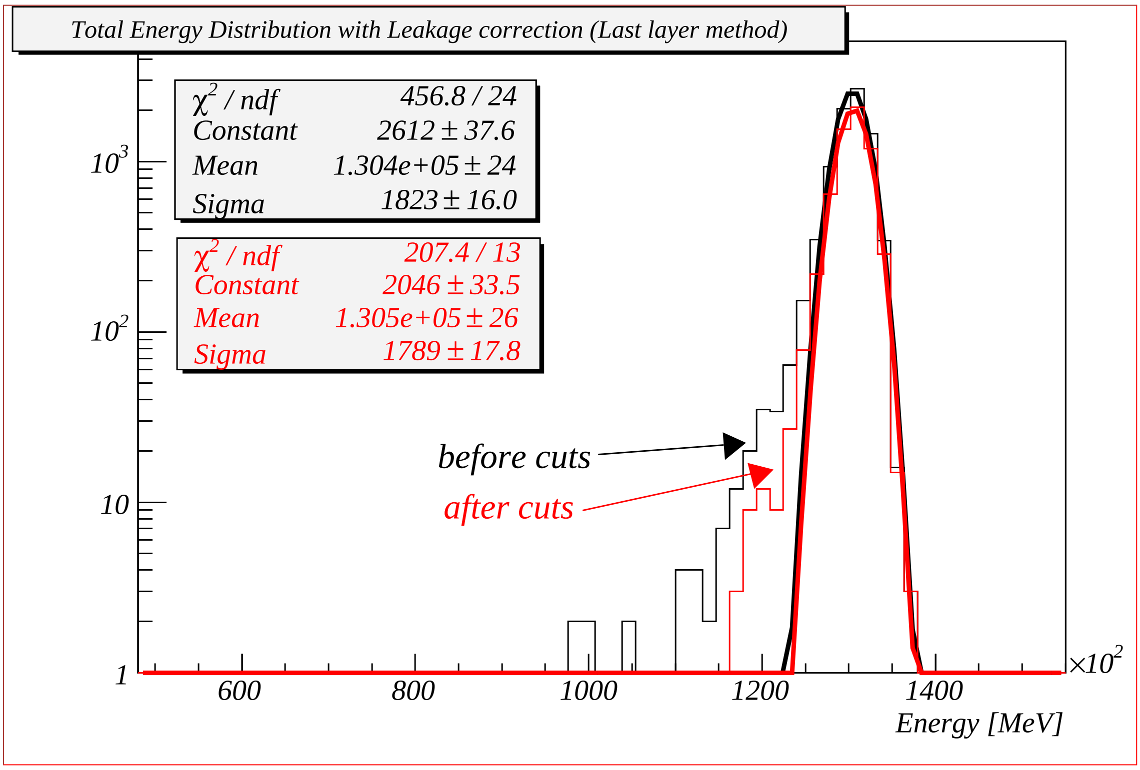

Figure 5.16: Total energy distributions (with leakage correction) before and after the cuts for positrons with generated momentum of 128 GeV.

momentum	E_{centr}/E_{TOT} [%]	χ^2 [%]	E/p [%]	TRD [%]	$All\ CUTs$ [%]
8 GeV	11.3 ± 0.2	22.6 ± 0.2	5.4 ± 0.1	3.2 ± 0.1	0.25 ± 0.03
16 GeV	9.5 ± 0.1	21.9 ± 0.2	8.4 ± 0.1	6.9 ± 0.1	0.31 ± 0.03
32 GeV	11.2 ± 0.2	20.5 ± 0.2	9.8 ± 0.2	9.3 ± 0.2	0.18 ± 0.02
64 GeV	13.1 ± 0.3	18.2 ± 0.4	7.3 ± 0.3	9.0 ± 0.3	0.17 ± 0.04
128 GeV	19.7 ± 0.3	15.4 ± 0.3	5.0 ± 0.1	8.6 ± 0.2	0.10 ± 0.02
256 GeV	24.8 ± 0.3	15.3 ± 0.3	3.9 ± 0.1	11.7 ± 0.2	0.13 ± 0.02
512 GeV	32.9 ± 0.5	14.4 ± 0.4	3.6 ± 0.2	21.7 ± 0.4	0.13 ± 0.04
1024 GeV	41.6 ± 0.5	14.2 ± 0.3	6.0 ± 0.2	65.8 ± 0.4	0.61 ± 0.07
2048 GeV	51.1 ± 0.9	11.6 ± 0.6	14.2 ± 0.7	91.7 ± 0.5	1.1 ± 0.2

Table 5.3: Cut efficiencies for protons at different momentum values. The efficiencies are normalized to the pre-selection samples.

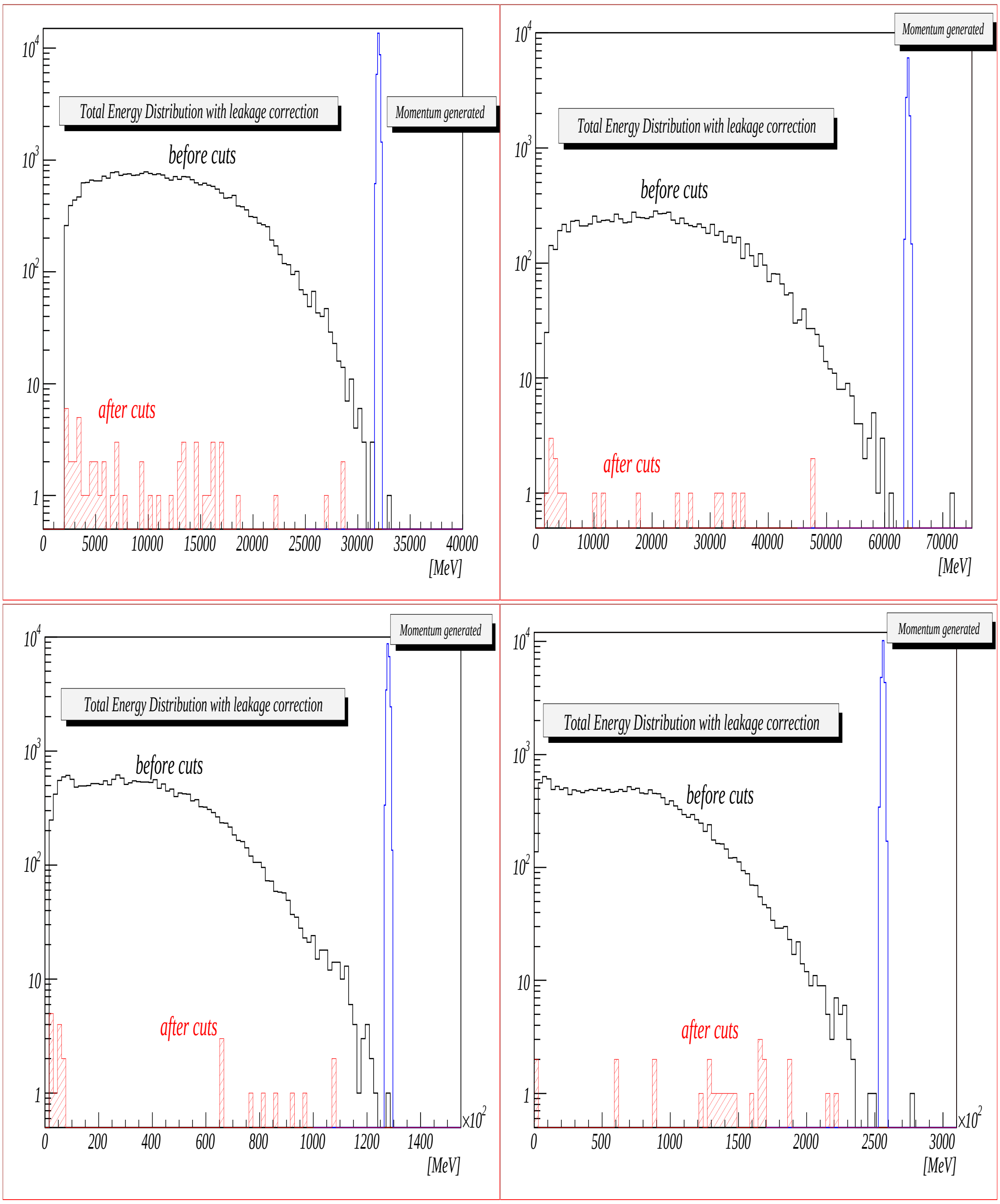

Figure 5.17: Total energy measured distribution before and after all cuts on the protons samples for generation momentum equal to 32, 64, 128 and 256 GeV.

5.5 MC analysis on the positrons and protons spectrum

In the MC 2004 Mass Production, data samples were generated not only at fixed momentum but also with a uniform distribution of momentum logarithm within two given ranges: $10 \div 200\ GeV$ and $200 \div 4000\ GeV$.

All the cuts seen in Section 5.3 were applied on these samples and the results are shown in Figures 5.18 for positrons and Figures 5.19 for protons. In these Figures three different distributions are shown: the blue line is the generated momentum of the triggered and pre-selected events; the black one is measured energy in ECAL for the same events; the red line is the measured energy distribution for those events surviving all the cuts.

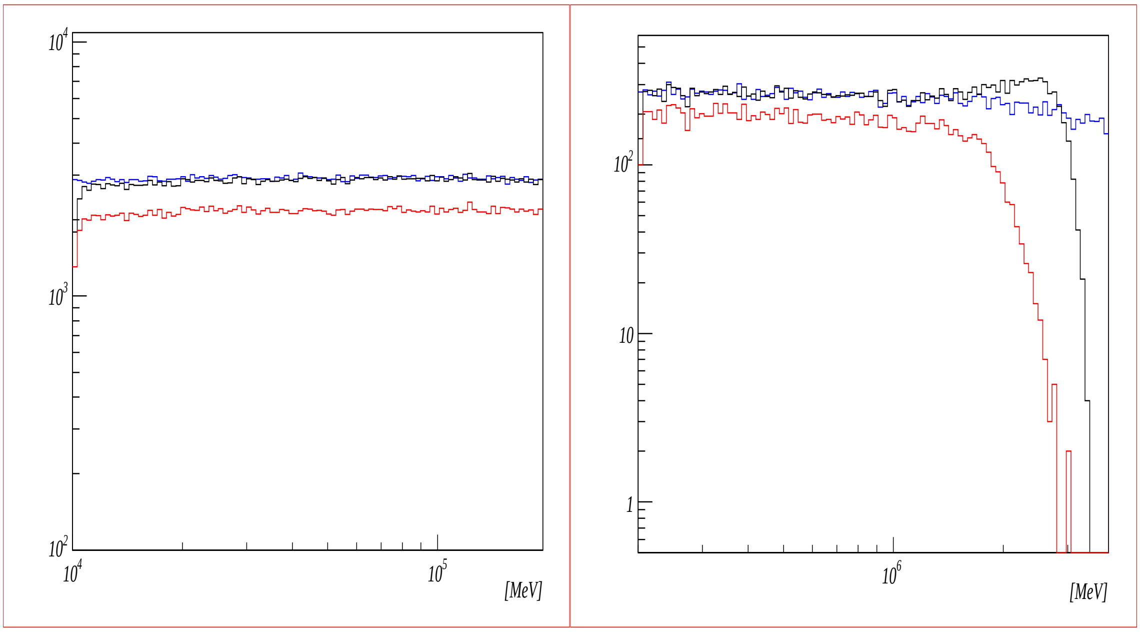

Figure 5.18: Total energy measured distribution before (black lines) and after (red lines) all cuts on the positrons samples for generated momentum in the ranges $10 \div 200\ GeV$ (*left*) and $200 \div 4000\ GeV$ (*right*). The blue lines are the momentum generated distributions for pre-selected events.

The positrons distributions in Figures 5.18 clearly show that the reconstructed energy is excellent agreement with the generated one up to $\sim 2\ TeV$, above which the longitudinal leakage starts to flaw the measure. The combined efficiency of the cuts is almost constant, equal to 75%, over the range from $10\ GeV$ to $\sim 1\ TeV$.

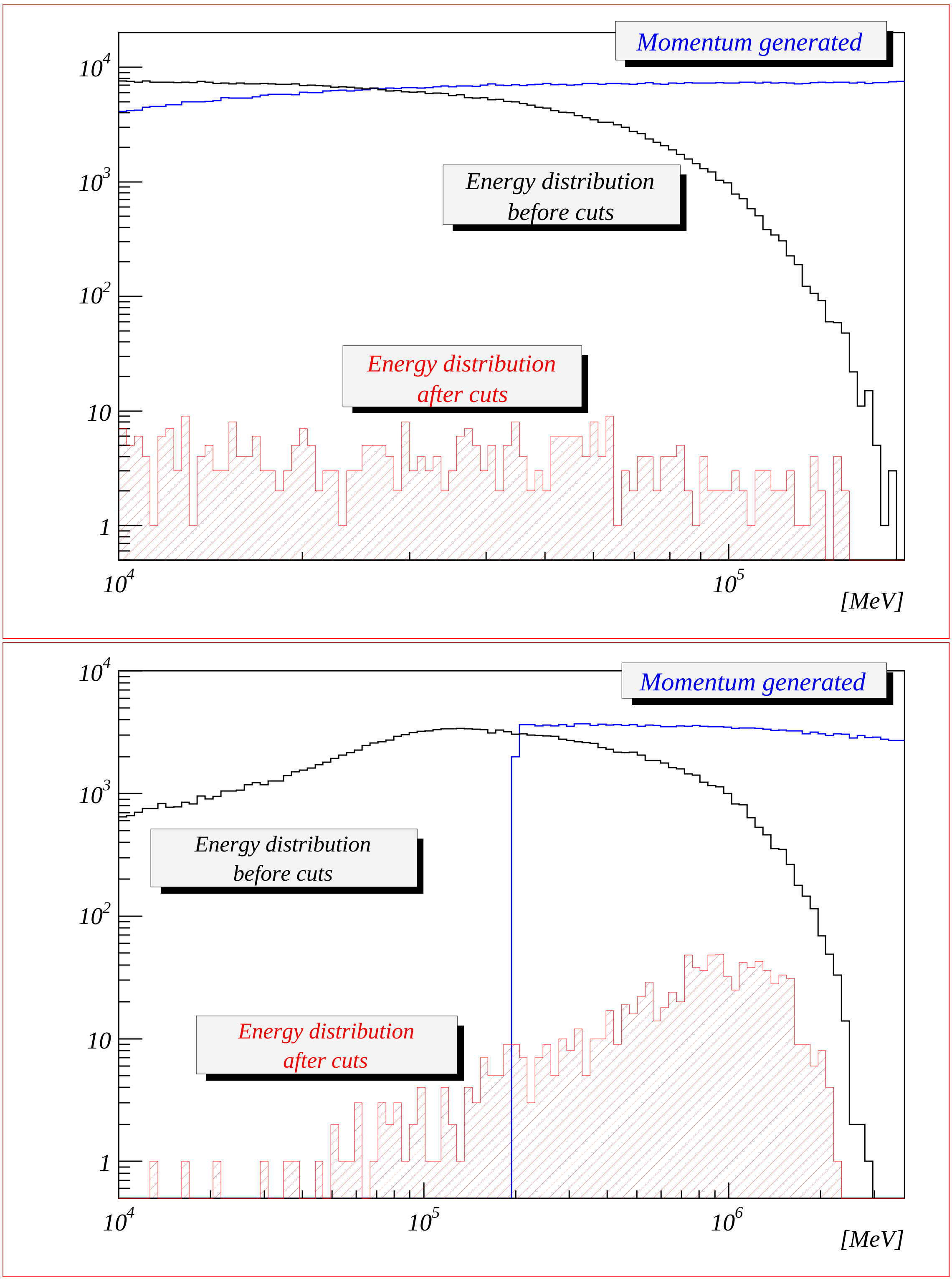

Figure 5.19: Total energy measured distribution before (black lines) and after (red lines) all cuts for the protons samples at generated momentum in the ranges $10 \div 200$ *GeV* (*top*) and $200 \div 4000$ *GeV* (*bottom*). The blue lines are the momentum generated distributions for pre-selected events.

On the other hand the measured energy in ECAL for the protons can be, and usually is, much lower than the generated energy. Figures 5.19 also show that the rejection capability greatly reduces at energies above $\sim 1\ TeV$.

In order to reproduce the expected spectrum for positrons and protons in cosmic rays, the above samples have been weighted using the following analytical formulas:

$$\left(\frac{d\Phi}{dE}\right)_{e+} = \frac{4.5\ \epsilon^{0.7}}{1 + 650\ \epsilon^{2.3} + 1500\ \epsilon^{4.2}} \qquad GeV^{-1}cm^{-2}sr^{-1}s^{-1} \tag{5.1}$$

$$\left(\frac{d\Phi}{dE}\right)_{p} = 17.1\ \epsilon^{-2.78} \qquad MeV^{-1}m^{-2}sr^{-1}s^{-1} \tag{5.2}$$

The first equation is the theoretical spectrum derived by Moskalenko and Strong [46] for positrons ($\epsilon = E/(1\ GeV)$), while the second is the protons spectrum ($\epsilon = E/(1\ MeV)$) measured by AMS-01 [30] (see Equation 2.3). The flux calculated by these formulas are plotted in Figure 5.20 for both positrons and protons.

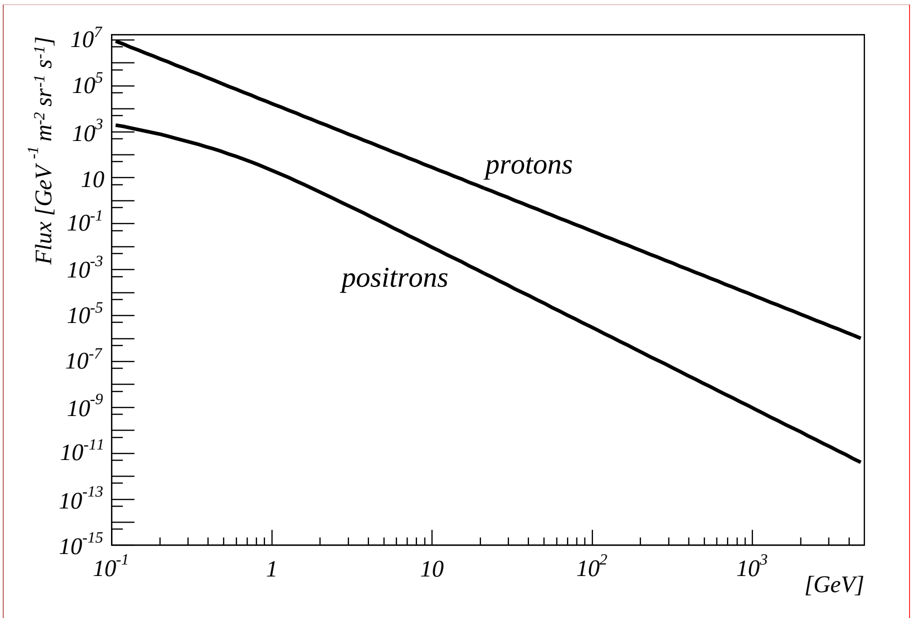

Figure 5.20: Positrons and protons spectrum from Equation 5.1 and 5.2.

Since the MC samples were generated with an uniform distribution of the momentum logarithm, each event must be weighted with a factor which takes into account the value of the flux at the particle generated momentum, and the number of events in the same momentum bin. Given the flux, the events rates is obtained multiplying by the geometric acceptance and the bin energy width.

Summing the two distributions corresponding to the two momentum ranges, the total rates for protons and positrons are found as displayed in Figure 5.21. Four curves are plotted: blue triangles represent the rate as a function of generated momentum for those protons which are triggered and pre-selected; the black triangles represent the rate as function of the measured energy for the same events; the red triangles describe the rate as a function of the measured energy for protons surviving all the cuts; the red full circles show the rate as a function of the measured energy for positrons after all the cuts. At this events rate during a period of three years, AMS-02 will collect 10^7 positrons at $\sim 10\ GeV$ and about 10^3 positrons at $\sim 500\ GeV$.

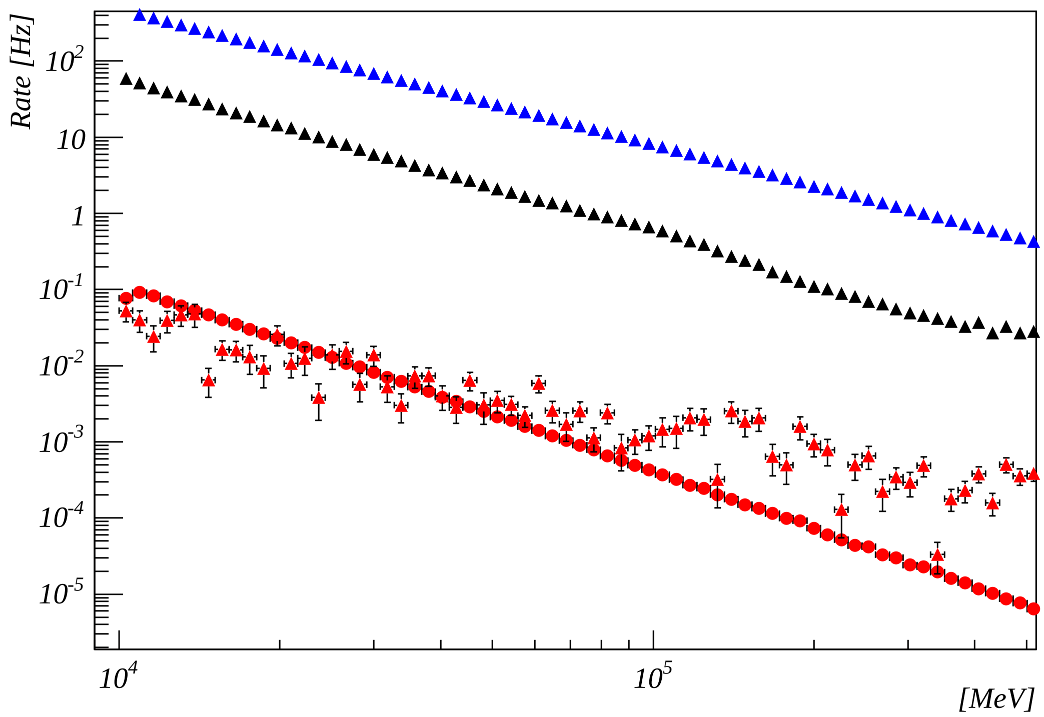

Figure 5.21: *Blue triangles* represent the rate as a function of generated momentum for those protons which are triggered and pre-selected; the *black triangles* represent the rate as function of the measured energy for the same events; the *red triangles* describe the rate for protons surviving all the cuts; the *red full circles* show the rate for positrons after all the cuts.

A good parameter to estimate the quality of the rejection power is the *signal to background ratio* define as:

$$\frac{S}{\sqrt{B}} = \frac{R_S \Delta T}{\sqrt{R_B \Delta T}} = \frac{R_S}{\sqrt{R_B}}\sqrt{\Delta T}$$

where R_S is the signal rate, R_B the background rate and ΔT is the time interval during which data are collected.

For three years of AMS-02 data taking, the expected signal to background ratio is shown in Figure 5.22 (bottom) together with the signal and background events rates (top). A good signal to background ratio ($S/\sqrt{B} \geq 10$) is needed to discriminate

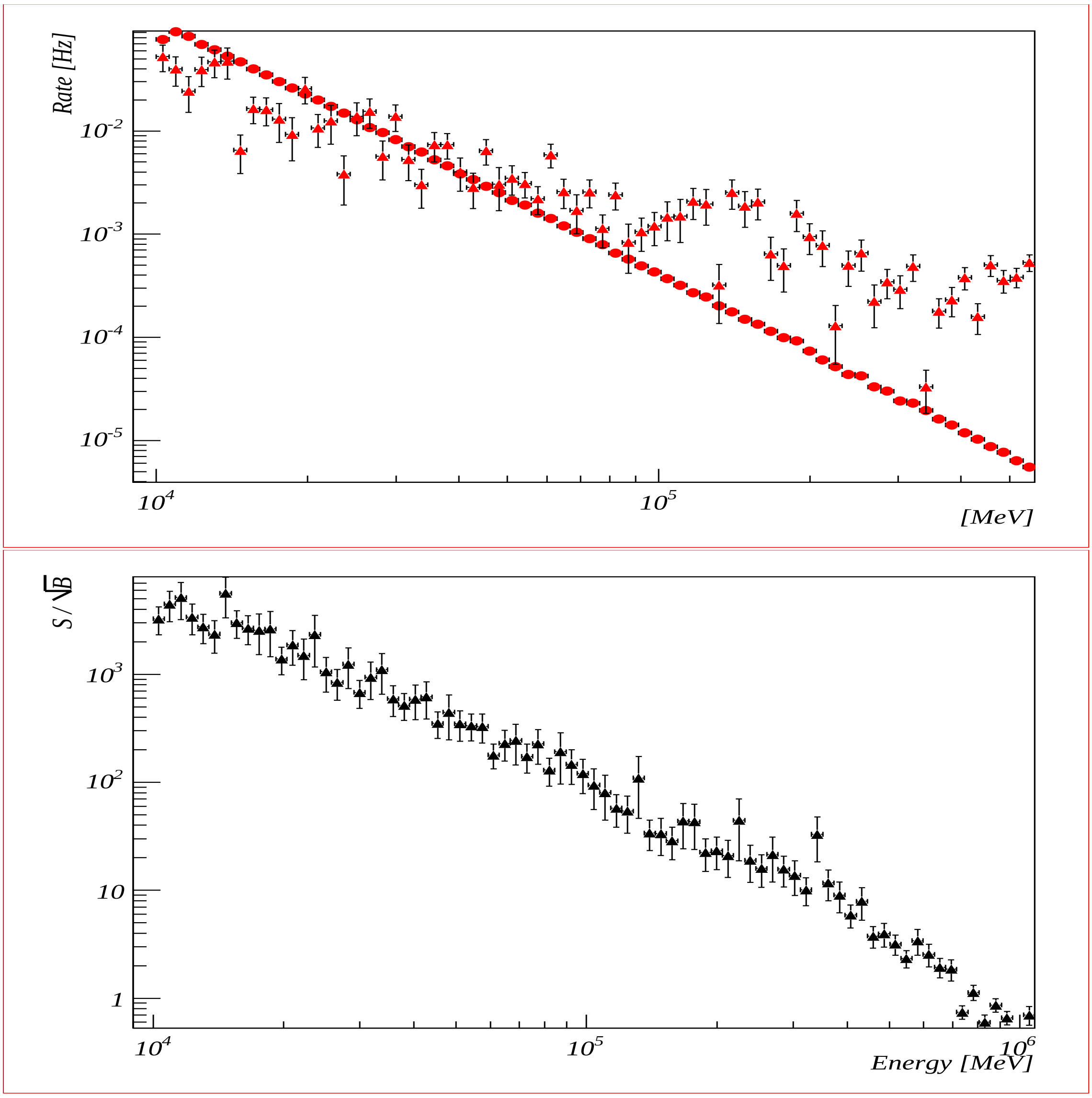

Figure 5.22: *Top*: signal and background rate after all the cuts; *bottom*: signal to background ratio for three years of data taking.

positrons from protons. As can be seen from the Figure, the rejection power is good enough below $\sim 300\ GeV$.

Such a good rejection power combined with the excellent energy resolution of

ECAL will allow to see the possible excess due to the neutralino annihilation.

Bibliography

[1] K. C. Freeman. On the disks of spiral and so galaxies. *Astrophys. J.*, 160:811, 1970.

[2] A. Einstein. *Ann. Phys.*, 69:436, 1922.

[3] A. Friedmann. *Z. Phys.*, 10:377, 1922.

[4] E.P. Hubble. *Publ. Nat. Acad. Sci*, 15:168, 1929.

[5] G. Gamow. *Phys. Rev.*, 74:505, 1948.

[6] Arno A. Penzias and Robert Woodrow Wilson. A measurement of excess antenna temperature at 4080-mc/s. *Astrophys. J.*, 142:419–421, 1965.

[7] K.S. Thorne C.W. Misner, J.A. Wheeler. *Gravitation*. 1973.

[8] Shoko Sakai et al. The hubble space telescope key project on the extragalactic distance scale xxiv: The calibration of tully-fisher relations and the value of the hubble constant. 1999.

[9] Palash B. Pal. Determination of cosmological parameters: An introduction for non-specialists. *Pramana*, 54:79–91, 2000.

[10] J. C. Mather et al. Early results from the cosmic background explorer (cobe). *Astrophys. J.*, 354:L37, 1990.

[11] P. de Bernardis et al. A flat universe from high-resolution maps of the cosmic microwave background radiation. *Nature*, 404:955–959, 2000.

[12] Wayne Hu and Scott Dodelson. Cosmic microwave background anisotropies. *Ann. Rev. Astron. Astrophys.*, 40:171, 2002.

[13] D. N. Spergel et al. First year wilkinson microwave anisotropy probe (wmap) observations: Determination of cosmological parameters. *Astrophys. J. Suppl.*, 148:175, 2003.

[14] John L. Tonry et al. Cosmological results from high-z supernovae. *Astrophys. J.*, 594:1–24, 2003.

[15] A.H. Broeils K.G. Begeman and R.H. Sanders. *Mon. Not. R. Astr. Soc.*, 249:523, 1991.

[16] V. Plyaskin. Antimatter and dark matter search with the alpha magnetic spectrometer (ams). *Surveys High Energ. Phys.*, 13:177–201, 1998.

[17] Scott Burles and David Tytler. The deuterium abundance toward qso 1009+2956. *Astrophys. J.*, 507:732–744, 1998.

[18] R. Bernabei et al. Dark matter search. *Riv. Nuovo Cim.*, 26:1–73, 2003.

[19] D. S. Akerib et al. New results from the cryogenic dark matter search experiment. *Phys. Rev.*, D68:082002, 2003.

[20] L. Bergstrom. Indirect detection of neutralino dark matter. 1999.

[21] G. Valle, E. Falchini, et al. Continuum gamma spectra from neutralino annihilation. *Nucl. Phys. Proc. Suppl.*, 113:186–192, 2002.

[22] M. Kamionkowski and M.S. Turner. A distinctive positron feature from heavy wimp annihilations in the galactic halo. *Phys. Rev.*, D43:1774–1780, 1991.

[23] I. V. Moskalenko and A. W. Strong. Positrons from particle dark-matter annihilation in the galactic halo: Propagation green's functions. *Phys. Rev.*, D60:063003, 1999.

[24] Jonathan L. Feng, Konstantin T. Matchev, and Frank Wilczek. Prospects for indirect detection of neutralino dark matter. *Phys. Rev.*, D63:045024, 2001.

[25] S. W. Barwick et al. Measurements of the cosmic-ray positron fraction from 1-gev to 50-gev. *Astrophys. J.*, 482:L191–L194, 1997.

[26] M. A. DuVernois et al. Cosmic ray electrons and positrons from 1-gev to 100-gev: Measurements with heat and their interpretation. *Astrophys. J.*, 559:296–303, 2001.

[27] Edward A. Baltz, Joakim Edsjo, Katherine Freese, and Paolo Gondolo. The positron excess and supersymmetric dark matter. 2002.

[28] J. Alcaraz et al. Search for antihelium in cosmic rays. *Phys. Lett.*, B461:387–396, 1999.

[29] J. Alcaraz et al. Protons in near earth orbit. *Phys. Lett.*, B472:215–226, 2000.

[30] J. Alcaraz et al. Cosmic protons. *Phys. Lett.*, B490:27–35, 2000.

[31] J. Alcaraz et al. Leptons in near earth orbit. *Phys. Lett.*, B484:10–22, 2000.

[32] J. Alcaraz et al. Helium in near earth orbit. *Phys. Lett.*, B494:193–202, 2000.

[33] B. Blau et al. The superconducting magnet of ams-02. *Nucl. Phys. Proc. Suppl.*, 113:125–132, 2002.

[34] W. J. Burger. The ams silicon tracker. *Nucl. Phys. Proc. Suppl.*, 113:139–146, 2002.

[35] Diego Casadei et al. The ams-02 time of flight system. *Nucl. Phys. Proc. Suppl.*, 113:133–138, 2002.

[36] T. Siedenburg et al. A transition radiation detector for ams. *Nucl. Phys. Proc. Suppl.*, 113:154–158, 2002.

[37] J. Casaus. The ams rich detector. *Nucl. Phys. Proc. Suppl.*, 113:147–153, 2002.

[38] R. Mukherjee et al. Egret observations of high-energy gamma ray emission from blazars: An update. *Astrophys. J.*, 490:116–135, 1997.

[39] G. Lamanna. High-energy gamma-ray detection with the alpha magnetic spectrometer on board the international space station. *Nucl. Phys. Proc. Suppl.*, 113:177–185, 2002.

[40] I. V. Moskalenko and A. W. Strong. Production and propagation of cosmic-ray positrons and electrons. *Astrophys. J.*, 493:694–707, 1998.

[41] R. Kossakowski. *AMS Note 2002-01-03*, 2002.

[42] F. Pilo, E. Falchini, et al. The ams-02 electromagnetic calorimeter. *Nucl. Phys. Proc. Suppl.*, 113:159–165, 2002.

[43] C. Goy. *AMS Note 2003-07-01*, 2003.

[44] F. Cervelli, E. Falchini, et al. A reduced scale e.m. calorimeter prototype for the ams-02 experiment. *Nucl. Instrum. Meth.*, A490:132–139, 2002.

[45] V. Choutko and A. Klimentov. http://pcamss0.cern.ch/mm.html. 2004.

[46] I. V. Moskalenko and A. W. Strong. Production and propagation of cosmic-ray positrons and electrons. *Astrophys. J.*, 493:694–707, 1998.